Magma evolution and processes of the Ashi Volcano, NW Tibet, China: Sr isotope studies of plagioclase crystals

by

Sara Speetjens

A thesis submitted to the Graduate Faculty of
Auburn University
in partial fulfillment of the
requirements for the Degree of
Master of Science

Auburn, Alabama
May 5, 2018

Approved by

Haibo Zou, Chair, Professor of Geosciences
Willis Hames, Professor of Geosciences
David King, Professor of Geosciences
Mark Steltenpohl, Professor of Geosciences

Abstract

The Ashi Volcano is a member of the Ashikule Volcanic Field (AVF) and is located on the northwestern margin of the Tibetan Plateau. The Ashi Volcano draws much attention from volcanologists due to its recent eruptions in a high plateau (the last eruption occurred in 1951), in spite of its moderate size with a cone height of 110 meters. The composition of the Ashi volcanic rocks is trachyandesite.

The role of open-system processes, such as magma assimilation, is controversial for the evolution of the Ashi Volcano. Previous studies in support of open-system processes were based on the presence of plagioclase compositional reverse zoning, whereas previous arguments against open-system processes were derived from the absence of any correlations between whole-rock Sr isotopic compositions and SiO_2. However, compositional zoning of plagioclase may be derived by other factors, such as temperature, pressure and water contents. And whole-rock Sr isotopic compositions may not have the sensitivity to detect open-system processes. Here we use single-grain Sr isotopic compositions in plagioclase to evaluate the role of open-system processes in the magma evolution of the Ashi Volcano. Unlike plagioclase compositional zoning, single-grain plagioclase Sr isotopic compositions are not affected by temperature, pressure, or water content. Compared with whole-rock Sr isotope compositions, single-grain Sr isotopic compositions are more sensitive to open-system processes.

Single-grain plagioclases and whole-rock samples of Ashi Volcano have been analyzed for their Sr isotopic compositions by a thermal ionization mass spectrometer at Auburn

University. About 50% of the plagioclase grains have Sr isotopic compositions similar to whole-rock Sr isotopic compositions. The other 50% of the plagioclase grains have $^{87}Sr/^{86}Sr$ ratios (up to 0.7159) significantly higher than the whole-rock $^{87}Sr/^{86}Sr$ ratios (0.7101-0.7102), indicating assimilation of the Ashi magmas by crustal materials with more radiogenic Sr. Such materials with more radiogenic Sr do not represent recharge of mantle-derived magmas, because mantle-derived magmas have $^{87}Sr/^{86}Sr$ ratios significantly lower than the whole-rock ratios of 0.7101-0.7102.

Using AU-EMPA the primary mineral phases were confirmed and compositional analyses of clinopyroxene, orthopyroxene, and plagioclase were conducted. Reverse compositional zonation was observed in plagioclase grains, which can be caused by changing pressure, temperature, and water content. The compositional analyses on orthopyroxene and clinopyroxene phases were used to calculate pre-eruption equilibrium pressure and temperature values. The temperature estimates range from 1081-1104 ºC and pressure estimates range from 5.6-7.1 kbars, which translates to a depth range of 18.5-23.4 km.

Acknowledgments

Funding for this research was provided by Dr. Haibo Zou through an NSF of China grant (41272070) and by the Department of Geosciences through the Spencer Waters and Dan Folse Memorial award. Thanks are owed to Dr. Qicheng Fan for the gracious donation of the samples used in this research. Dr. Yongwei Zhao and Dr. Hong Yu are thanked for their aid in preparation of supplies used in Dr. Zou's radiogenic isotope laboratory and clean lab. Thanks are owed to the scientists at Wagner Petrographic for the diligent preparation of the thin and thick sections used in this research. Thanks and gratitude are most especially owed to my advisor Dr. Haibo Zou for providing funding, materials, assistance in Sr isolation and measurement, and thesis writing. This research was also greatly aided by the instruction and aid from Dr. Willis Hames in the Auburn University Electron Microprobe Analyzer (AU-EMPA) Lab and Kayla Griffen for helping in sample analyses. This research also benefitted greatly from suggestions from committee members Dr. David King and Dr. Mark Steltenpohl.

Table of Contents

List of Tables

List of Figures

Introduction

The Ashi Volcano is a member of the Ashikule Volcanic Cluster (AVC), which is located in the northwestern margin of the Tibetan Plateau. The AVC is located near the junction of major fault zones (Altun and Kangxiwa) in a shear-extensional tectonic basin. The AVC consists of fourteen major volcanoes and dozens of subvolcanoes with volcanic features typical of a volcanic field (volcanic cones, lava terraces, lava valleys, etc.). The reported ages of the eruptions in the AVC are Pliocene to Holocene (Liu Jiaqi et al., 1990; Xu et al., 2012). On May 27, 1951, the Xinjiang Newspaper reported an explosive eruption in the AVC, and has since been attributed to the Ashi Volcano (Liu Jiaqi et al., 1990; Yu et al., 2014; Wei et al., 2017). The AVC is located in a tectonically unique and active geologic setting, with major compressional forces causing widespread faulting and volcanism. Due to extreme remoteness, however, the AVC has had limited research done on it until recently. Due to the recent eruption and a 7.3 magnitude earthquake south of the AVC, many scientists have taken note of these active volcanoes, sparking an interest in the source, composition, and evolution of the magma.

There is significant information that can be derived from radiogenic isotopic signatures that can yield information on the history of a volcanic rock that is inaccessible through other scientific approaches. Strontium (Sr), the element whose isotopes are of interest, is an alkaline earth metal with atomic number 38.

It is chemically very similar to calcium (Ca) and thus is a common substitute in Ca bearing minerals. Early in earth's history during the separation of the crust and mantle, there was significant fractional crystallization, which excluded incompatible elements from mantle-derived basaltic melts and included these incompatible elements into silicic residual melts, which formed the continental crust. Rubidium (Rb) was one of the incompatible elements enriched in the continental crust. ^{87}Rb is a radiogenic isotope that decays to ^{87}Sr with a half-life of 49 billion years. By comparing the ratio of this daughter isotope ^{87}Sr with the stable ^{86}Sr isotope, the characteristic of parental magma can be determined, with high ^{87}Sr/^{86}Sr ratios being derived from crustal melts and low ^{87}Sr/^{86}Sr ratios being derived from a normal mantle source. In applying ^{87}Sr/^{86}Sr ratios to samples of plagioclase grains from the Ashi Volcano, the composition and the evolution processes of the parent magma can be assessed in a manner that has yet to be done.

Objectives

The Ashi Volcano's magma source and evolution is relatively poorly understood. Through this research, the magma evolution and source will be understood in greater detail. Specifically, the magma mixing and/or assimilation of crustal material is assessed by measuring the strontium (Sr) isotopic compositions of individual plagioclase grains and of the whole rock. This will allow a greater understanding of magmatism in an enigmatic and unique tectonic setting. In addition to Sr isotope data, zoned plagioclase crystals in thin sections are analyzed using Auburn University Electron Microprobe Analyzer (AU-EMPA) for anorthite (An) values. By analyzing the An values, the evolution of the magma's calcium concentration is deduced, as plagioclase crystals readily incorporate Ca into its atomic structure at high (>1,000 ºC [Yu et al., 2014]) temperatures. The equilibrium temperature and pressure of the magma chamber can also be estimated using orthopyroxene-clinopyroxene thermometers. These equilibrium temperature and pressure data points can allow for a better understanding of the magma chamber conditions.

The main questions that this research aims to answer are as follows: Is the magma of the Ashi Volcano primarily crustal or mantle derived? To what degree has this magma been mixed and/or contaminated? How has the chemical composition of the magma evolved?

Background

Geologic Setting

The Tibetan plateau is the result of a continental collision and is quite a spectacular example. India was an island moving rapidly during Early Cenozoic at a rate of about 20 cm/year. During Eocene (~50 Ma) India collided with Asia, slowing to a rate of about 5 cm/year. This extreme change in speed resulted in major energy inputs allowing for the Tibetan plateau to be uplifted by the underthrusting Indian plate and subducted Neo-Tethyan seafloor (Chatterjee et al., 2013). This collision resulted in an elevation average of about 5 km for the Tibetan Plateau. The Tibetan crust has thickened to approximately double the thickness of average continental crust. The crust shortened in the north-south direction and stretched vertically during Eocene to Miocene by the collision of India into Asia (Dewey et al., 1988).

The area of the Tibetan Plateau between the Kunlun Shan and the Tarim Basin consists of exotic continental crustal terranes accreted to the Eurasian plate before the collision between India and Asia (Dewey et al., 1988). The accreted terranes are north of the Indus-Zangbo suture zone, which is the area where the entire Neo-Tethys Ocean was subducted. These terranes are bounded by outcrops of ophiolitic material and are interpreted as sutures (Chatterjee et al., 2013). The northernmost terrane is the Kunlun, with the Songpan-Ganzi, Qiantang, and Lhasa terranes to the south. These terranes, along with age and distribution of volcanic rocks, faults and other geological features are shown in Figure 1 (Xia et al., 2010).

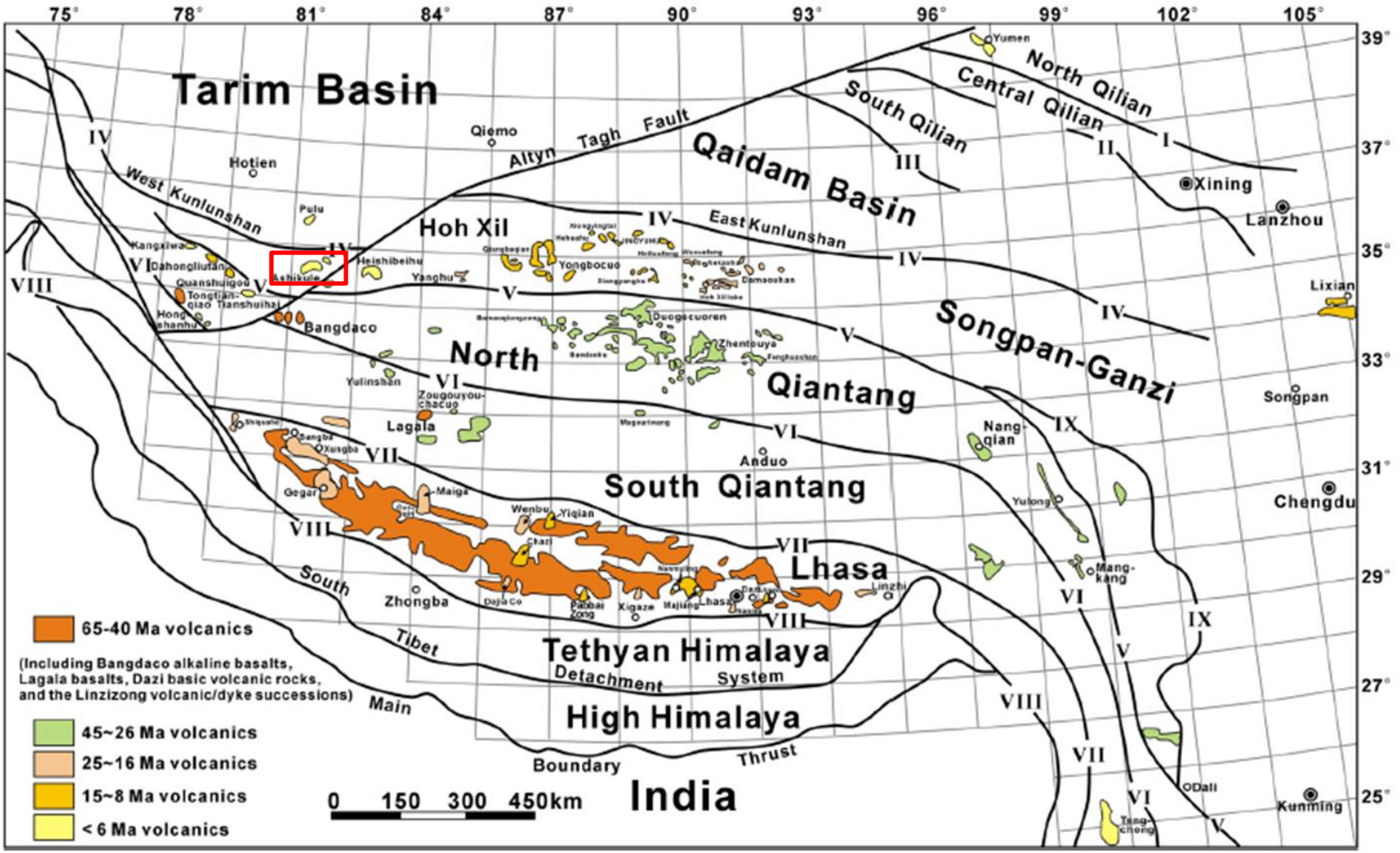

Figure 1- Modified from Xia et al., (2010). Distribution of terranes, volcanic outcrops and ages, and suture zones.

The Tarim craton is a notable craton in Central Asia (Zhang et al., 2013), as it has rigidly resisted deformation from the convergence of the Indian and Eurasian plate due to a strong Precambrian lithosphere and thick, heterogeneous Cenozoic sediments (Wang el al., 2003). The Tarim craton and the Tibetan plateau are separated by major transform faults, as shown in Figure 1. The Kunlun and Altyn Tagh faults accommodate the strain associated with the extreme pressure of the still advancing Indian plate (Figure 2).

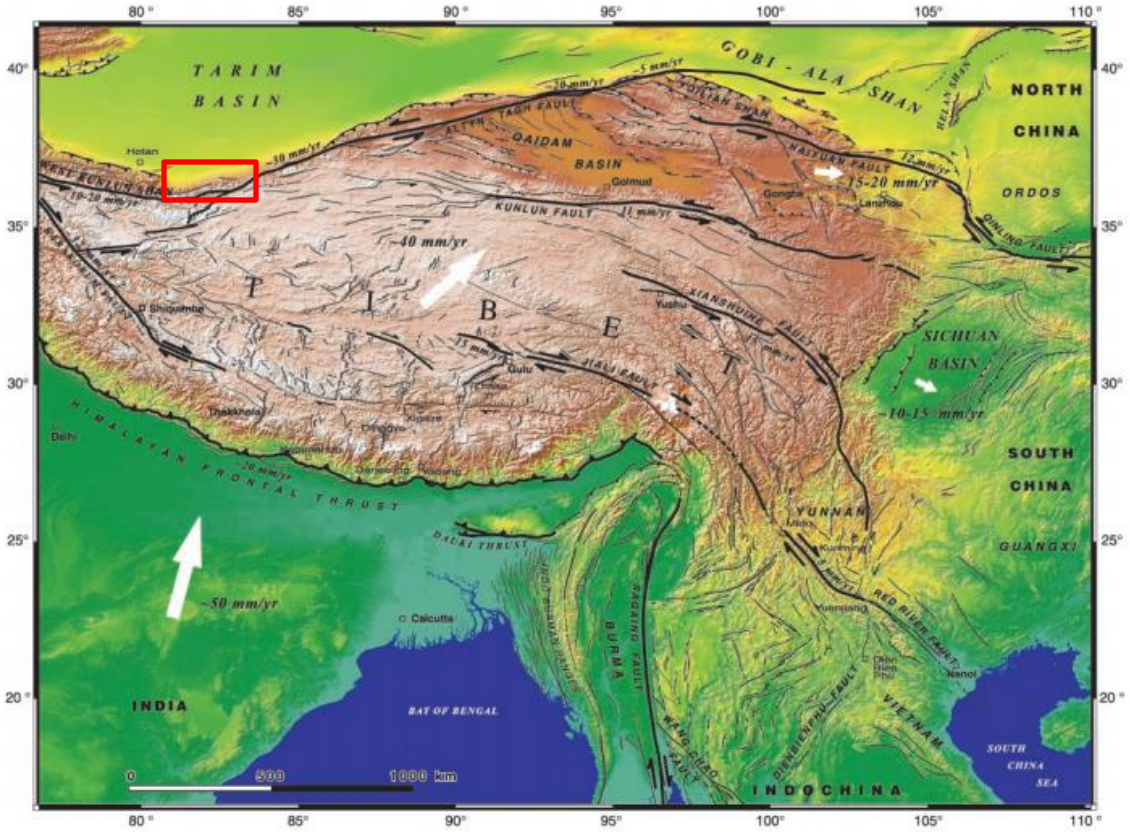

Figure 2- Regional map of the collision between the Indian plate and Eurasia. Continuing pressure from the still advancing Indian plate represented by the white arrow. From Tapponnier et al., (2001).

The Ashikule Basin is home to the AVC and is outlined in all presented maps by a red box. The Ashikile Basin resides on the northern margin of the Tibetan Plateau and is located at the junction of the Altyn Tagh Fault and the Kangxiwa Fault and is surrounded by the Kunlun Mountains. The AVC consists of fourteen major volcanoes and other volcanic features, such as lava flows and vents. The AVC covers an area of approximately 200 km^2. With an average elevation of about 5,000 meters, the AVC is one of the highest elevation volcanic fields in the world. The AVC has been volcanically active since the Late Pleistocene, with the Ashi Volcano erupting in 1951 (Xu et al., 2012).

The Ashi Volcano erupted explosively on May 27, 1951, as reported by Xinjiang Daily, a local newspaper. Some previous works referred to the Ashi Volcano as volcano number 1, although all research published in the past decade has adopted the name "Ashi". The spatial distribution of the Ashi Volcano, along with surrounding volcanoes, lakes, and geomorphological features are represented in Figure 3 (Xu et al., 2012). The Ashi Volcano is located directly south of Ashikule lake and to the north east of Wuluke lake. It is surrounded on all sides by lava flows.

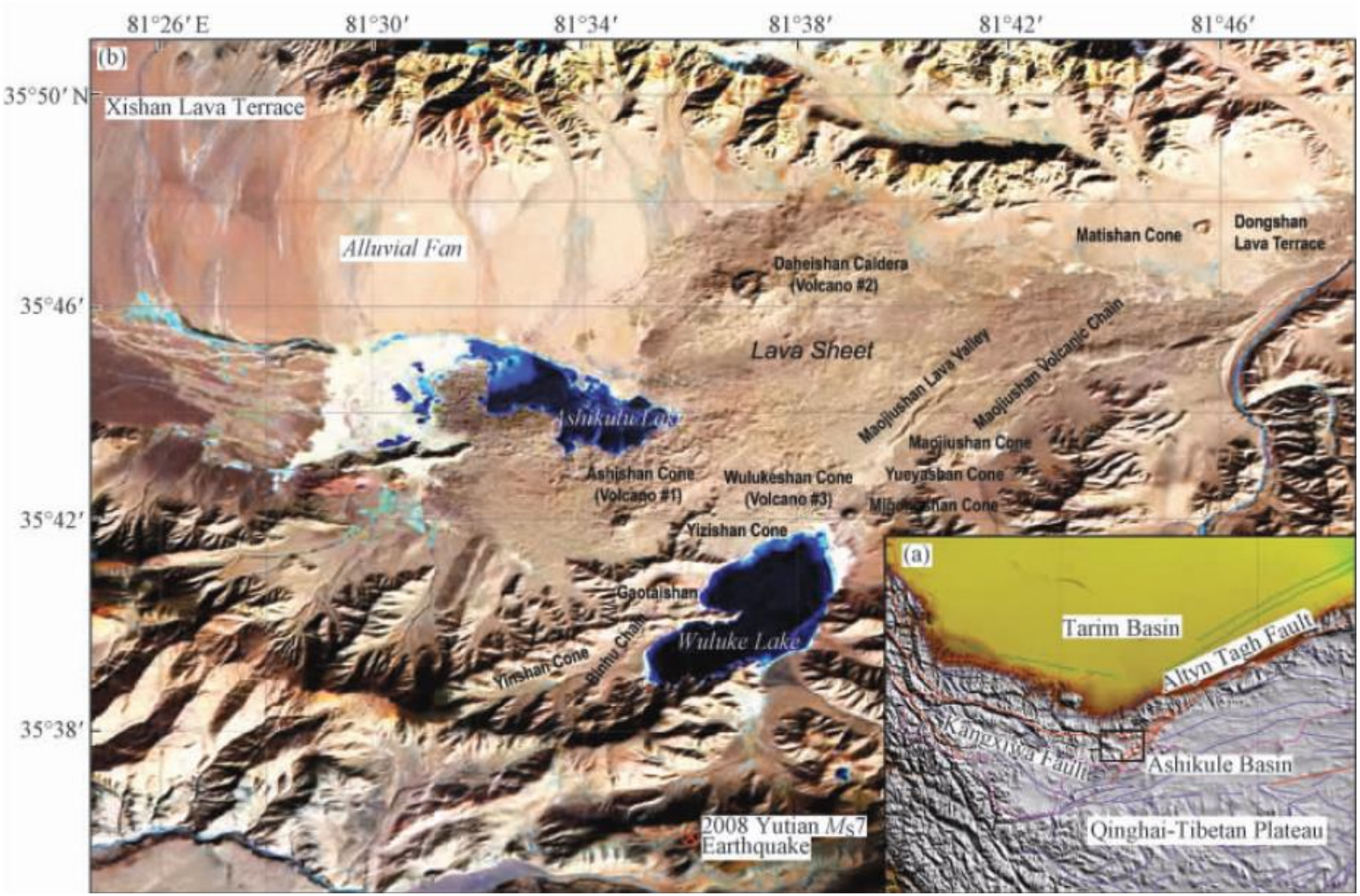

Figure 3- Modified from Xu et al., (2012). (a) Index showing location of Ashikule basin in relation to other tectonic features.

(b) Distribution of volcanoes, lakes, and other geomorphic features of the Ashikule basin.

Concerning Plagioclase

Plagioclase is a member of the feldspar group of framework silicates. Feldspars are the most abundant minerals in the earth's crust. Almost all igneous and metamorphic rocks contain feldspars, and they are an important component of many sedimentary rocks. Feldspars occur over a compositional range, shown in Figure 4. Plagioclase minerals can form under a wide range of pressures and temperatures, and their composition is controlled primarily by magma composition, temperature, and water content (Gao et al., 2014 and references therein). These characteristics of plagioclase make it an extremely useful mineral in determining the origin, composition, and evolution of the parent magma.

The minerals of primary interest in the current research are plagioclase, which has a compositional range of $CaAl_2Si_2O_8$-$NaAlSi_3O_8$. Plagioclase feldspars form a continuous solid solution series that is achieved by coupled substitutions at high temperatures. This means the Ca^{2+} will substitute for Na^{+}, since they are approximately the same size, while the charge balance is maintained through substituting Al^{3+} for Si^{4+}. Plagioclase composition is shown conventionally as a percentage of anorthite (An%), with the assumption that the remainder of the plagioclase composition is made up of albite. The plagioclase composition between pure albite ($NaAlSi_3O_8$) and pure anorthite ($CaAl_2Si_2O_8$) are also shown in Figure 4. Depending on the percentage of anorthite in a plagioclase crystal, the mineral may be assigned a more specific name of albite, oligoclase, andesine, labradorite, bytownite, or anorthite. Albite's An% is between 0-10%, oligoclase between 10-30%, andesine between 30-50%, labradorite between 50-70%, bytownite

between 70-90%, and anorthite >90%. An important note is that plagioclase is commonly altered to various clay minerals.

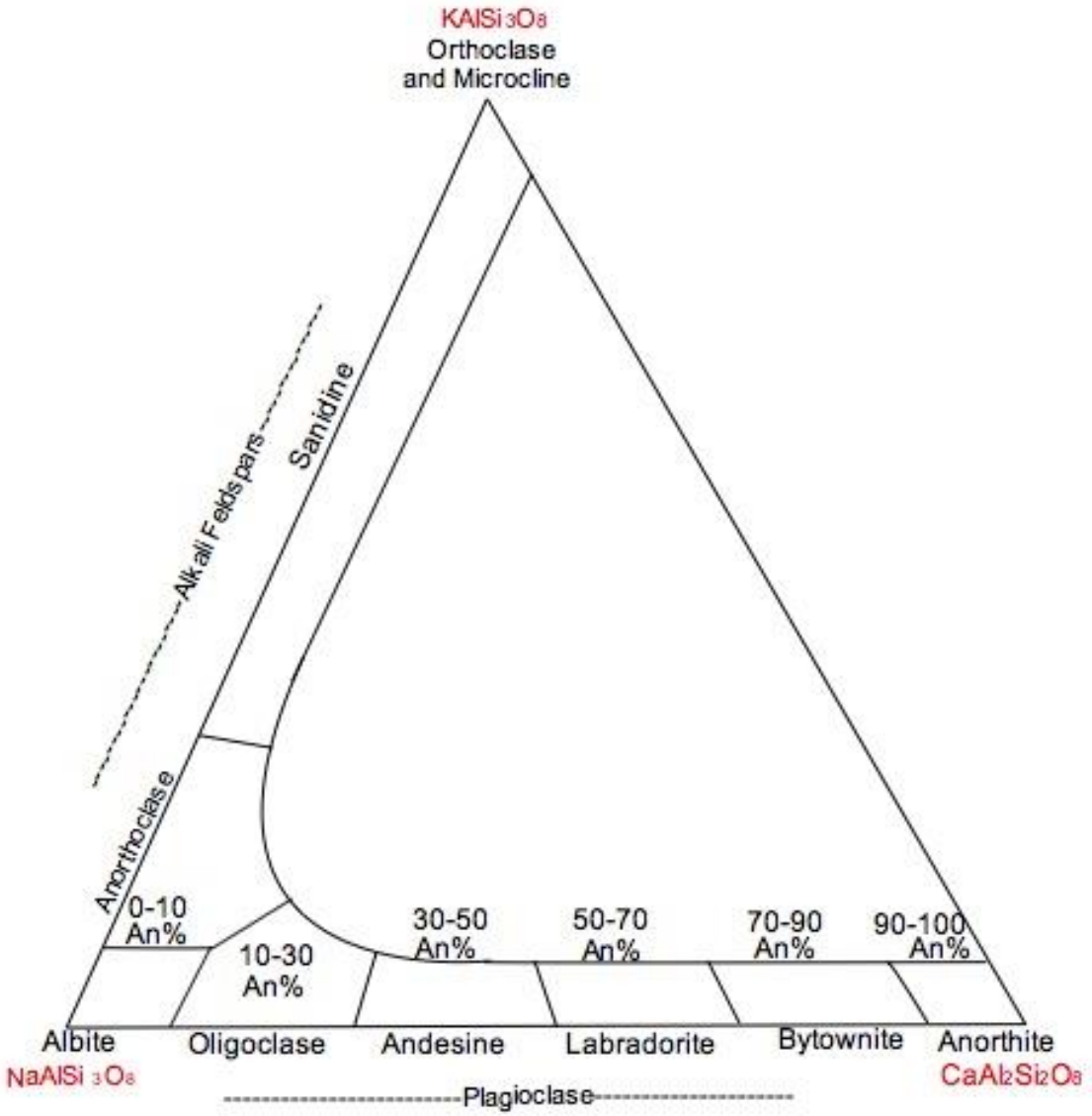

Figure 4- Feldspar compositional diagram.

Concerning Strontium

Strontium (Sr) is an alkaline earth metal that is a particularly important geochemical tracer when analyzing igneous rocks. Sr is a commonly occurring element in nature, being the 15th most abundant element on earth. The similar ionic radius and same charge (+2) of Sr allows it to easily substitute for Ca in the mineralogical structure of various minerals, specifically plagioclase. Many studies suggest that the Sr isotopic composition of plagioclase may be significantly different than the Sr isotopic composition of the matrix grains or whole rock (Gao et al., 2014 and references therein), making Sr ideal for analyses to determine petrogenetic processes. This variation in Sr concentrations is due to the property of strontium to chemically fractionate, or become concentrated in certain mineral phases such as plagioclase (Winter, 2013). Unlike major and trace element concentrations, $^{86}Sr/^{87}Sr$ ratio is not affected by processes such as partial melting and closed-system fractional crystallization. This property also makes Sr isotopes a useful tool for analyzing origin and evolution of magma, as the only way to change the $^{86}Sr/^{87}Sr$ ratio is through compositional changes due to the source or assimilation.

Natural Sr consists of four stable isotopes- ^{84}Sr, ^{86}Sr, ^{87}Sr, and ^{88}Sr (Faure and Mensing, 2005). Abundance varies due to radiogenic ^{87}Sr production. ^{87}Sr is produced through beta decay of ^{87}Rb, which has a half-life of 49 billion years. The Rb-Sr system is an extremely useful isotopic parent-daughter system for both age dating and petrogenetic studies. When analyzing Sr, it is common to use the ratio of $^{86}Sr/^{87}Sr$, since ^{86}Sr is stable and is not created as a product of the breakdown of any other element. Due to the extremely long half-life of Rb, we can assume that

the present-day $^{86}Sr/^{87}Sr$ ratio of the young Ashi volcanic rocks is representative of the $^{86}Sr/^{87}Sr$ ratio present in the melt at eruption, since the most recent eruption was in 1957 and not enough time has passed for significant post-eruption accumulation of radiogenic ^{87}Sr.

Early in the earth's history, there was significant fractional crystallization. This caused incompatible elements, such as Rb, to be preferentially incorporated into silicic residual melt. These silicic residual melts were the building blocks of the continental crust. The incompatible elements were excluded from basaltic melts, producing a continental crust with a higher Rb/Sr ratio than the upper mantle.

Previous Research

The location of the AVC has presented a daunting challenge for volcanologists and geochemists interested in the volcanoes of this region. As some of the highest elevation volcanoes in the world, there has been minimal research conducted on their origins, eruptive history, composition, and, in turn, the implications these data have on the tectonic history of the region. The AVC is remote and located at the base of the inhospitable West Kunlun Mountain Chain and there are no roads proximal to the region.

The first geological research on the AVC was done in the 1970s in order to investigate the reported volcanic activity of the region. The geologists conducted preliminary field work and discovered the presence of four volcanoes, naming them 1-4 (Zhao, 1976). In Zhao (1976) and other previous works, the Ashi Volcano was referred to as Volcano 1. Liu Jiaqi (1999) determined that the Ashikule group is composed lithologically of trachyandesite, trachybasalt, and tephrite which has since been confirmed (Yu et al., 2014; Wei et al., 2017). Later fieldwork in May of 2011 was conducted by geologists of the Institute of Geology, China Earthquake Administration and Earthquake Administration of Xinjiang Uygur Autonomous Regions. Their fieldwork uncovered more volcanoes (10 major ones total), determined eruption type, acquired structural data, and investigated approximate history of volcanic activity. The Ashi Volcano is on the south side of the Ashikule Basin and is widely considered to be the source of the most recent eruption of 1951 (Liu Jiaqi et al., 1990; Yu et al., 2014; Wei et al., 2017). The cone is well preserved and is 110 meters tall with the northern rim rising 26 meters taller than the southern

rim. The caldera is approximately 20 meters in diameter and is 48 meters deep. There are no obvious erosion features on the outside of the cone and is covered entirely in a thin layer of loess. Lava has flowed in all directions from the Ashi Volcano, with the flows entering Ashikule Lake to the north and butting up to the foot of a mountain to the south. By analyzing the structure of the Ashi Volcano, at least three stages of its formation can be decerned. The cinder cone was formed first with the mixing of country rock debris. The cinder cone is black and dark brown in color and has a gentle outer slope. The second stage of formation is characterized by cascading deposits that are dark brown and lining the crater rim. These were formed by splashdown accumulation, causing the inner slope of the cone to become steep. The last stage is marked by the formation of gas vents. These gas vents are about 2 meters in diameter. The gas vents shown in Figure 5 were found on the north rim of the cone (Xu et al., 2012).

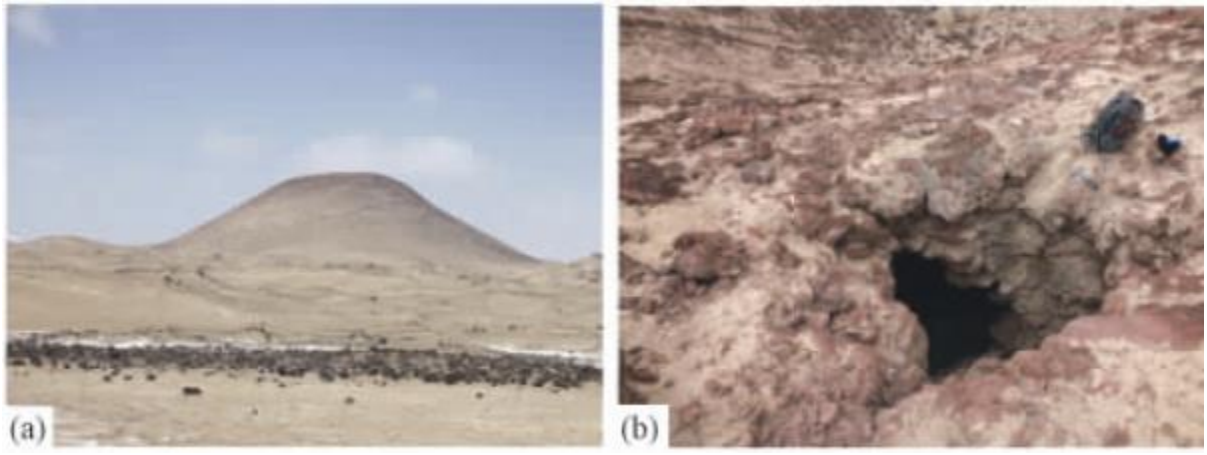

Figure 5- (a) Ashi Volcano viewed from the southwest. (b) Gas vent from the Ashi Volcano located on the northern rim.

Yu et al. (2014) conducted studies on the lithology, chemical composition, and texture of samples from the Ashi Volcano. Texturally, the Ashi Volcanic rocks are black or dark gray, vesicular, and have a porphyritic texture. The samples are mainly phenocrysts and groundmass, with the phenocrysts being mainly plagioclase and pyroxene with minor olivine and ilmenite. Yu et al. (2014) make a distinction between the samples collected based on the content of phenocrystic plagioclase verses pyroxene. They attribute this compositional variation to multiple, distinct magma pockets. There are two clusters of data points when considering phenocryst composition and oxide diagrams. Through x-ray fluorescence spectrometry, Yu et al. (2014) confirmed the composition of the Ashi volcanic rocks to be trachyandesite.

Yu et al. (2014) also analyzed the phenocryst composition of the Ashi volcanic rocks and found that the dominate phase of plagioclase is andesine, but that labradorite and oligoclase were also present. The An values of plagioclase grains with reaction rims is 30-40 at the core and 44-48 at the rims, indicating reverse compositional zonation. They interpret this as evidence that the crystals grew in an acidic magma that was afterwards mixed with a more basic magma. Figure 6 shows the An values and BSE images of the samples from which these conclusions were drawn.

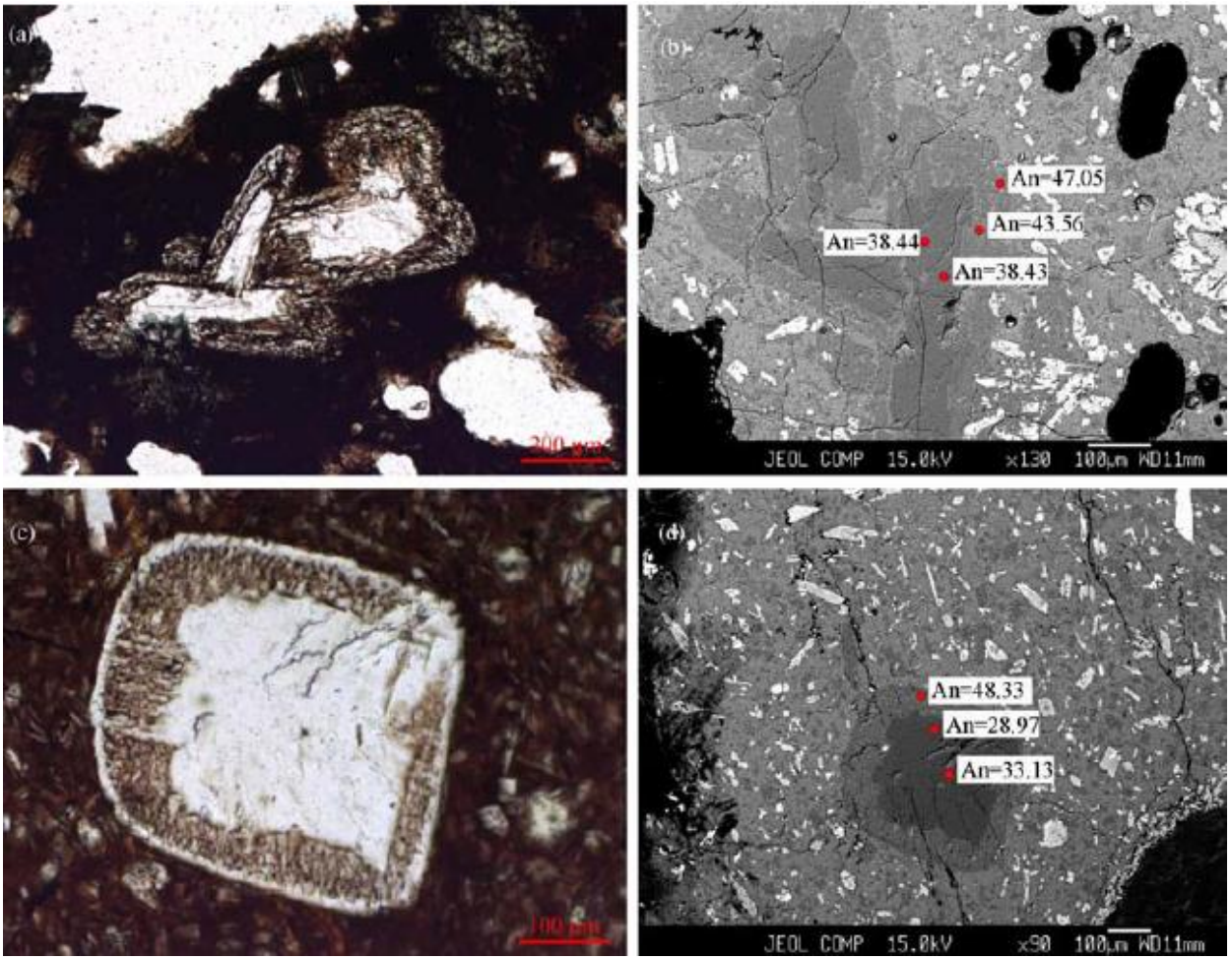

Figure 6- Modified from Yu et al. (2014). (a) Plagioclase crystal with reaction rim in plane polarized light. (b) BSE image of the plagioclase crystal shown in Figure 6a showing the An values of the core and rim. These plagioclase crystals exhibit reverse compositional zoning. (c) Plagioclase crystal with reaction rim in plane polarized light. (d) BSE image of the plagioclase crystal shown in Figure 6c showing the An values of the core and rim.

To determine information on the equilibrium temperature and pressure of the magma chamber, Yu et al. (2014) used the orthopyroxene-liquid thermometers proposed by Putirka (2008). The results correspond to their previous assertion that there are two interconnected magma chambers. In the group of pyroxene they distinguished as group A, the estimated equilibrium temperature is 1135-1176 ºC at 0.6-0.82 GPa, or a depth of 18-25 km. In the second group of pyroxene crystals, group B, the estimated equilibrium temperature is 1104-1143 ºC at 0.44-0. GPa, or a depth of 13-18 km. Yu et al. (2014) do note that Shen et al. (2013) obtained different results using the clinopyroxene-liquid thermobarometer method that would indicate the depth of the magma chamber is actually deeper, at 18-30 km. The equilibrium temperature and pressure of the magma chamber pre-eruption is a topic of ongoing research.

The most recent and most detailed work on the AVC was done by Wei et al. (2017). The broad scope of this study includes petrologic, geochemical, and seismic tomography analysis. Most pertinent to this research is their work on the whole-rock Sr isotopes of Ashi volcanic rocks, but also of interest is the whole-rock major and trace element analysis. The major element analysis confirmed the composition of the samples as trachyandesite [Figure 7a, Wei et al., (2017)]. All of the samples analyzed have a high K_2O (3.48-4.47 wt.%) and K_2O/ Na_2O (1.08-1.53) ratios, showing the composition to be shoshonitic [figure 7b, Wei et al., (2017)]. The trace element analysis is consistent with K-rich continental magmatism, as shown by elevated trace element concentrations.

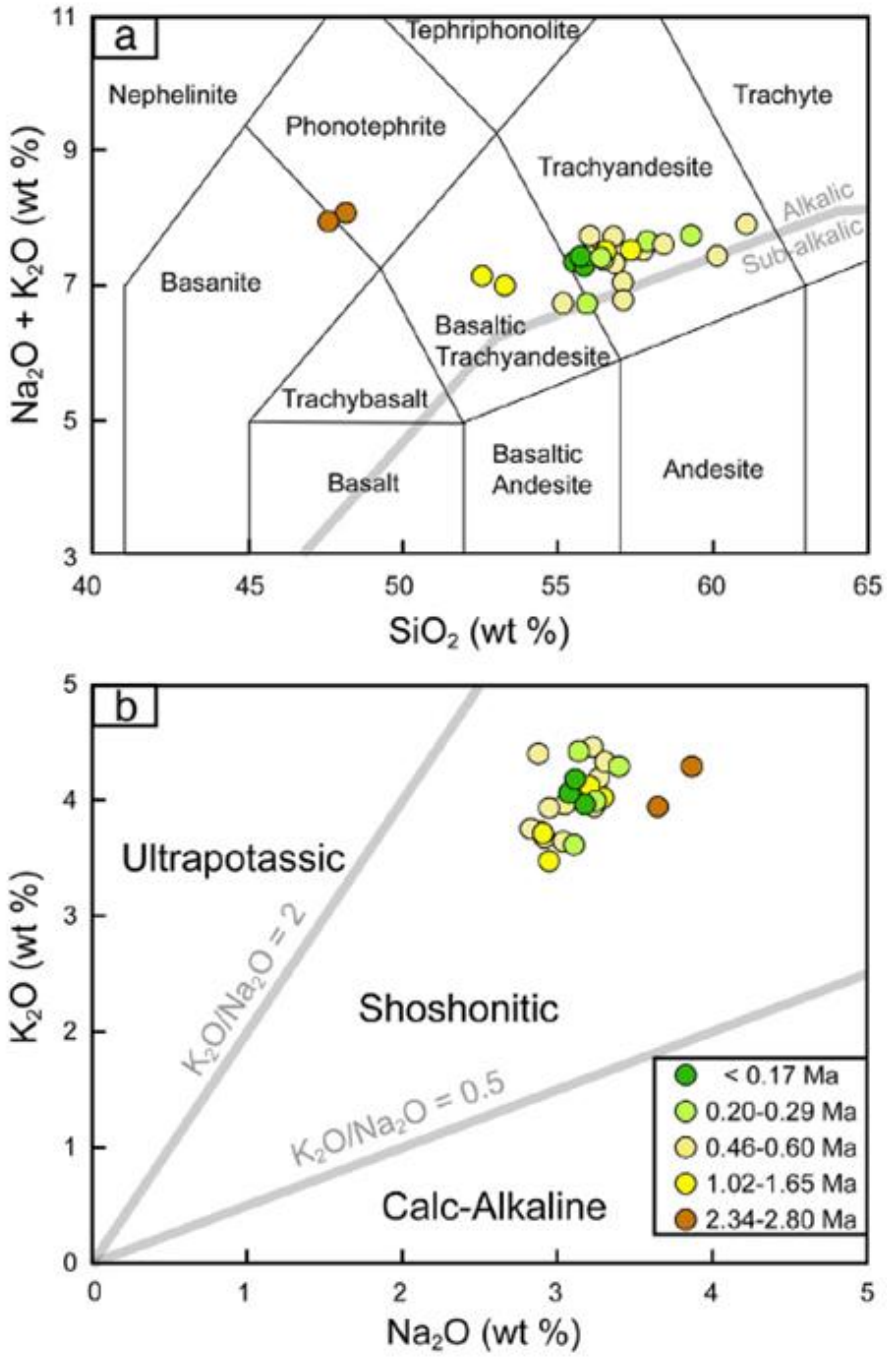

Figure 7- Modified from Wei et al. (2107). (a)- TAS diagram of samples from the AVC. The youngest samples (dark green) are clustered in the trachyandesite compositional field, with some minor overlap into the basaltic trachyandesite compositional field. (b)- K_2O and Na_2O compositional diagram showing the cluster of data in the shoshonitic compositional field.

The Sr isotope data from Wei et al. (2017) are presented in Table 1. The most relevant data are located under the Episodes 1 and 2 (Table 1), although all data from the six episodes are of interest. Whole rock samples were analyzed, a key factor when comparing the research presented in the following work. The results show enriched $^{87}Sr/^{86}Sr$ (0.707490-0.710523) relative to bulk silicate earth (BSE).

Episode (age)	Sample	$^{87}Sr/^{86}Sr$	Error (2σ)
1 and 2 (<0.17 Ma)	ASKL-3	0.710300	0.000005
1 and 2 (<0.17 Ma)	ASKL-4	0.710295	0.000005
1 and 2 (<0.17 Ma)	518–5	0.710337	0.000005
3 (0.20–0.29 Ma)	ASKL-10	0.710463	0.000005
3 (0.20–0.29 Ma)	513–11	0.710102	0.000005
3 (0.20–0.29 Ma)	518–9	0.710353	0.000005
4 (0.46–0.60 Ma)	ASKL-7	0.710516	0.000005
4 (0.46–0.60 Ma)	ASKL-8	0.710427	0.000005
4 (0.46–0.60 Ma)	ASKL-14	0.709738	0.000005
4 (0.46–0.60 Ma)	ASKL-15	0.709696	0.000005
4 (0.46–0.60 Ma)	ASKL-16	0.709871	0.000006
4 (0.46–0.60 Ma)	515–1	0.710016	0.000005
4 (0.46–0.60 Ma)	WLK-3	0.709887	0.000005
4 (0.46–0.60 Ma)	516–2	0.709870	0.000005
5 (1.02–1.65 Ma)	ASKL-5	0.710523	0.000005
5 (1.02–1.65 Ma)	516–11	0.708887	0.000005
5 (1.02–1.65 Ma)	518–14	0.709876	0.000005
6 (2.34–2.80 Ma)	ASKL-17	0.708650	0.000005
6 (2.34–2.80 Ma)	ASKL-18	0.707490	0.000005

Table 1- Modified from Wei et al. (2017). Enriched $^{87}Sr/^{86}Sr$ values compared to bulk silicate earth.

Wei et al. (2017) suggest the most recent Ashi eruption was caused by new magma input from the source. This was determined by correlations between Eu anomaly and MgO wt % and an increase in the MgO wt % (Figure 8). By comparing SiO_2 and $^{87}Sr/^{86}Sr$ values (Figure 9), Wei et al. (2017) also suggest that the younger AVC lavas did not experience significant crustal contamination, despite thick continental crust. The limited range of SiO_2 and extremely restricted $^{87}Sr/^{86}Sr$ values are how Wei et al. (2017) determined that there was minimal crustal contamination, since significant contamination would likely yield $^{87}Sr/^{86}Sr$ values closer to 0.716, which is an approximate $^{87}Sr/^{86}Sr$ ratio expected in continental crust. The proposed mechanism for AVC magma generation is partial melting of metasomatized sub-continental lithospheric mantle (SCLM), which is the proposed mechanism for potassic magmatism in much of Tibet (Cooper et al., 2002; Turner et al., 1993, 1996; Williams et al., 2004).

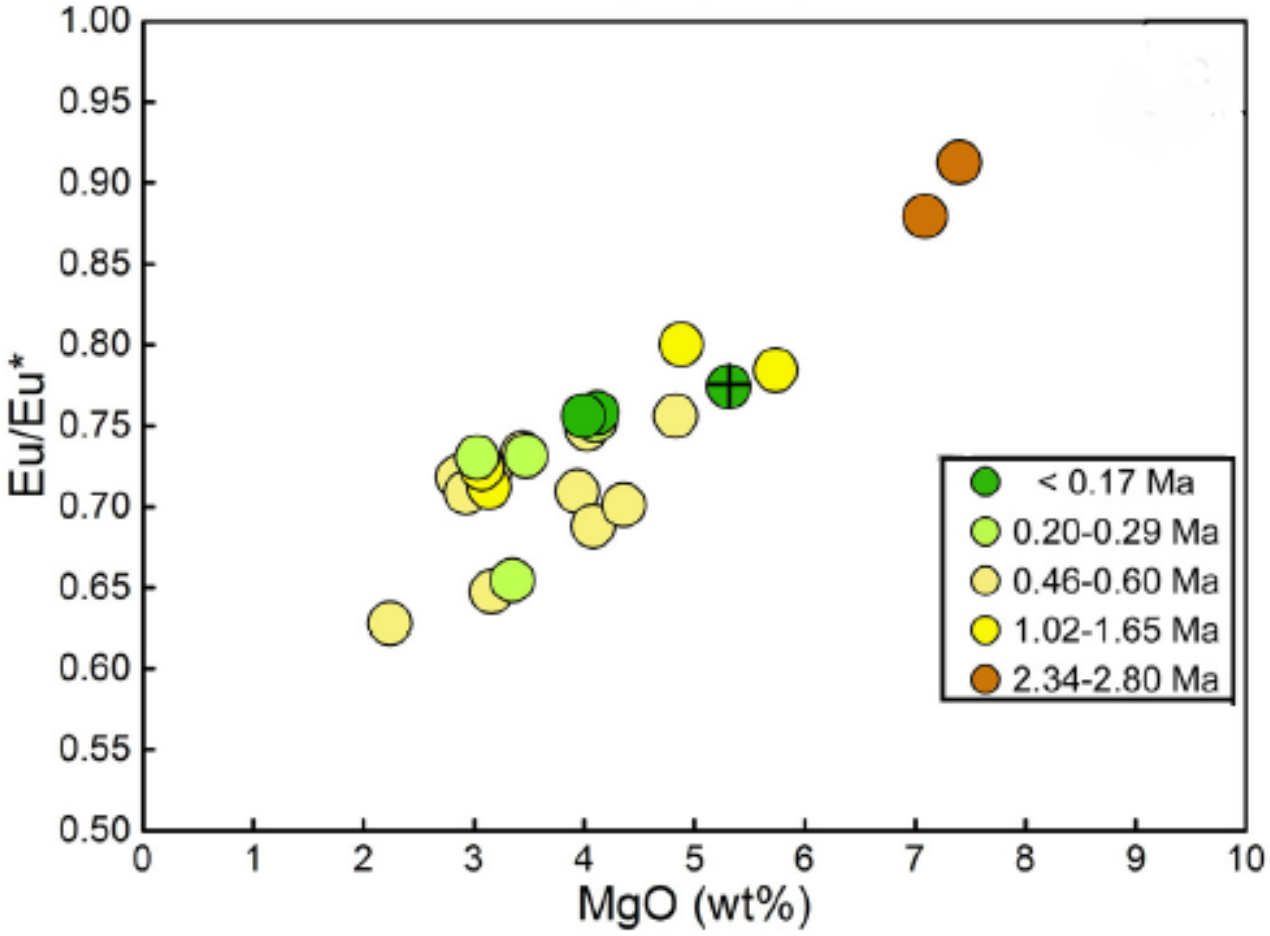

Figure 8- Modified from Wei et al., (2017). Eu vs. MgO wt %. Samples of main interest are represented by dark green, with data of samples from the most recent eruption shown in green with the cross inside.

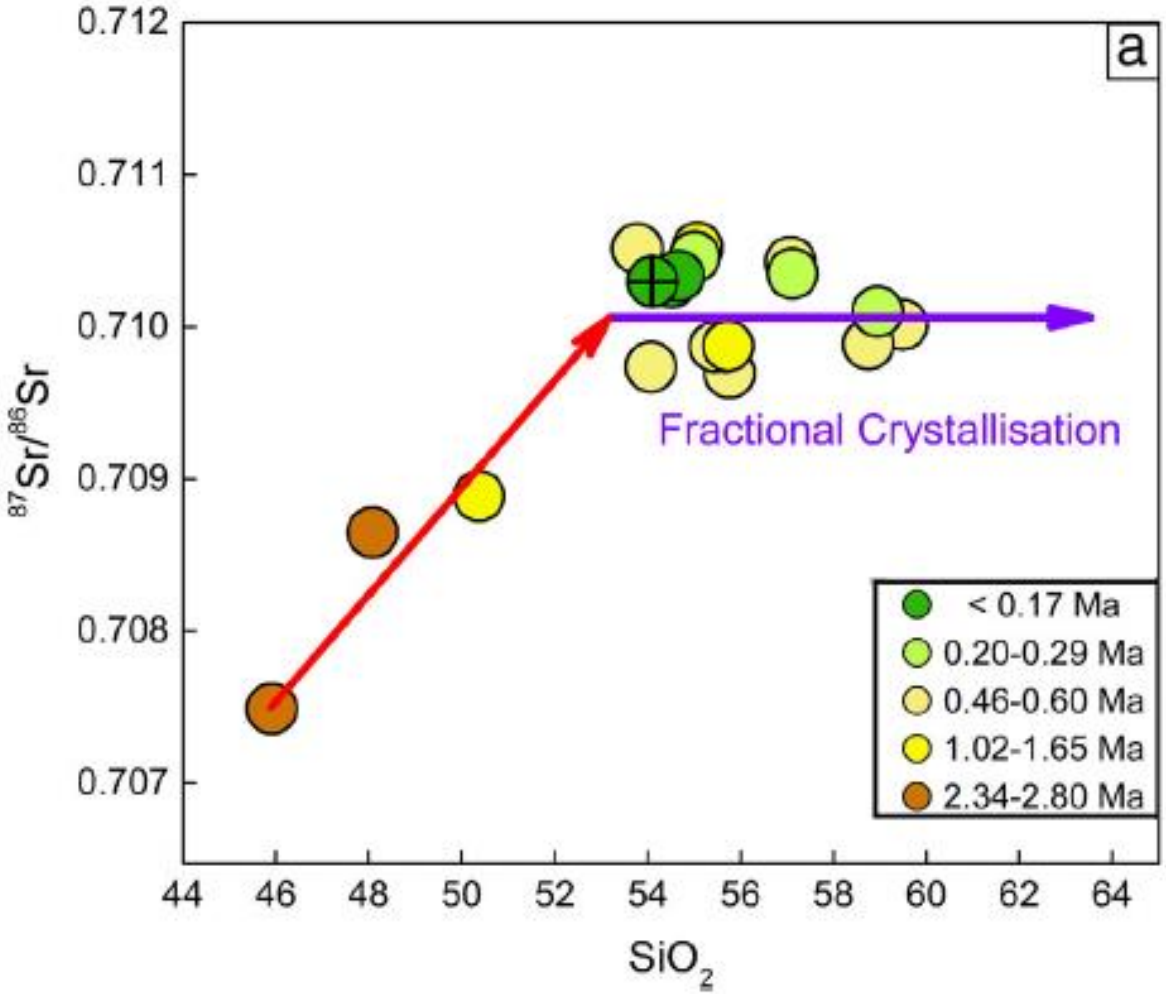

Figure 9- Modified from Wei et al., (2017). $^{87}Sr/^{86}Sr$ values compared to SiO_2. Samples of main interest are represented by dark green with data of samples from the most recent eruption shown in green with the cross inside.

Materials and Methods

Sample Preparation

Due to the remote location of the AVC, the samples in this research were collected by an outside geological team and donated for use in this research. Two rock samples were selected for this research from the donated samples, sample 513-4-b and sample 513-7, both of which are shown in Figure 10.

For TIMS analyses, electron microprobe analyses, and optical analyses, the samples had to be cut into billets, or smaller pieces. This was done using a compound miter saw in Auburn University's sample preparation lab. A few small pieces were used for plagioclase extraction, while the rest were sent to Wagner Petrographic for polished thin and thick section preparation.

$^{87}Sr/^{86}Sr$ Data Collection

The first step in the $^{87}Sr/^{86}Sr$ data collection was to mechanically separate the plagioclase grains. This was done with a rock hammer to first break down the sample. The sample aggregate was then ground with a mortar and pestle to a powder and sieved to isolate grains in the φ range of 3 to 2. The isolated sample was then picked for plagioclase grains using needle nose tweezers and a binocular microscope. Approximately 35 grains were picked for each sample. The grains were placed in 3N hydrochloric acid (HCl) to dissolve secondary carbonate grains that were indistinguishable from plagioclase under the binocular microscope. The grains

were washed with deionized water and dried in an oven. The remaining grains were then placed in an ultrasonic bath to separate out any grains that were not plagioclase. The floating grains were discarded and remaining grains again dried.

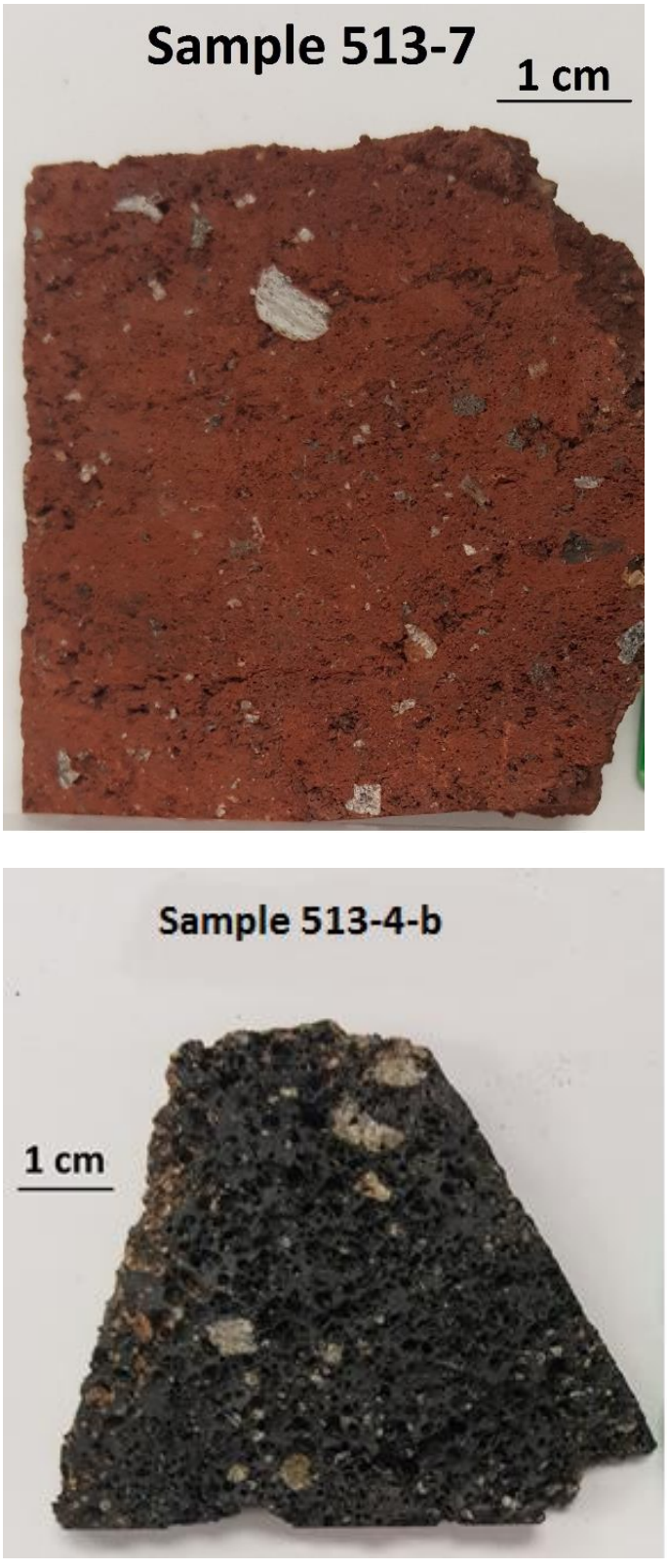

Figure 10- Images of samples from Ashi Volcano which were used in the following research.

Sr ions were chemically separated from dissolved plagioclase by ion exchange chromatography in a trace metal clean room and measured at Auburn University in Dr. Haibo Zou's Radiogenic Isotope Laboratory in the Department of Geosciences (Figure 11) under the direction of Dr. Zou. Single-grain plagioclases were weighed individually using an analytical balance and were placed into 7 ml Teflon screw-top beakers. The grains were dissolved by a 3:1 mixture of concentrated ultrapure HF and HNO_3 on a hot plate at ~100 °C for several days. After plagioclase grains were completely dissolved, the caps of the Teflon beakers were removed and the solution was evaporated on the hot plate. The dried samples were then dissolved by 7N HNO_3 and evaporated to dryness. The 7N HNO_3 process was repeated one more time. Finally, samples are dissolved by 2N HNO_3 and transferred to 1.5 ml centrifuge tubes.

Figure 11- Images of trace metal clean room. a.) Polypropylene horizontal flow acid hood (right) and Millipore water purification system (left). b.) Microzone polypropylene vertical flow workstation for ion exchange column chemistry.

Micro columns are filled with 0.25 ml Eichrom Sr-resin (Figure 12a). After cleaning and conditioning of the Sr-resin, centrifuged solutions in 2N HNO_3 were loaded to the micro columns. The micro columns were washed by 2N, 7N and 3N HNO_3 to remove non-Sr ions (Figure 12b). Very dilute (0.05N) HNO_3 were used to collect Sr. The column chromatography separation procedure is adapted from Mikova and Denkova (2007).

Strontium isotopic compositions were analyzed by a thermal ionization mass spectrometer (TIMS, Finnigan MAT 262) at the Trace Metal Isotope Laboratory at Auburn University for measuring radiogenic and stable isotopes of trace metals. The multi-collector MAT 262 is equipped with 8 Faraday cups and a secondary electron multiplier. Purified Sr samples were picked up from Teflon beakers using dilute (0.25 N) HNO_3 and were mixed with 1 microliter TAPH solution (Zou, 1999; Zou et al., 2000). The mixture is then loaded onto degassed rhenium filaments as ionization filaments. Sr samples on the single Re filaments are dried at 0.7 ampere (A). The filament current is then slowly increased to 2.0 A until all H_3PO_4 is evaporated, and finally is flushed very briefly at 3.0 A. Filaments with Sr samples are then mounted to a sample magazine that can hold up to 13 samples. The magazine is loaded to the ion source of MAT-262. Vacuum in the ion source and mass analyzer of the mass spectrometer is kept at below 10^{-7} Torr. Purified Sr samples are thermally ionized by passing a current through the filaments in the ion source. An accelerating voltage of 10 KV is used to accelerate Sr^+ ions from the ion source into the magnetic sector mass analyzer. Dynamic jumping mode is used for Sr isotope analyses. Sr isotopic compositions are normalized to $^{86}Sr/^{88}Sr$ of 0.1194.

a.)

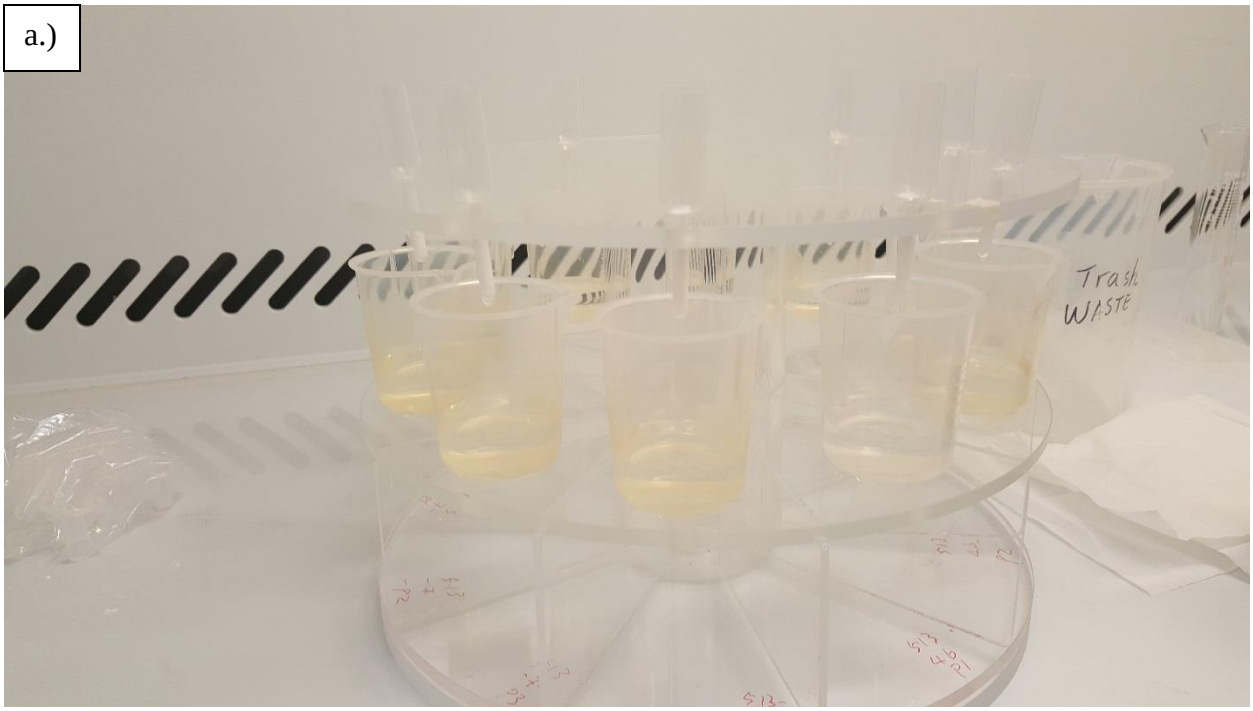

b.)

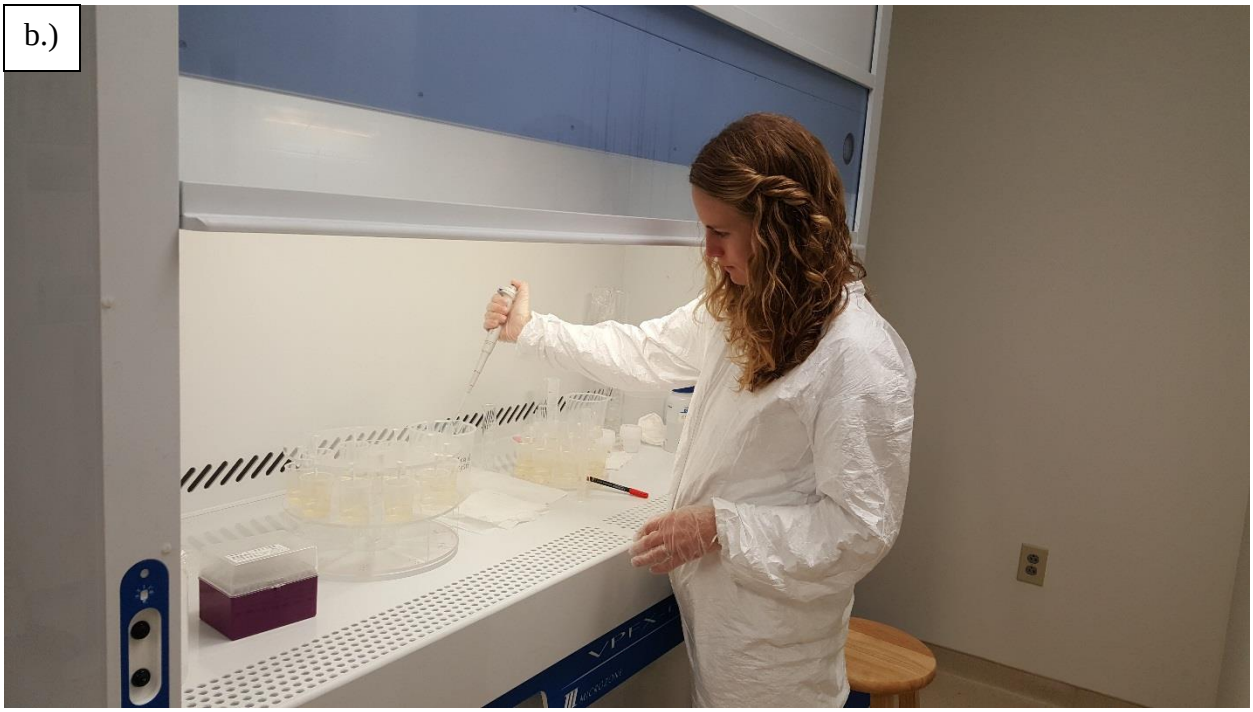

Figure 12- a.) Micro columns are filled with 0.25 ml Eichrom Sr-resin. b.) The micro columns were washed with HNO_3 to remove non-Sr ions.

Electron Microprobe

Two polished thick sections (100 microns) and two thin sections were made by Wagner Petrographic. Each sample, sample 513-4-b and sample 513-7, had one thick and one thin section made from it. Before analyzing the mineral compositions of the thick sections, the thin sections were analyzed to identify minerals and determine textural relationships.

To prepare the thick sections for analysis, the thin sections were then placed in a carbon vacuum evaporator to coat the samples in carbon. This creates an electrically conductive surface and prevents charge accumulation. The samples were then loaded into the sample holder and input into the Auburn University Electron Microprobe Analyzer (AU-EMPA), shown in Figure 13. The AU-EMPA was standardized to Amelia albite and anorthite. To analyze the composition of various mineral phases, EDS spectrums were generated to confirm phase composition and then point analyses and line analyses were performed on several mineral grains. BSE and compositional maps were also created of multiple phases.

Figure 13- Auburn University Electron Microprobe Analyzer (AU-EMPA).

RESULTS

Optical Petrography

Sample 513-4b is highly vesicular with a porphyritic texture (Figure 14 a and b). The phenocrysts are mainly plagioclase (Figure 14 c and d) and some pyroxene (Figure 15). There is significantly more plagioclase than pyroxene, with visual estimates being that the phenocrysts are ~70% plagioclase and ~30% pyroxene by volume. About 65% of the pyroxene displays glomeroporphyritic texture (Figure 16). Ilmenite and geikielite are also present in minor amounts (Figure 17). The plagioclase phenocrysts are generally euhedral to sub euhedral, some exhibiting a reaction rim (Figure 18). Some plagioclase grains exhibit a peculiar habit, where the grain is mainly euhedral but the center is filled with groundmass (Figure 19). While this is an unusual texture, it is a minor occurrence and thus not likely a significant feature. The edge of vesicles exhibits an amygdular texture, with the vesicles containing sericite (Figure 20). The groundmass is mainly glass with microplagioclase and micropyroxene.

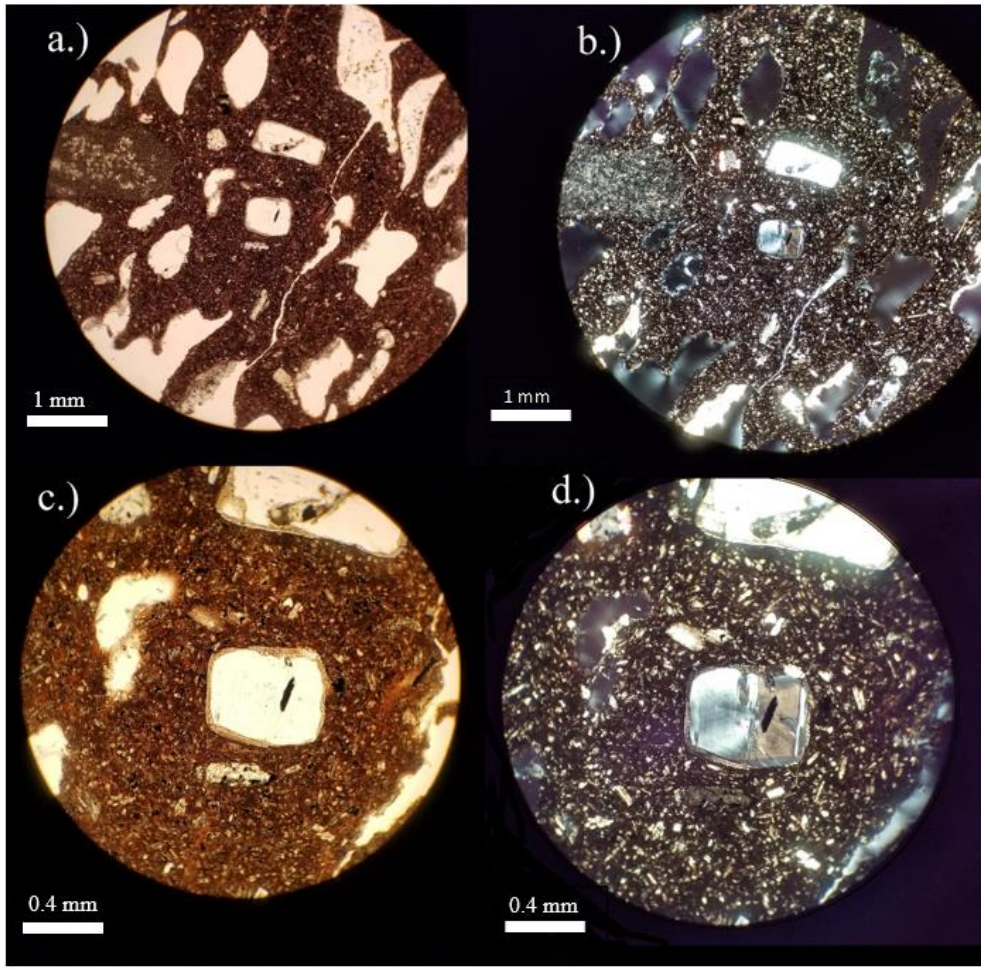

Figure 14–a.) Porphyritic texture of sample 513-4b in PPL at 4x magnification. b.) Same as 14-a but in XPL. Note zoned plagioclase phenocrysts, vesicles, and glassy groundmass. c.) Plagioclase phenocryst at 10x magnification in PPL. d.) Plagioclase phenocryst at 10x magnification in XPL. Note the rim of the plagioclase.

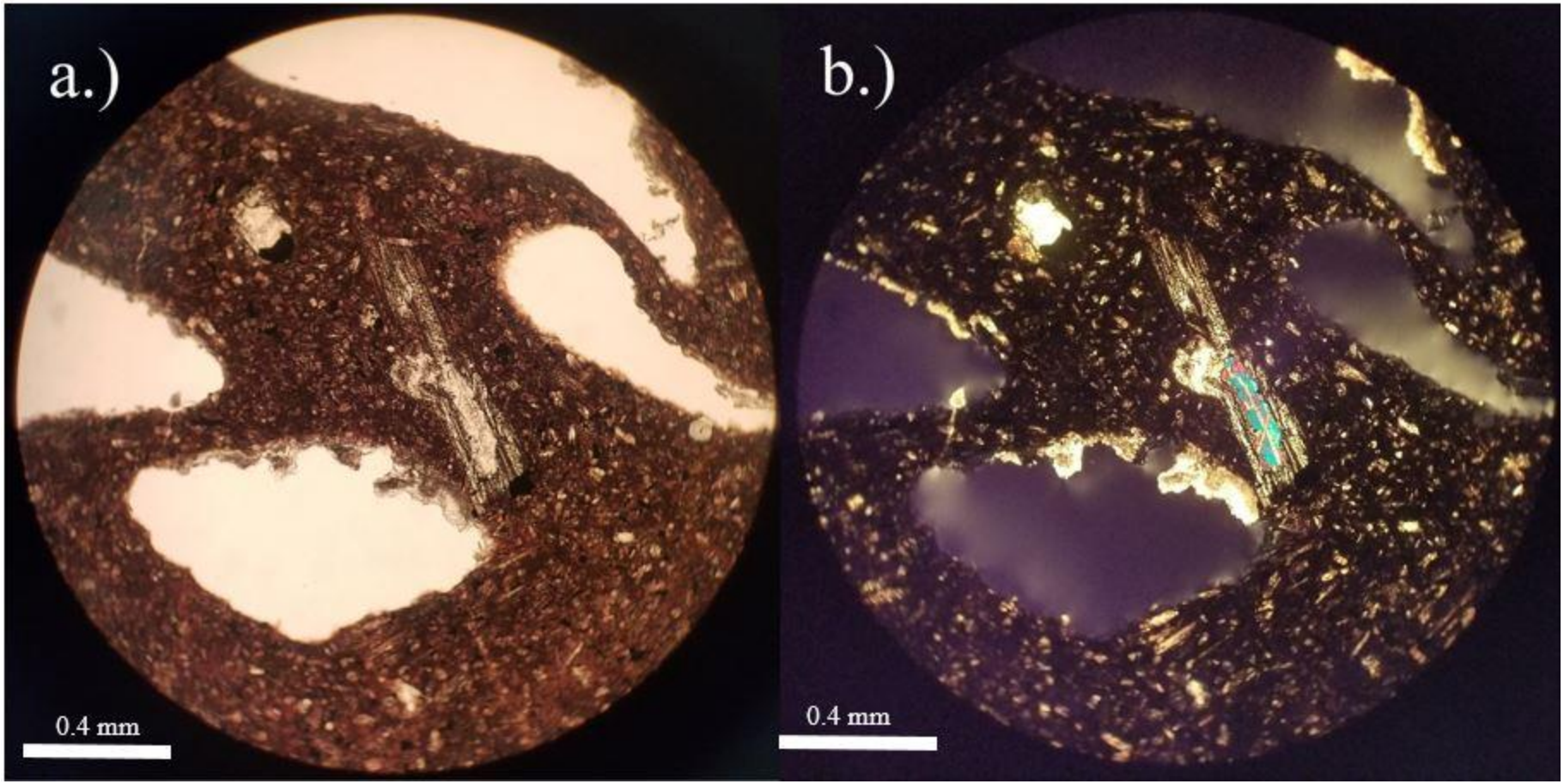

Figure 15- a.) Image of pyroxene (center) at 10x magnification in PPL. b.) Same pyroxene at 10x magnification in XPL. The pyroxene has a considerably sized reaction rim that is apparent in this image.

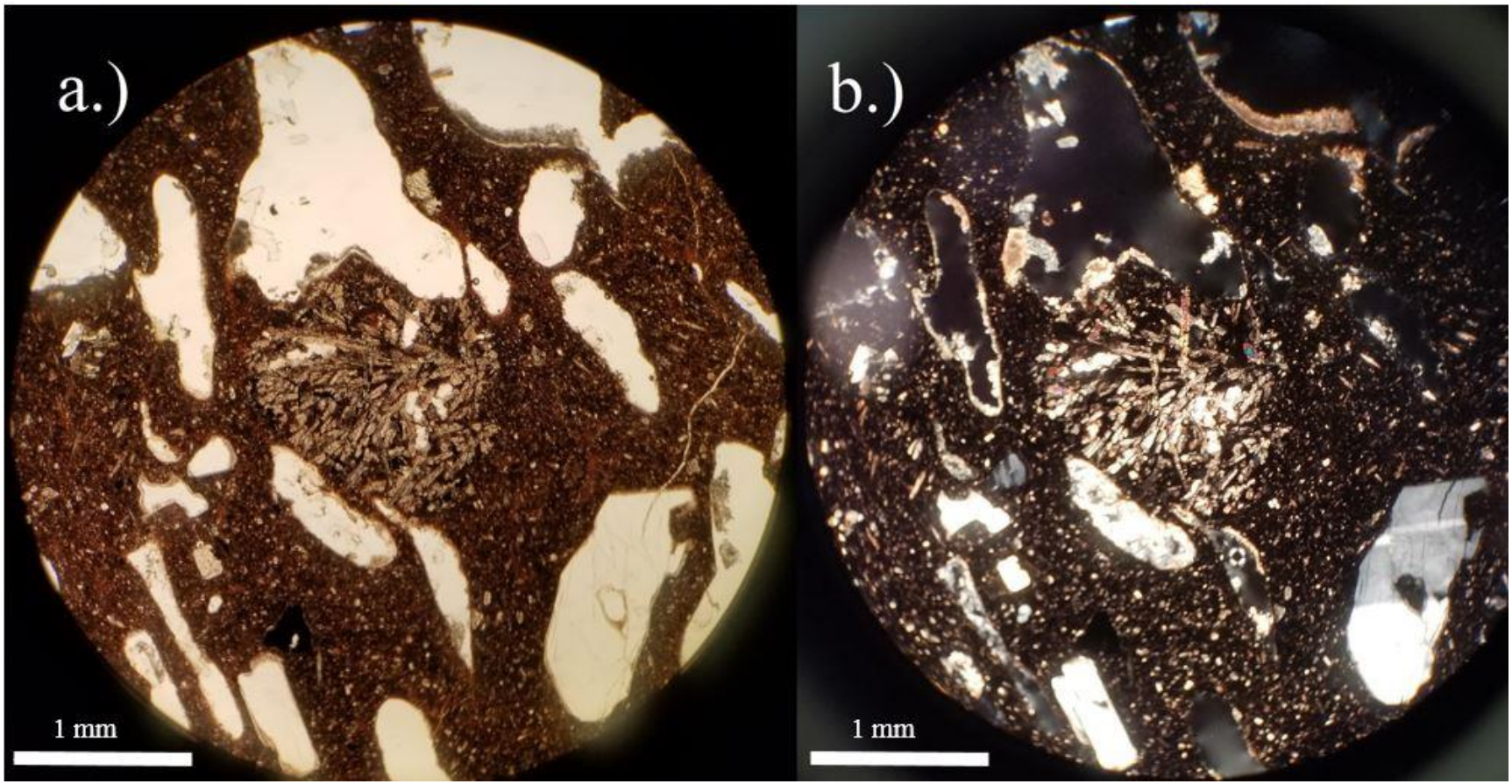

Figure 16- a.) Image of pyroxene displaying glomeroporphyritic texture at 4x magnification in PPL and b.) in XPL.

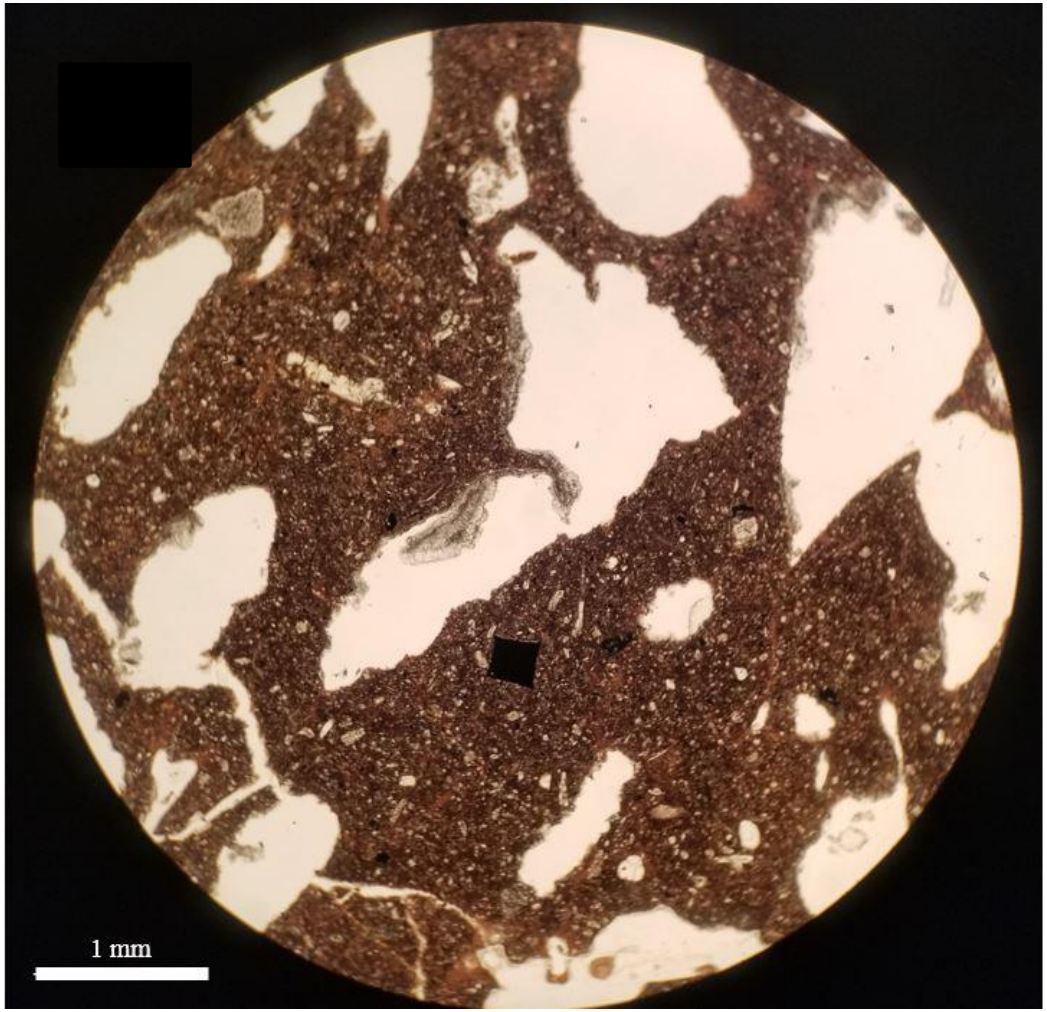

Figure 17- The opaque, euhedral mineral phase is ilmenite and geikielite, shown in PPL at 4x magnification.

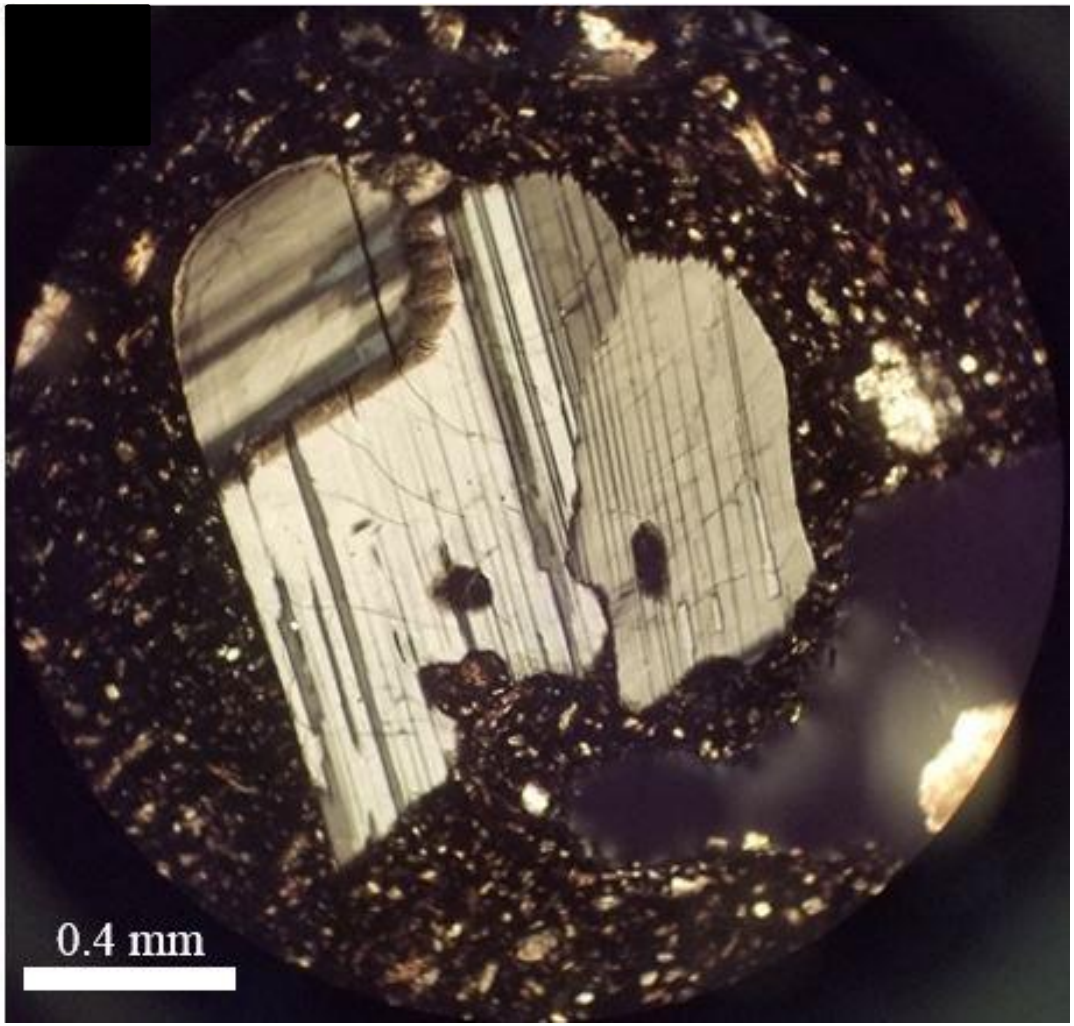

Figure 18- a.) Subeuhedral plagioclase in XPL at 10x magnification. Plagioclase exhibits albite twinning. The visible groundmass is glass with microplagioclase and micropyroxene.

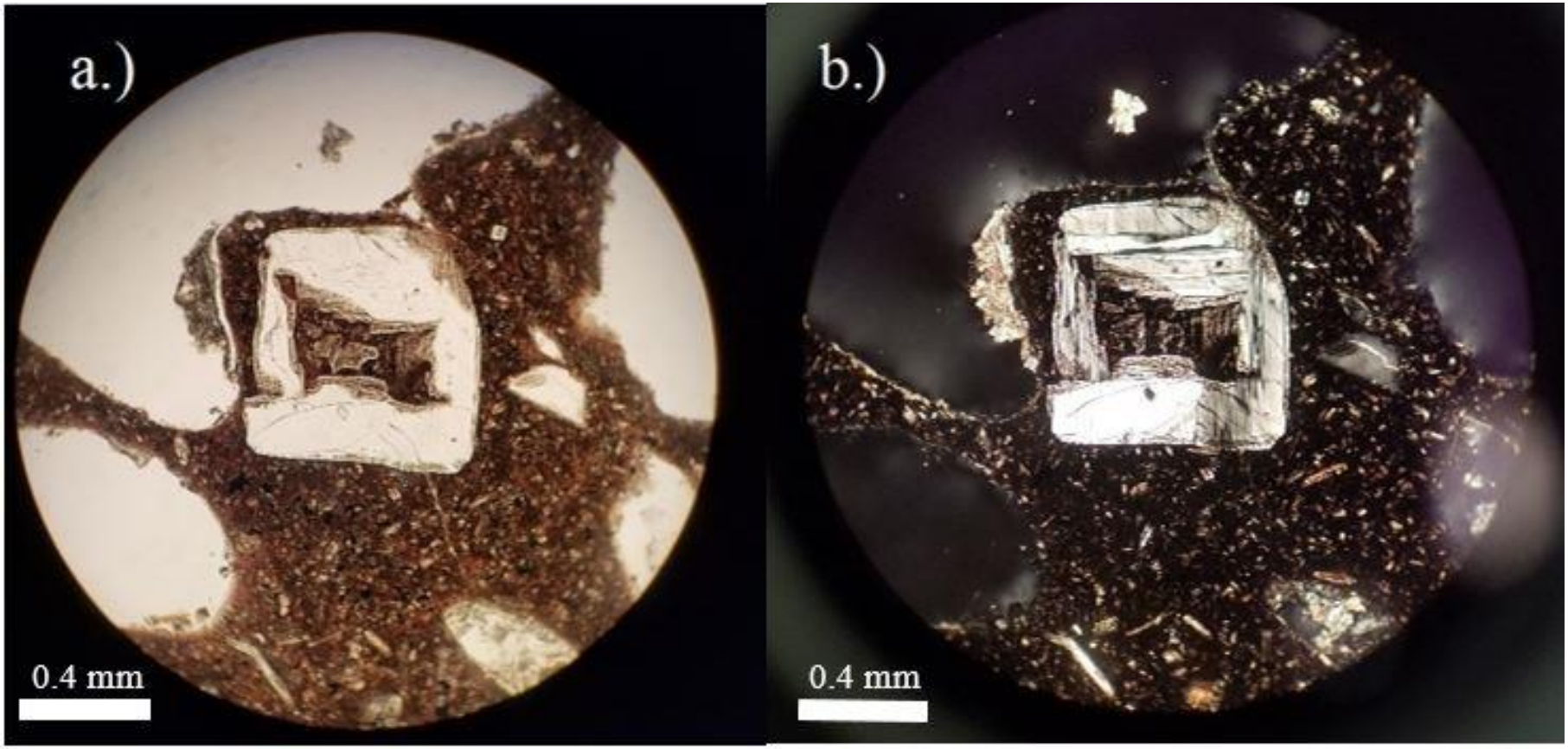

Figure 19- a.) Euhedral to subhedral plagioclase grain at 10x magnification in PPL. b.) Same plagioclase grain as a.) in XPL.

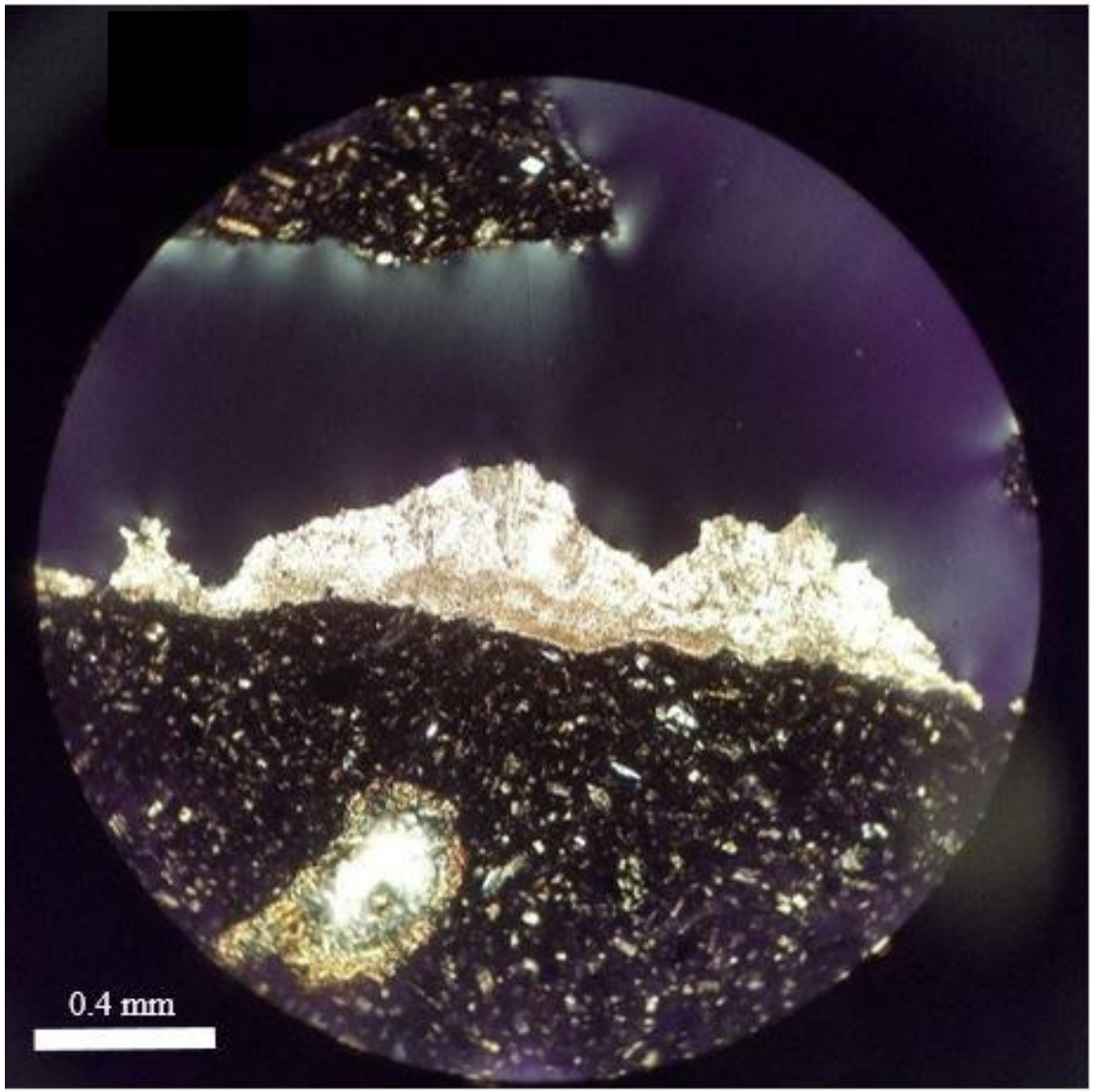

Figure 20- Sericite lining edge of vesicle viewed at 10x magnification and in XPL.

Sample 513-7 is also vesicular with a porphyritic texture, and the phenocryst composition is mainly pyroxene and plagioclase, shown in Figure 21. There is both orthopyroxene and clinopyroxene present in this sample, shown in Figure 22. Figure 23 shows sillimanite in a potassium feldspar, and is the only occurrence of this fibrous mineral phase. This mineral is interesting, since sillimanite is almost exclusively found in metamorphic rocks. The sillimanite and potassium feldspar phase likely is a xenocryst. The protolith of this suspected xenocryst was likely a phyllite or schist. The groundmass is almost entirely glass and has a rusty red color.

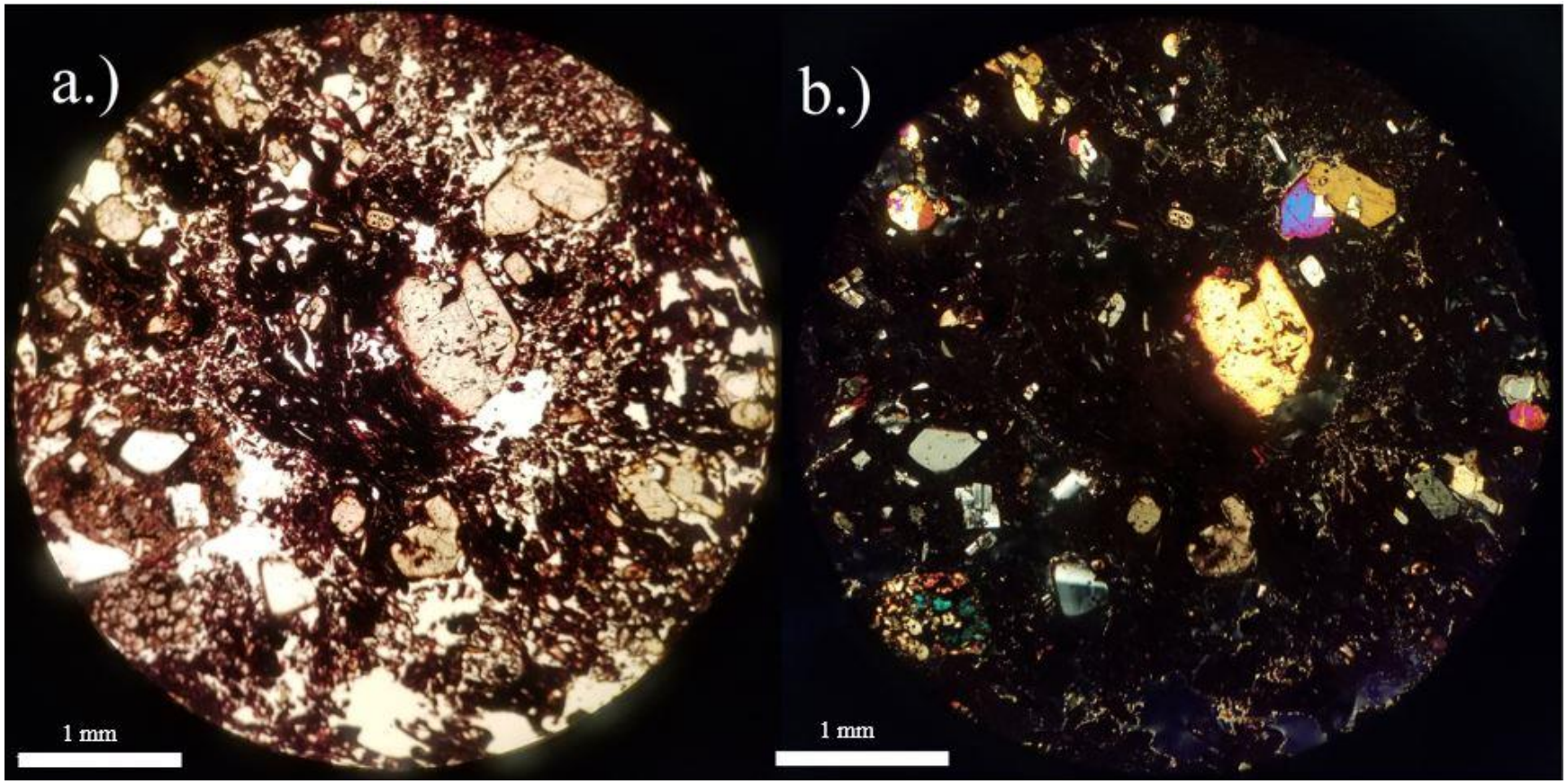

Figure 21- a.) PPL image at 4x magnification of pyroxene and plagioclase. b.) XPL image of same view as image a.

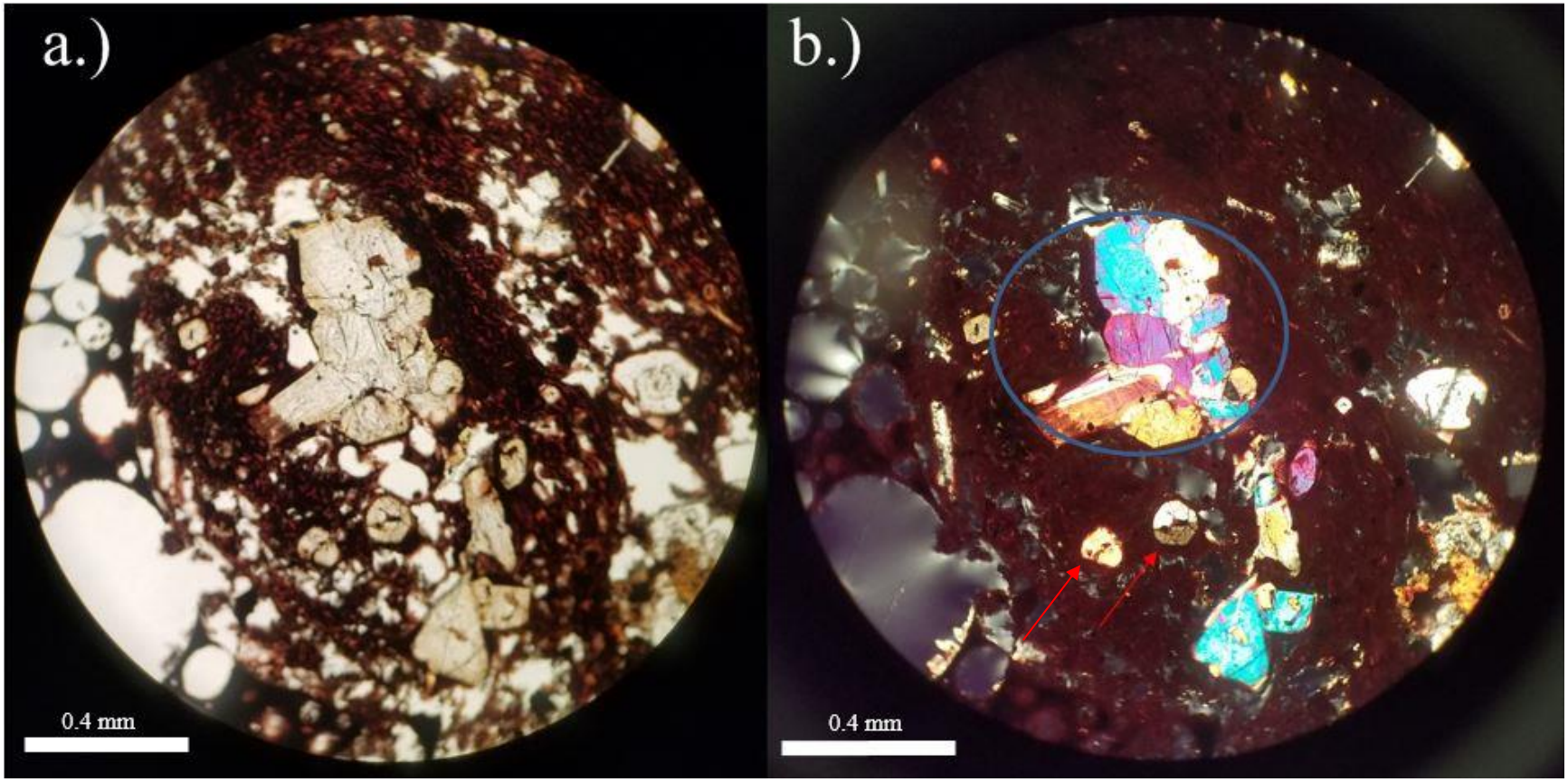

Figure 22- a.) PPL image at 10x magnification. Cleavage of pyroxene visible in central crystal. b.) XPL image at 10x magnification showing OPX and CPX. The large center crystal is primarily CPX (outlined in blue), while the OPX is denoted by red arrows.

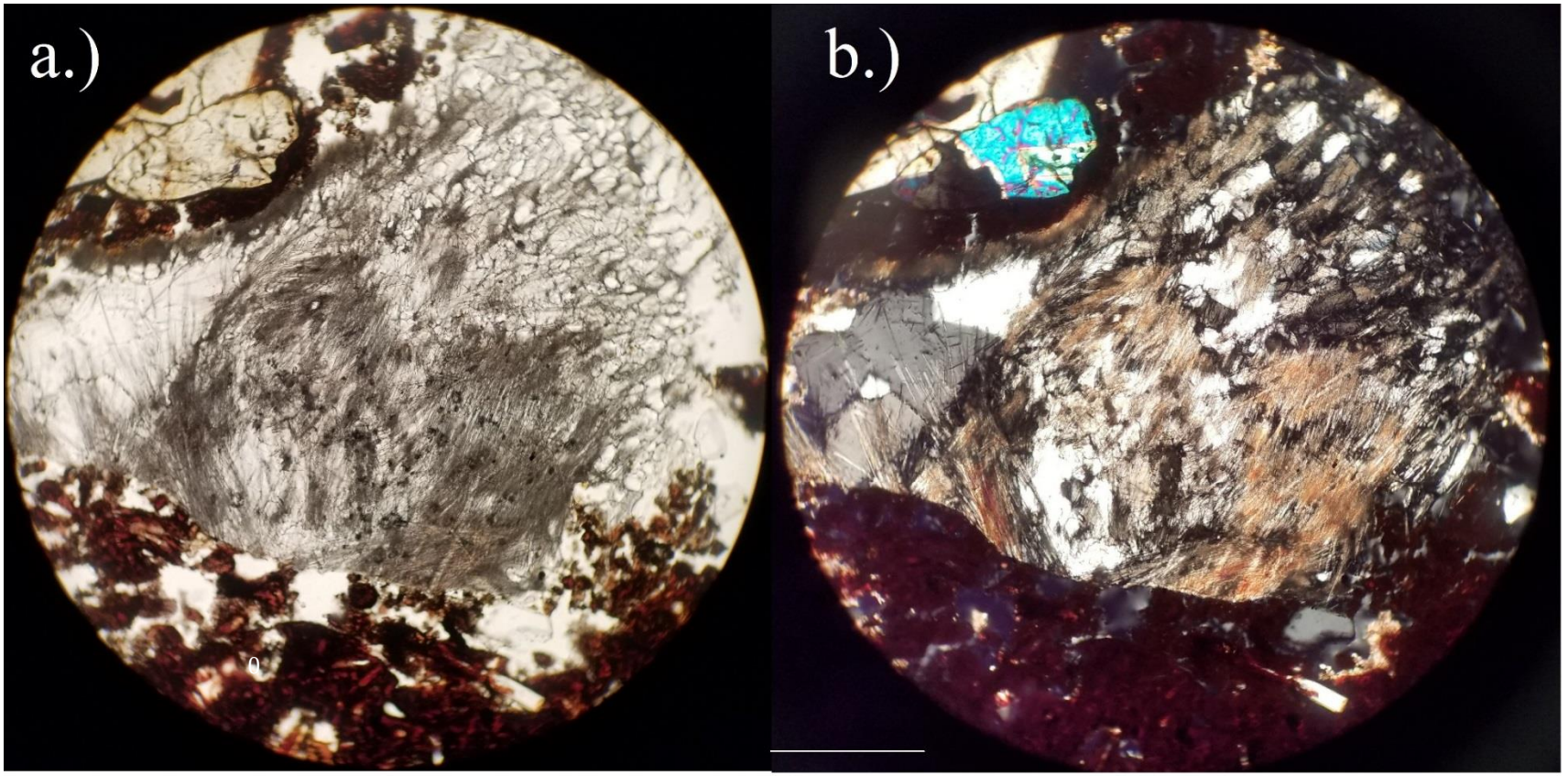

Figure 23- a.) PPL image of sillimanite in a potassium feldspar at 10x magnification. b.) XPL image of sillimanite in a potassium feldspar at 10x magnification. This is likely a xenocryst from surrounding country rock.

$^{87}Sr/^{86}Sr$ Results

Sr isotopic compositions of 12 plagioclase grains and two bulk-rock samples (513-4b and 513-7) were measured using the Finnigan MAT 262 thermal ionization mass spectrometer at Auburn University. The $^{87}Sr/^{86}Sr$ data for the Ashi samples 513-4b and 513-7 and 12 single-grain plagioclases (6 grains from each sample) are reported in Table 2 and graphed in Figures 24 and 25. The differences between single-grain plagioclase $^{87}Sr/^{86}Sr$ (513-4b P1-P6 and 513-7 P1-P6) and their respective whole-rock $^{87}Sr/^{86}Sr$ are also given.

Most plagioclase grains have higher $^{87}Sr/^{86}Sr$ than their whole-rock values. If we consider potential magma heterogeneity in $^{87}Sr/^{86}Sr$ of 0.001 within a closed-system magma chamber, then the plagioclases differing from the whole rock by >0.001 in $^{87}Sr/^{86}Sr$ values reflect open-system processes (mantle-derived magma recharge or crustal contaminations). In this study, 7 plagioclase grains have $^{87}Sr/^{86}Sr$ values higher than their whole-rock values by more than 0.001, clearly indicating open-system process. Note that one plagioclase from sample 513-4b has very high $^{87}Sr/^{86}Sr$ of 0.7159, which is 0.0058 higher than whole-rock ratio. The $^{87}Sr/^{86}Sr$ ratios of the other 5 plagioclase grains and whole rock differ by no more than 0.001, which is a strong indicator that these 5 plagioclase grains were in equilibrium with the Ashi magma and represent bulk magma composition of respective samples.

Sample	$^{87}Sr/^{86}Sr$	Error (2σ)	Plg $^{87}Sr/^{86}Sr$ – WR $^{87}Sr/^{86}Sr$
513-4b P1	0.715863	0.000036	0.005767
513-4b P2	0.711810	0.000024	0.001714
513-4b P3	0.711115	0.000013	0.001019
513-4b P4	0.711245	0.000013	0.001150
513-4b P5	0.711077	0.000009	0.000981
513-4b P6	0.711104	0.000009	0.001008
513-4b WR	0.710096	0.000010	
513-7 P1	0.710563	0.000008	0.000351
513-7 P2	0.710205	0.000011	-0.000007
513-7 P3	0.712639	0.000056	0.002427
513-7 P4	0.710481	0.000012	0.000269
513-7 P5	0.711066	0.000058	0.000854
513-7 P6	0.713936	0.000131	0.003724
513-7 WR	0.710212	0.000009	

Table 2- $^{87}Sr/^{86}Sr$ values for plagioclase grains collected from samples 513-4b and 513-7 and $^{87}Sr/^{86}Sr$ values of whole rock for samples 513-7b and 513-4. PLG/P=plagioclase, WR=whole rock.

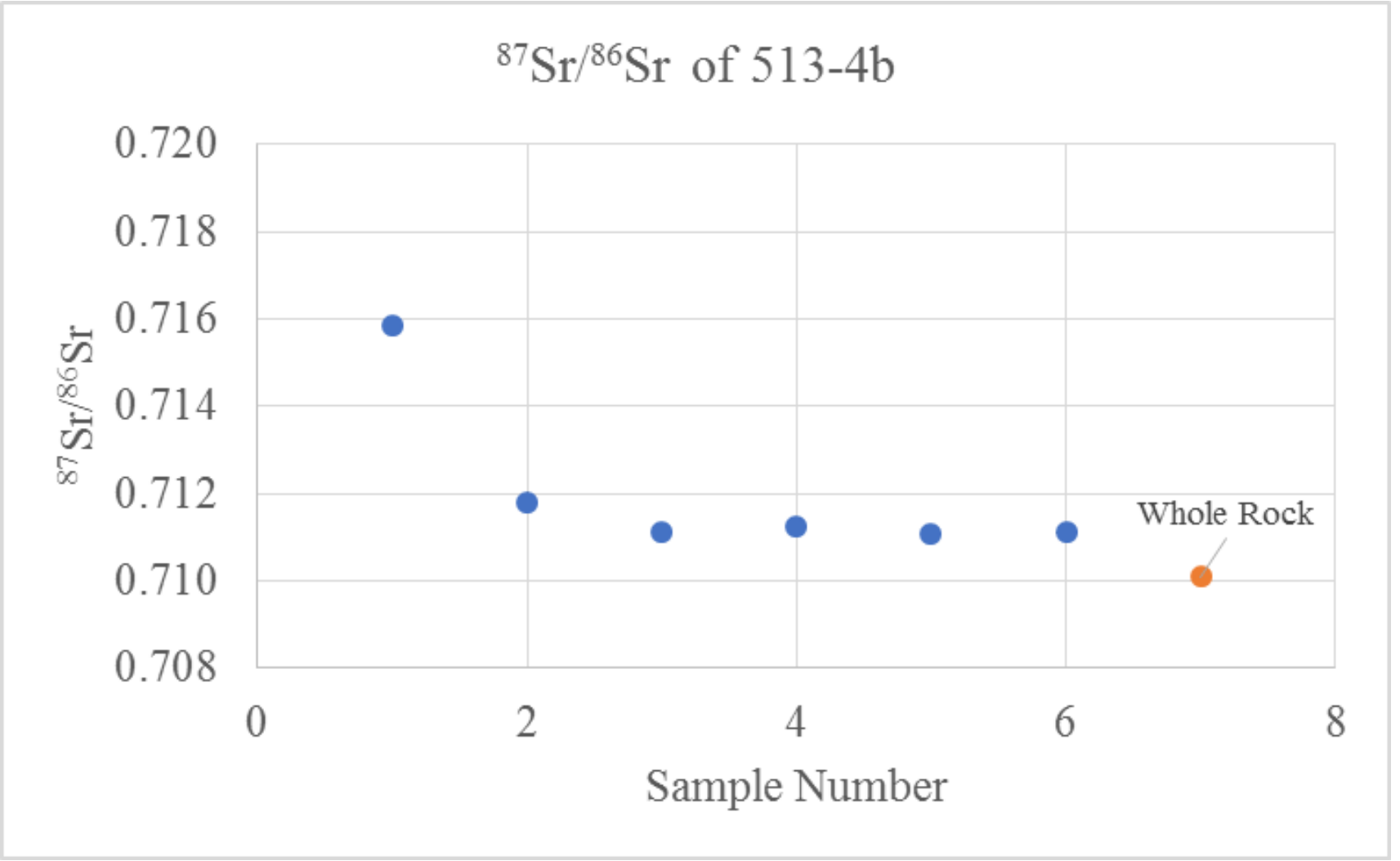

Figure 24- Graph of $^{87}Sr/^{86}Sr$ values for plagioclase grains collected from samples 513-4b compared to bulk rock value.

The difference in $^{87}Sr/^{86}Sr$ values for plagioclase grains compared to bulk rock is of importance (see text).

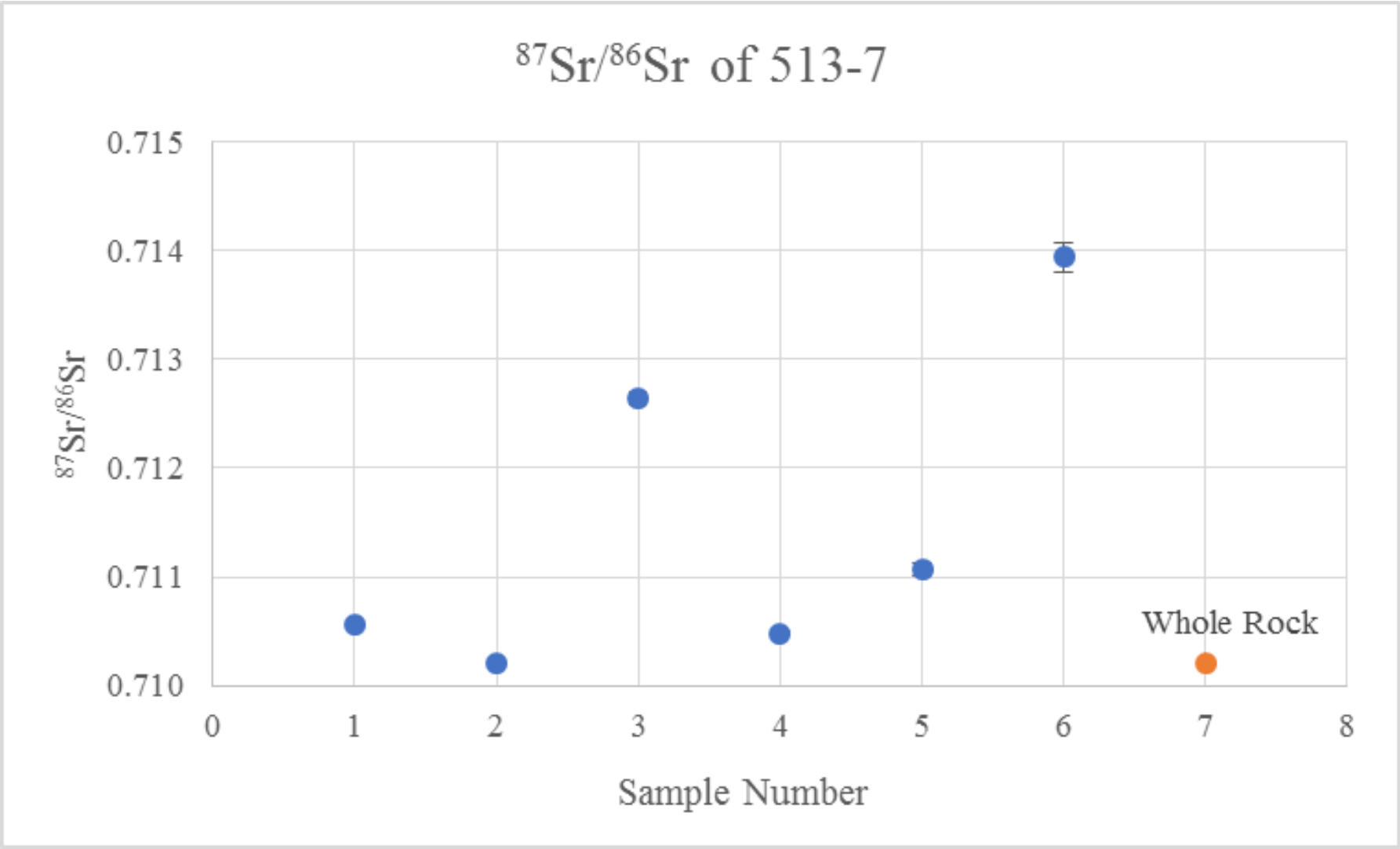

Figure 25- Graph of $^{87}Sr/^{86}Sr$ values for plagioclase grains collected from samples 513-7 compared to bulk rock value.

The difference in $^{87}Sr/^{86}Sr$ values for plagioclase grains compared to bulk rock is of importance (see text).

Electron Microprobe

EDS spectrum data collected from the Auburn University Electron Microprobe Analyzer (AU-EMPA) confirm that the primary mineral phases are plagioclase and pyroxene with minor amounts of ilmenite and rutile (spectral signatures can be found in Appendix 1). Selected plagioclase and pyroxenes were quantitatively analyzed using WDS spectrometers on the AU-EMPA. The AU-EMPA was standardized multiple times throughout the data collection process and rechecked several times during data collection. Appendix 2 shows the resulting oxide percent of several standards analyses as well as information pertinent to standardization. The values are in excellent agreement with each other.

In previous studies of the Ashi Volcano, reverse compositional zonation was reported in the plagioclase minerals, with An values ranging from 28.97 in the core, to 48.33 at the rim. Figure 26 shows the results of a plagioclase line traverse analysis done on sample 513-4b (traverse line 1). The An value in the core range between 27.22-31.24 and the An values at the rim are as high as 44.7, but are highly variable. Table 3 shows the oxide weight results from the plagioclase line traverse 1 presented in Figure 26. An values of a second line traverse analysis done on 513-4b is presented in Figure 27 (traverse line 2), with the corresponding oxide weight percent shown in Table 4. An values are remarkably consistent in the core, with values between 29.73-36.00. The rim shows higher An values on one side, but not on the other, with the higher An side showing values between 28.38-41.26. Figure 28 shows 2 point analyses and a line

traverse analyses (traverse line 3) from a plagioclase in sample 513-7 and the corresponding oxide weight percent in table 5. The data from traverse line 3 show the effects of reaction rim on the data. The analyses from the rim and core show the lower An value in the core of 23.51 with the An value of the rim equaling 38.14. These data from sample 513-4b and 513-7 show similar reverse compositional zonation that was previously reported by Yu et al. (2014).

In addition to reverse compositional zoning in plagioclase minerals, pyroxenes were also analyzed for compositional zonation. Reverse compositional zonation for pyroxenes has also been reported in previous studies (Yu et al., 2014). Figure 29 summarizes analyses done on both clinopyroxene and orthopyroxene. The trend of higher Mg # ($Mg\# = 100*(Mg/Mg+Fe^{2+})$) at the core and lower at the rim represents a typical trend of pyroxenes incorporating Mg into their structure early on in mineral formation with the amount decreasing as the magma cools. Thus, reverse compositional zonation of pyroxenes are not observed in the pyroxenes analyzed. Figure 29 b-e shows false color images of the composition of the pyroxenes. This false color is useful to emphasize the compositional concentrations and relative differences between composition internally in the sample.

Figures 30 and 31 plot the composition of plagioclase and pyroxenes on plagioclase and pyroxene classifications respectively. The compositions are averages of analyses done on the core of the respective mineral phases. Plagioclase analyzed in traverse lines 1-3 were used in creating the plagioclase classification plot (Figure 30). Pyroxenes shown in Figure 29 were used to plot the pyroxene compositions.

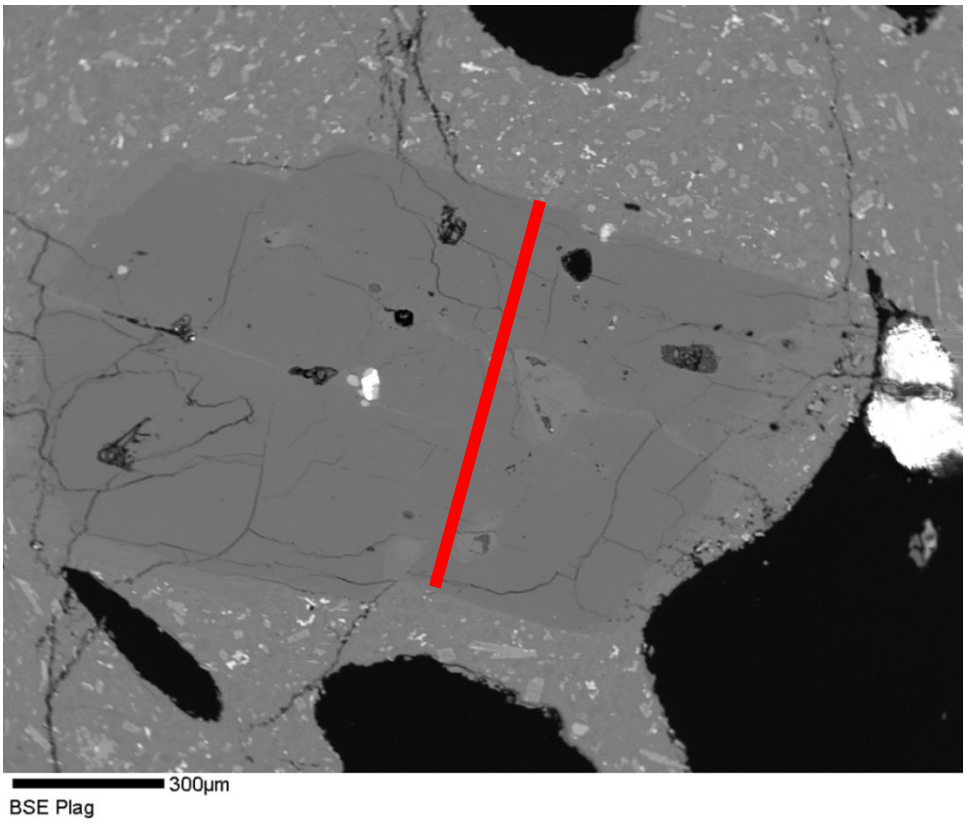

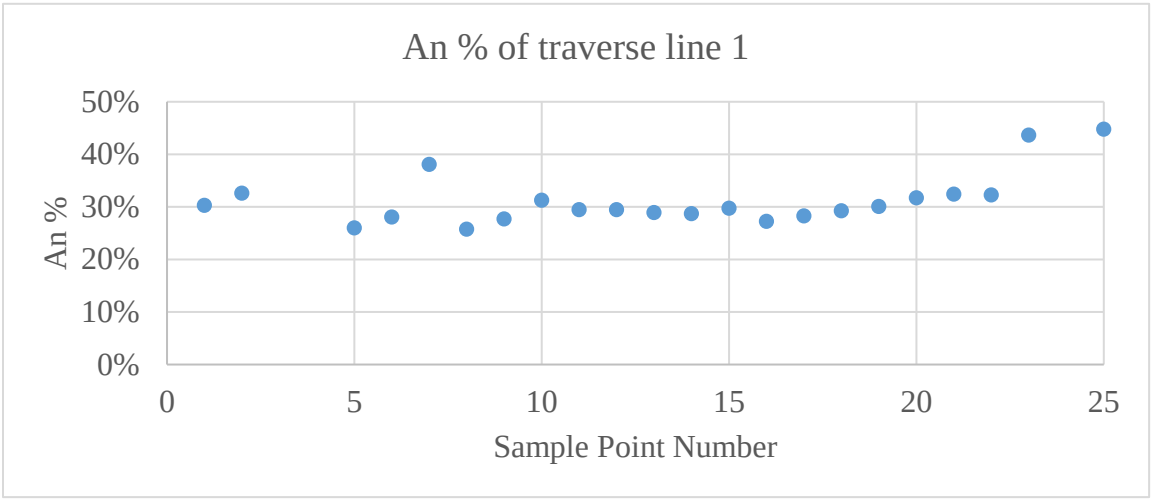

Figure 26- BSE of plagioclase grain in sample 513-4b. The red line in the top image shows the path of the traverse line. The graph shows the An%, with sample point number 1 starting at the top right of image A and increasing as the line moves to the bottom left. The red line shows the path of the line traverse.

Analysis Number	1	2	3	4	5	6	7	8	9	10	11	12	13	14	15
SiO_2	63.54	61.97	68.99	67.34	64.45	62.71	60.59	63.81	63.62	62.34	63.08	62.74	63.36	62.94	62.87
TiO_2*	0	0	0	0	0	0	0	0	0	0	0	0	0	0	0
Al_2O_3	24.03	24.64	14.64	16.33	19.69	20.71	24.24	22.83	23.15	24.37	24.39	24.42	24.38	24.39	24.65
FeO	0	0	0.0045	0	0.0022	0.0022	0	0.0022	0.0022	0	0.0022	0.0045	0.0022	0.0023	0.0023
MnO	0.0024	0.0024	0.0024	0.0024	0.0024	0.0024	0.0024	0.0073	0.0024	0.0048	0.0024	0.0024	0.0024	0.0024	0.0024
MgO	0.00	0.11	0.58	0.45	0.30	0.30	0.14	0.04	0.05	0.25	0.00	0.00	0.06	0.00	0.00
CaO	6.33	6.91	2.03	2.97	4.67	5.20	7.70	5.21	5.70	6.49	6.09	6.14	6.12	6.09	6.30
NaO	6.85	6.63	3.30	3.49	4.04	4.35	5.51	5.95	6.27	6.54	6.80	7.08	7.39	7.65	7.55
K_2O	1.84	1.93	6.26	5.85	5.04	4.59	2.15	3.59	2.98	2.06	1.91	1.60	1.41	1.08	1.03
Total	102.59	102.19	95.80	96.43	98.19	97.87	100.34	101.44	101.78	102.05	102.28	101.98	102.72	102.16	102.40
Numbers of ions on the basis of 8 O															
SiO_2	2.989	2.031	2.980	2.760	2.713	3.170	3.087	2.925	2.863	2.705	2.810	2.791	2.729	2.748	2.741
Al_2O_3	1.003	1.961	1.019	1.230	1.272	0.793	0.882	1.053	1.115	1.275	1.185	1.197	1.257	1.252	1.257
FeO	0.002	0.024	0.001	0.000	0.000	0.000	0.000	0.000	0.000	0.000	0.000	0.000	0.000	0.000	0.000
MnO	0.003	0.000	0.000	0.000	0.007	0.039	0.031	0.020	0.021	0.010	0.003	0.003	0.016	0.000	0.000
MgO	0.002	0.001	0.000	0.000	0.000	0.000	0.000	0.000	0.000	0.000	0.000	0.000	0.000	0.000	0.000
CaO	0.001	0.944	0.018	0.295	0.324	0.100	0.146	0.227	0.254	0.368	0.246	0.268	0.304	0.284	0.287
NaO	0.118	0.047	0.973	0.577	0.563	0.294	0.310	0.356	0.385	0.477	0.508	0.534	0.555	0.575	0.600
K_2O	0.899	0.002	0.013	0.102	0.108	0.367	0.342	0.292	0.267	0.122	0.202	0.167	0.115	0.106	0.089
Z	3.99	3.98	3.96	3.97	3.98	3.98	3.98	3.99	3.99	3.99	4.00	4.00	3.99	3.99	4.00
X	0.97	0.99	0.76	0.80	0.87	0.91	0.97	0.96	0.97	0.97	0.97	0.98	0.98	0.99	0.99
Mole Percent															
Ab	30.26%	32.58%	13.12%	18.25%	25.97%	28.05%	38.06%	25.72%	27.67%	31.24%	29.46%	29.44%	28.90%	28.69%	29.73%
An	59.28%	56.59%	38.65%	38.88%	40.66%	42.47%	49.29%	53.17%	55.09%	56.98%	59.54%	61.45%	63.18%	65.23%	64.49%
Or	10.45%	10.83%	48.23%	42.87%	33.37%	29.48%	12.65%	21.11%	17.24%	11.78%	11.00%	9.11%	7.92%	6.08%	5.78%

Table 3- Oxide weight percent from first plagioclase line traverse 1 analysis of sample 513-4b. *TiO_2 not analyzed.

Analysis Number	16	17	18	19	20	21	22	23	24	25	26	27	28	29
SiO_2	63.58	63.74	62.29	62.31	62.76	62.3	62.28	59.33	69.45	59.6	68.83	61.61	69.49	68.59
TiO_2*	0	0	0	0	0	0	0	0	0	0	0	0	0	0
Al_2O_3	23.91	23.98	23.66	24.42	24.78	24.71	24.68	16.77	15.22	13.69	14.49	11.08	13.78	14.54
FeO	0.0023	0.0023	0.0023	0.0023	0.0023	0.0023	0	0.0023	0	0.0068	0.0023	0.0047	0.0024	0.0024
MnO	0.0049	0.0024	0.0024	0.0024	0.0024	0.0049	0.0024	0.0025	0.0025	0.0025	0.0025	0.0051	0.0051	0.0026
MgO	0.09	0.00	0.82	0.79	0.00	0.00	0.00	3.98	0.40	0.34	0.50	7.03	1.39	0.35
CaO	5.79	5.95	6.01	6.36	6.70	6.68	6.71	7.67	2.53	10.02	1.94	4.25	1.76	2.11
NaO	7.84	7.58	7.39	7.49	7.23	6.74	6.61	4.03	3.57	3.02	3.01	2.23	3.27	3.12
K_2O	1.08	1.16	0.98	1.05	1.13	1.46	1.80	2.19	5.94	5.79	7.06	3.29	5.94	6.94
Total	102.30	102.41	101.16	102.42	102.61	101.90	102.08	93.98	97.11	92.47	95.83	89.50	95.64	95.65
Numbers of ions on the basis of 8 O														
Si	2.747	2.742	2.733	2.763	2.766	2.740	2.713	2.725	2.725	2.723	2.829	3.150	2.956	3.173
Al	1.246	1.252	1.263	1.225	1.227	1.227	1.253	1.268	1.274	1.272	0.943	0.814	0.800	0.787
Fe	0.000	0.000	0.000	0.000	0.000	0.000	0.000	0.000	0.000	0.000	0.000	0.000	0.000	0.000
Mn	0.004	0.000	0.000	0.006	0.000	0.054	0.051	0.000	0.000	0.000	0.283	0.027	0.025	0.034
Mg	0.000	0.000	0.000	0.000	0.000	0.000	0.000	0.000	0.000	0.000	0.000	0.000	0.000	0.000
Ca	0.284	0.284	0.293	0.270	0.277	0.283	0.297	0.312	0.313	0.314	0.392	0.123	0.533	0.096
Na	0.621	0.646	0.637	0.661	0.638	0.630	0.633	0.609	0.572	0.561	0.373	0.314	0.291	0.269
K	0.078	0.060	0.057	0.060	0.064	0.055	0.058	0.063	0.082	0.100	0.133	0.344	0.366	0.415
Z	3.99	3.99	3.97	3.97	3.99	4.00	4.00	3.77	3.96	3.76	3.96	3.68	3.94	3.96
X	0.99	0.98	0.97	0.99	0.98	0.97	0.98	0.90	0.78	1.19	0.78	0.65	0.73	0.79
Mole Percent														
Ab	27.22%	28.27%	29.24%	30.05%	31.70%	32.39%	32.24%	43.64%	15.75%	44.77%	12.26%	34.84%	11.92%	13.14%
An	66.73%	65.19%	65.09%	64.07%	61.91%	59.17%	57.49%	41.51%	40.22%	24.42%	34.50%	33.04%	40.12%	35.26%
Or	6.05%	6.54%	5.67%	5.88%	6.39%	8.44%	10.27%	14.85%	44.03%	30.81%	53.24%	32.12%	47.95%	51.60%

Table 3- Continued. Oxide weight percent from first plagioclase line traverse 1 analysis of sample 513-4b. *TiO_2 not analyzed.

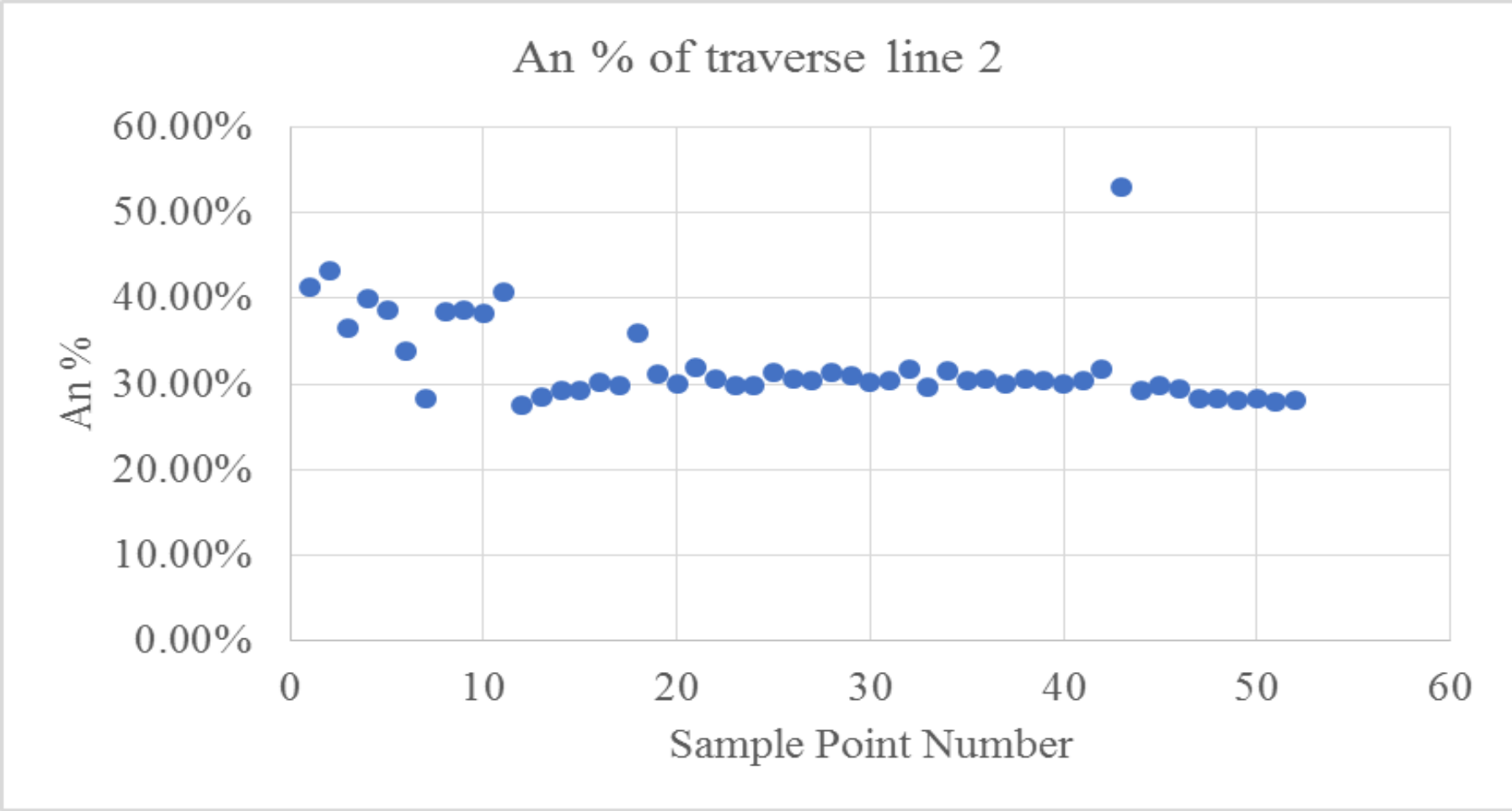

Figure 27- Graph of An values of a second line traverse analysis done plagioclase grain in sample 513-4b. An values are remarkably consistent in the core, with values between 29.73-36.00. The rim shows higher An values on one side, but not on the other, with the higher An side showing values between 28.38-41.26.

Analysis Number	1	2	3	4	5	6	7	8	9	10	11	12	13	14	15
SiO_2	0	0	16.28	71.96	58.76	72.36	72.76	67.19	59.97	57.8	60.89	59.01	59.91	61.35	63.91
TiO_2*	0	0	0	0	0	0	0	0	0	0	0	0	0	0	0
Al_2O_3	0.01	0	3.6	15.26	22.03	14.75	15.23	17.85	24.35	26.13	22.66	25.39	24.52	22.43	21.31
FeO	0.0021	0.0021	0	0.0021	0.0043	0.0021	0.0021	0.0021	0.0043	0.0021	0.0021	0.0021	0.0021	0.0021	0.0064
MnO	0.0022	0.0023	0.0023	0.0023	0.0023	0.0023	0.0046	0.0046	0	0.0023	0.0023	0.0046	0.0023	0.0023	0.0023
MgO	0	0	6.3	0.23	0.13	0.15	0.05	0.07	0.2	0.02	0.09	0.03	0.13	0.15	0.2
CaO	0	0.03	1.35	1.82	9.1	0.9	1.39	2.98	8.23	8.93	7.13	8.28	7.83	6.48	5.24
NaO	0.00	0.02	0.08	3.97	4.98	2.49	3.09	3.28	5.11	5.47	4.81	5.58	5.52	5.05	5.18
K_2O	0	0	0.08	5.74	2.2	6.45	5.95	6.57	2.07	1.49	3.08	1.92	2.03	2.99	3.23
Total	0.01	0.05	27.69	98.98	97.21	97.10	98.48	97.95	99.93	99.84	98.66	100.22	99.94	98.45	99.08
Numbers of ions on the basis of 8 O															
Si	2.80	2.78	2.71	2.78	2.81	2.75	2.78	2.79	2.80	2.79	2.79	2.80	2.78	2.81	2.79
Al	1.21	1.15	1.20	1.17	1.09	1.19	1.16	1.14	1.20	1.20	1.21	1.20	1.22	1.20	1.22
Fe	0.013	0.091	0.095	0.059	0.102	0.060	0.084	0.068	0.014	0.013	0.012	0.012	0.010	0.020	0.012
Mn	0.002	0.059	0.063	0.038	0.069	0.038	0.053	0.043	0.002	0.000	0.000	0.001	0.000	0.003	0.000
Mg	0.000	0.003	0.001	0.001	0.005	0.001	0.002	0.002	0.000	0.000	0.000	0.001	0.002	0.000	0.001
Ca	0.22	0.31	0.38	0.36	0.33	0.36	0.32	0.24	0.23	0.22	0.22	0.22	0.22	0.22	0.22
Na	0.58	0.40	0.42	0.39	0.37	0.42	0.40	0.53	0.61	0.65	0.63	0.60	0.63	0.59	0.60
K	0.12	0.11	0.07	0.06	0.09	0.09	0.10	0.15	0.10	0.11	0.12	0.12	0.12	0.12	0.11
Z	4.01	3.93	3.91	3.95	3.91	3.94	3.93	3.94	4.00	3.99	4.00	4.00	4.00	4.00	4.01
X	0.92	0.83	0.87	0.81	0.79	0.87	0.82	0.93	0.94	0.98	0.97	0.94	0.97	0.93	0.93
Mole Percent															
Ab	23.51%	38.14%	43.63%	44.48%	41.67%	41.60%	39.30%	26.45%	24.11%	22.84%	22.63%	23.82%	22.91%	23.37%	24.07%
An	63.33%	48.60%	48.36%	48.02%	46.60%	48.55%	48.19%	57.74%	65.42%	66.12%	64.98%	63.53%	64.91%	63.92%	64.39%
Or	13.16%	13.26%	8.02%	7.49%	11.73%	9.86%	12.52%	15.82%	10.47%	11.04%	12.39%	12.65%	12.19%	12.71%	11.55%

Table 4- Oxide weight percent from second plagioclase line traverse 2 analysis of sample 513-4b. The first 3 analyses were analyses of the matrix and were not included in any considerations of plagioclase compositions. *TiO_2 not analyzed.

Analysis Number	16	17	18	19	20	21	22	23	24	25	26	27	28	29
SiO_2	59.93	60.53	59.71	58.61	62.55	62.28	62.4	62.55	56.5	62.3	60.08	62.13	62.33	58.56
TiO_2*	0	0	0	0	0	0	0	0	0	0	0	0	0	0
Al_2O_3	24.59	24.45	24.39	25.58	23.8	23.83	24.11	23.98	22.08	24.34	24.05	24.49	24.29	22.92
FeO	0.0021	0	0.0021	0.0021	0.0021	0.0021	0.0021	0.0021	0.0042	0.0021	0	0	0.0042	0.0042
MnO	0.0023	0.0023	0	0.0046	0.0023	0.0023	0.0023	0.0046	0.0046	0.0023	0.0023	0.0023	0.0046	0.0023
MgO	0.46	0.13	0	0.08	0.02	0.01	0	0	0.66	0	0.01	0	0	0.01
CaO	7.46	7.75	7.61	8.32	5.69	5.93	6.01	6	5.48	6.29	8.04	6.52	6.23	6.02
NaO	5.51	5.43	5.44	5.59	6.18	6.24	6.09	6.27	5.46	6.59	6.62	6.79	6.80	6.04
K_2O	1.66	2.04	2.04	1.65	3.21	3.07	2.93	2.68	2.36	2.46	1.94	1.81	1.84	1.6
Total	99.61	100.33	99.19	99.84	101.45	101.36	101.54	101.49	92.55	101.98	100.74	101.74	101.50	95.16
Numbers of ions on the basis of 8 O														
Si	2.79	2.77	2.85	2.86	2.67	2.76	2.93	2.72	2.83	3.15	2.96	3.17	3.04	3.19
Al	1.21	1.15	1.00	1.02	1.28	1.16	0.84	1.27	0.94	0.81	0.80	0.79	0.64	0.75
Fe	0.018	0.085	0.131	0.110	0.058	0.099	0.230	0.000	0.000	0.000	0.000	0.000	0.000	0.000
Mn	0.002	0.064	0.141	0.090	0.029	0.052	0.145	0.000	0.283	0.027	0.025	0.034	0.517	0.095
Mg	0.000	0.002	0.001	0.001	0.000	0.000	0.004	0.000	0.000	0.000	0.000	0.000	0.000	0.000
Ca	0.24	0.33	0.25	0.27	0.43	0.34	0.20	0.31	0.39	0.12	0.53	0.10	0.22	0.09
Na	0.61	0.38	0.37	0.37	0.41	0.40	0.48	0.56	0.37	0.31	0.29	0.27	0.21	0.29
K	0.09	0.09	0.18	0.19	0.06	0.13	0.15	0.10	0.13	0.34	0.37	0.42	0.21	0.35
Z	4.00	3.93	3.85	3.88	3.95	3.91	3.76	4.00	3.77	3.96	3.76	3.96	3.68	3.94
X	0.94	0.81	0.80	0.83	0.89	0.87	0.82	0.98	0.90	0.78	1.19	0.78	0.65	0.73
Mole Percent														
Ab	25.56%	41.20%	31.31%	32.38%	47.67%	38.83%	24.22%	32.24%	43.64%	15.75%	44.77%	12.26%	34.84%	11.92%
An	65.35%	47.35%	45.67%	45.09%	45.89%	46.70%	57.91%	57.49%	41.51%	40.22%	24.42%	34.50%	33.04%	40.12%
Or	9.09%	11.45%	23.01%	22.53%	6.44%	14.48%	17.87%	10.27%	14.85%	44.03%	30.81%	53.24%	32.12%	47.95%

Table 4- Continued. Oxide weight percent from second plagioclase line traverse 2 analysis of sample 513-4b. *TiO_2 not analyzed.

Analysis Number	30	31	32	33	34	35	36	37	38	39	40	41	42	43	44	45
SiO_2	62.34	62.03	62.32	62.57	61.99	62.57	61.94	61.7	61.93	61.89	54.98	63.19	59.24	62.71	63.12	62.46
TiO_2*	0	0	0	0	0	0	0	0	0	0	0	0	0	0	0	0
Al_2O_3	24.36	24.54	24.3	24.56	24.59	24.29	24	24.81	24.35	24.42	21.53	24.5	22.74	24.23	24.14	24.01
FeO	0.0021	0	0	0.0021	0.0063	0.0021	0.0021	0	0.0021	0	0.0021	0.0021	0.0021	0	0.0042	0.0021
MnO	0.0023	0.0023	0.0023	0.0023	0.0023	0.0046	0.0046	0.0023	0.0023	0.0023	0.0023	0.0023	0.0046	0.0023	0.0068	0.0023
MgO	0	0	0	0	0	0	0	0.01	0.03	0	0.15	0	0	0	0	0
CaO	6.36	6.15	6.27	6.44	6.28	6.33	6.41	6.49	6.24	6.39	5.7	6.35	6.13	6.21	6.26	6.31
NaO	6.87	6.88	7.04	6.79	6.77	6.89	6.75	6.97	6.91	6.97	5.87	7.24	6.29	6.65	6.60	6.72
K_2O	1.66	1.74	1.71	1.53	1.7	1.71	1.51	1.5	1.59	1.68	1.41	1.7	1.59	1.78	1.89	2.1
Total	101.59	101.34	101.64	101.89	101.34	101.80	100.62	101.48	101.05	101.35	89.64	102.98	96.00	101.58	102.02	101.60
Numbers of ions on the basis of 8 O																
Si	2.74	2.73	2.74	2.73	2.73	2.74	2.74	2.71	2.73	2.73	2.73	2.74	2.75	2.75	2.76	2.75
Al	1.26	1.27	1.26	1.27	1.28	1.25	1.25	1.29	1.27	1.27	1.26	1.25	1.24	1.25	1.24	1.24
Fe	0.000	0.000	0.000	0.000	0.000	0.000	0.000	0.000	0.000	0.000	0.000	0.000	0.000	0.000	0.000	0.000
Mn	0.000	0.000	0.000	0.000	0.000	0.000	0.000	0.000	0.000	0.000	0.000	0.000	0.000	0.000	0.000	0.000
Mg	0.000	0.000	0.000	0.000	0.000	0.000	0.000	0.000	0.001	0.000	0.006	0.000	0.000	0.000	0.000	0.000
Ca	0.30	0.29	0.29	0.30	0.30	0.30	0.30	0.31	0.29	0.30	0.30	0.29	0.30	0.29	0.29	0.30
Na	0.58	0.59	0.60	0.58	0.58	0.59	0.58	0.59	0.59	0.60	0.57	0.61	0.57	0.57	0.56	0.57
K	0.09	0.10	0.10	0.09	0.10	0.10	0.09	0.08	0.09	0.09	0.09	0.09	0.09	0.10	0.11	0.12
Z	4.00	4.00	3.99	4.00	4.00	3.99	3.99	4.00	4.00	3.99	4.00	3.99	3.99	4.00	4.00	3.99
X	0.98	0.97	0.99	0.96	0.97	0.98	0.97	0.98	0.98	0.99	0.96	1.00	0.97	0.96	0.96	0.99
Mole Percent																
Ab	30.62%	29.74%	29.79%	31.33%	30.55%	30.38%	31.38%	31.06%	30.23%	30.42%	31.66%	29.56%	31.58%	30.49%	30.60%	30.08%
An	59.87%	60.23%	60.54%	59.80%	59.61%	59.85%	59.82%	60.39%	60.60%	60.06%	59.02%	61.01%	58.66%	59.10%	58.40%	57.99%
Or	9.52%	10.02%	9.67%	8.87%	9.85%	9.77%	8.80%	8.55%	9.17%	9.52%	9.33%	9.43%	9.76%	10.41%	11.00%	11.92%

Table 4- Continued. Oxide weight percent from second plagioclase line traverse 2 analysis of sample 513-4b. *TiO_2 not analyzed.

Analysis Number	46	47	48	49	50	51	52	53	54	55	56	57	58	59	60
SiO_2	62.47	60.1	63.04	63.14	62.38	53.52	63.22	62.56	62.83	63.52	63.16	63.67	64.33	63.55	62.62
TiO_2*	0	0	0	0	0	0	0	0	0	0	0	0	0	0	0
Al_2O_3	24.15	23.04	23.98	24.1	24.51	20.68	24.32	23.96	24.27	23.85	23.81	23.85	23.74	23.65	23.19
FeO	0.0042	0.0021	0.0021	0	0.0021	0.0021	0.0021	0.0021	0.0021	0.0021	0.0042	0.0021	0.0042	0.0021	0.0021
MnO	0.0023	0.0023	0.0023	0.0023	0.0023	0.0023	0.0023	0.0023	0.0023	0.0023	0.0023	0.0023	0.0023	0.0023	0.0023
MgO	0.03	1.63	0.02	0	0.06	0.14	0	0.01	0.03	0	0.02	0	0	0.04	0
CaO	6.4	5.81	6.15	6.4	6.59	14.31	6.14	6.12	6.19	5.93	5.81	5.79	5.87	5.72	5.71
NaO	6.66	6.00	6.51	6.46	6.14	5.53	6.47	6.38	6.67	6.72	6.66	6.78	6.78	6.68	6.68
K_2O	2.03	2.01	2.15	2.48	2.59	2.26	2.64	2.38	2.38	2.39	2.26	2.15	2.19	2.26	2.32
Total	101.75	98.59	101.85	102.58	102.27	96.44	102.79	101.41	102.37	102.41	101.73	102.24	102.92	101.90	100.52
Numbers of ions on the basis of 8 O															
Si	2.74	2.74	2.76	2.75	2.73	2.58	2.75	2.75	2.74	2.77	2.77	2.77	2.78	2.78	2.78
Al	1.25	1.24	1.24	1.24	1.26	1.18	1.25	1.24	1.25	1.22	1.23	1.22	1.21	1.22	1.21
Fe	0.000	0.000	0.000	0.000	0.000	0.000	0.000	0.000	0.000	0.000	0.000	0.000	0.000	0.000	0.000
Mn	0.000	0.000	0.000	0.000	0.000	0.000	0.000	0.000	0.000	0.000	0.000	0.000	0.000	0.000	0.000
Mg	0.001	0.063	0.001	0.000	0.002	0.006	0.000	0.000	0.001	0.000	0.001	0.000	0.000	0.001	0.000
Ca	0.30	0.28	0.29	0.30	0.31	0.74	0.29	0.29	0.29	0.28	0.27	0.27	0.27	0.27	0.27
Na	0.57	0.53	0.55	0.55	0.52	0.52	0.55	0.54	0.56	0.57	0.57	0.57	0.57	0.57	0.57
K	0.11	0.12	0.12	0.14	0.14	0.14	0.15	0.13	0.13	0.13	0.13	0.12	0.12	0.13	0.13
Z	3.99	3.97	4.00	3.99	3.99	3.76	4.00	4.00	3.99	3.99	4.00	4.00	3.99	4.00	3.99
X	0.98	0.93	0.96	0.98	0.97	1.40	0.98	0.97	0.99	0.98	0.97	0.96	0.96	0.96	0.98
Mole Percent															
Ab	30.66%	30.47%	30.01%	30.41%	31.70%	52.98%	29.24%	29.85%	29.34%	28.32%	28.26%	28.07%	28.29%	27.90%	27.77%
An	57.76%	56.97%	57.50%	55.56%	53.46%	37.06%	55.78%	56.33%	57.23%	58.09%	58.65%	59.51%	59.14%	58.98%	58.80%
Or	11.58%	12.56%	12.49%	14.03%	14.84%	9.96%	14.97%	13.82%	13.43%	13.59%	13.09%	12.42%	12.57%	13.13%	13.43%

Table 4- Continued. Oxide weight percent from second plagioclase line traverse 2 analysis of sample 513-4b. *TiO_2 not analyzed.

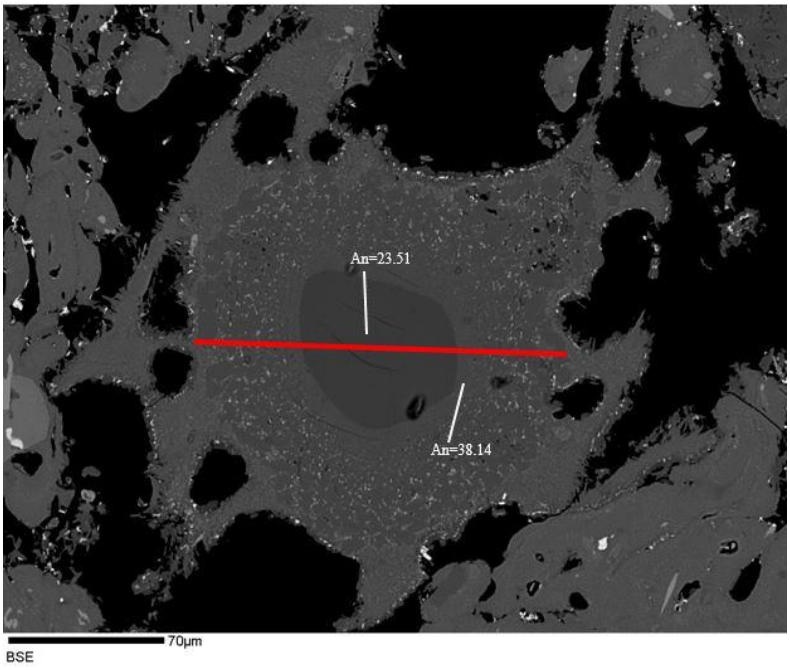

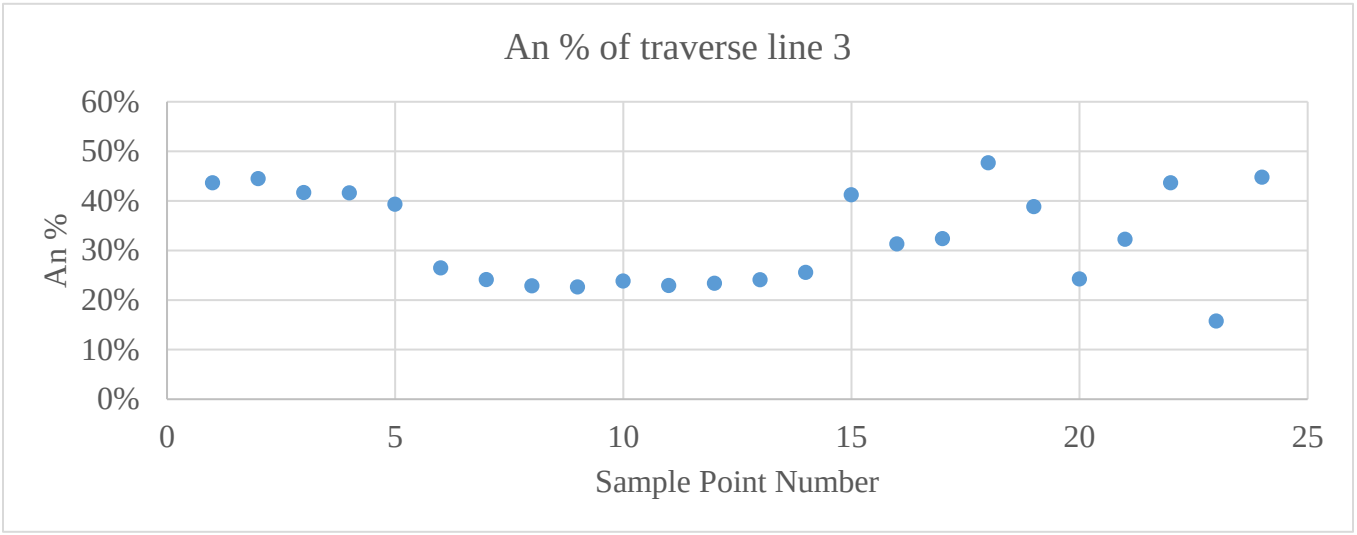

Figure 28- BSE of plagioclase grain in sample 513-7. The red line in the top image shows the path of the traverse line. The graph shows the An%, with sample point number 1 starting at the far right of image A and increasing as the line moves to the left. The red line shows the path of the line traverse. This plagioclase has an intense reaction rim, so 2 point analyses were conducted on the core and rim to determine An values on minimally altered regions, as shown on the BSE image.

Analysis Number	Core	Rim	1	2	3	4	5	6	7	8	9	10	11	12	13	14	15	16	17	18	19	20
SiO_2	62.49	60.13	56.68	56.73	57.05	58.20	59.36	62.63	62.53	62.42	62.43	62.29	62.37	61.70	62.87	62.33	59.02	59.93	61.14	55.88	58.22	63.35
TiO_2*	0	0	0	0	0	0	0	0	0	0	0	0	0	0	0	0	0	0	0	0	0	0
Al_2O_3	23.30	22.31	23.31	24.68	22.24	23.72	22.20	21.00	23.10	23.17	23.07	22.89	23.27	22.90	23.29	23.05	22.46	19.01	18.81	25.32	22.35	15.11
FeO	0.36	2.48	2.61	1.75	2.92	1.69	2.28	1.78	0.38	0.36	0.33	0.34	0.26	0.54	0.33	0.49	2.33	3.50	2.85	1.62	2.69	5.85
MnO	0.00	0.07	0.03	0.03	0.13	0.02	0.05	0.06	0.00	0.00	0.00	0.03	0.05	0.00	0.03	0.00	0.05	0.04	0.03	0.00	0.00	0.11
MgO	0.03	0.90	0.96	0.64	1.10	0.59	0.81	0.63	0.03	0.01	0.00	0.01	0.00	0.05	0.00	0.04	0.99	2.11	1.32	0.45	0.80	2.07
CaO	4.59	6.72	8.1	8.35	7.38	7.91	6.82	4.95	4.81	4.74	4.59	4.69	4.67	4.56	4.73	5.04	7.15	5.25	5.46	9.29	7.15	3.96
NaO	6.83	4.73	4.96	4.98	4.56	5.1	4.62	5.97	7.21	7.58	7.28	6.91	7.31	6.89	6.99	7.12	4.54	4.23	4.2	4.94	4.75	5.23
K_2O	2.16	1.96	1.25	1.18	1.74	1.57	1.82	2.49	1.75	1.92	2.11	2.09	2.09	2.08	1.91	1.51	1.67	3.24	3.19	1.05	2.24	2.45
Total	99.76	99.31	97.90	98.34	97.13	98.81	97.96	99.49	99.82	100.20	99.81	99.25	100.01	98.72	100.15	99.57	98.20	97.31	97.00	98.56	98.20	98.13
Numbers of ions on the basis of 8 O																						
Si	2.79	2.73	2.63	2.61	2.67	2.66	2.74	2.83	2.79	2.78	2.79	2.79	2.78	2.78	2.79	2.78	2.72	2.82	2.86	2.57	2.70	2.96
Al_2	1.22	1.19	1.27	1.34	1.23	1.28	1.21	1.12	1.21	1.22	1.21	1.21	1.22	1.22	1.22	1.21	1.22	1.05	1.04	1.37	1.22	0.83
Fe	0.01	0.09	0.10	0.07	0.11	0.06	0.09	0.07	0.01	0.01	0.01	0.01	0.01	0.02	0.01	0.02	0.09	0.14	0.11	0.06	0.10	0.23
Mn	0.002	0.061	0.067	0.044	0.077	0.040	0.004	0.004	0.000	0.000	0.000	0.002	0.003	0.000	0.002	0	0.003	0.003	0.002	0.000	0.000	0.007
Mg	0.000	0.003	0.001	0.001	0.005	0.001	0.032	0.024	0.001	0.000	0.000	0.000	0.000	0.002	0.000	0.00138	0.039	0.084	0.052	0.018	0.031	0.082
Ca	0.22	0.33	0.40	0.41	0.37	0.39	0.34	0.24	0.23	0.23	0.22	0.23	0.22	0.22	0.22	0.24	0.35	0.26	0.27	0.46	0.36	0.20
Na	0.59	0.42	0.45	0.44	0.41	0.45	0.41	0.52	0.62	0.65	0.63	0.60	0.63	0.60	0.60	0.62	0.41	0.39	0.38	0.44	0.43	0.47
K_2	0.12	0.11	0.07	0.07	0.10	0.09	0.11	0.14	0.10	0.11	0.12	0.12	0.12	0.12	0.11	0.09	0.10	0.19	0.19	0.06	0.13	0.15
Z	4.01	3.92	3.90	3.94	3.89	3.94	3.94	3.95	4.00	3.99	4.00	4.00	4.00	4.00	4.01	3.99729	3.94	3.87	3.90	3.95	3.92	3.79
X	0.93	0.86	0.92	0.92	0.89	0.93	0.86	0.91	0.95	0.99	0.97	0.95	0.97	0.94	0.93	0.94383	0.86	0.85	0.85	0.96	0.91	0.82
Mole Percent																						
Ab	23.51%	38.14%	43.63%	44.48%	41.67%	41.60%	39.30%	26.45%	24.11%	22.84%	22.63%	23.82%	22.91%	23.37%	24.07%	25.56%	41.20%	31.31%	32.38%	47.67%	38.83%	24.22%
An	63.33%	48.60%	48.36%	48.02%	46.60%	48.55%	48.19%	57.74%	65.42%	66.12%	64.98%	63.53%	64.91%	63.92%	64.39%	65.35%	47.35%	45.67%	45.09%	45.89%	46.70%	57.91%
Or	13.16%	13.26%	8.02%	7.49%	11.73%	9.86%	12.52%	15.82%	10.47%	11.04%	12.39%	12.65%	12.19%	12.71%	11.55%	9.09%	11.45%	23.01%	22.53%	6.44%	14.48%	17.87%

Table 5- Oxide weight percent from second plagioclase line traverse 3 analysis of sample 513-7.

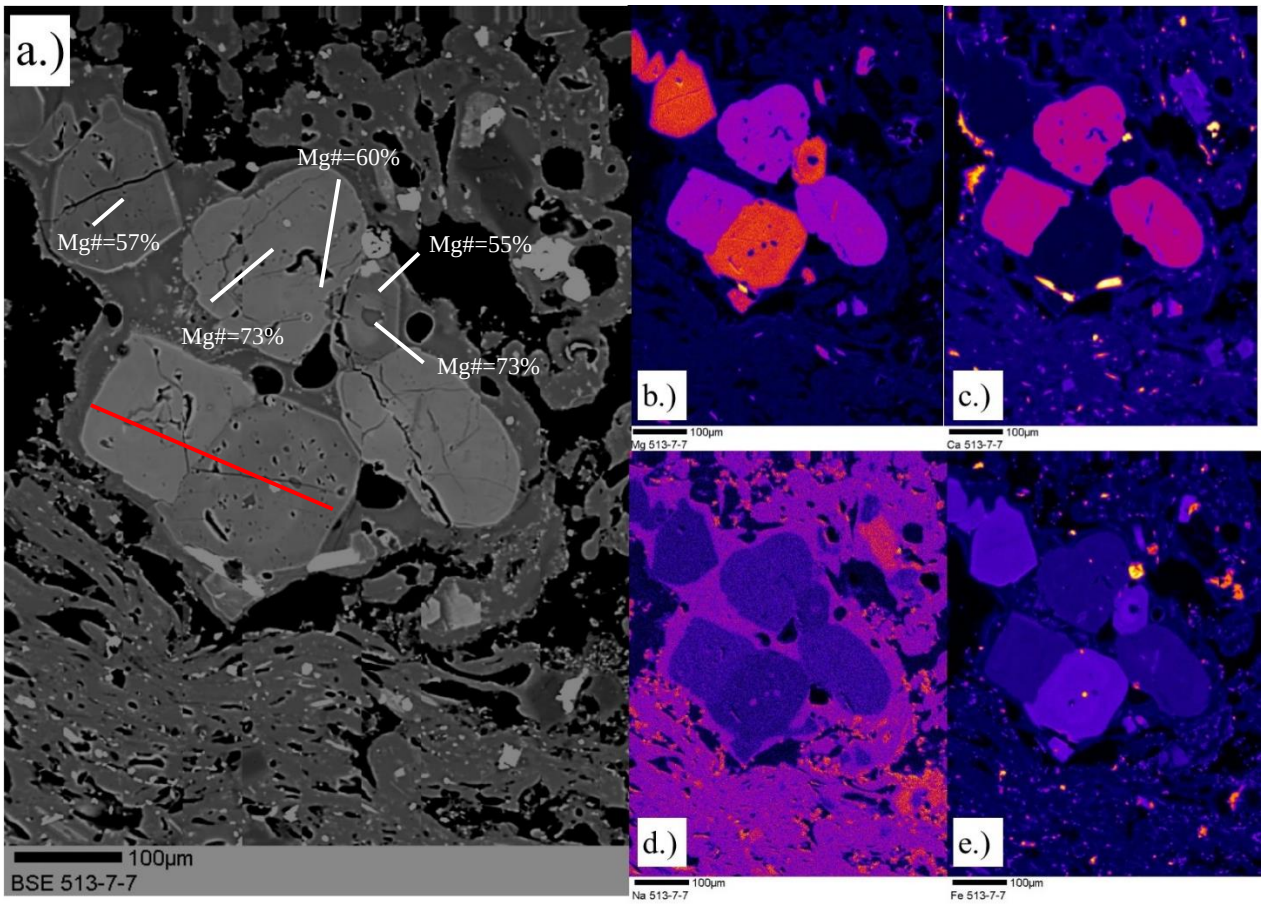

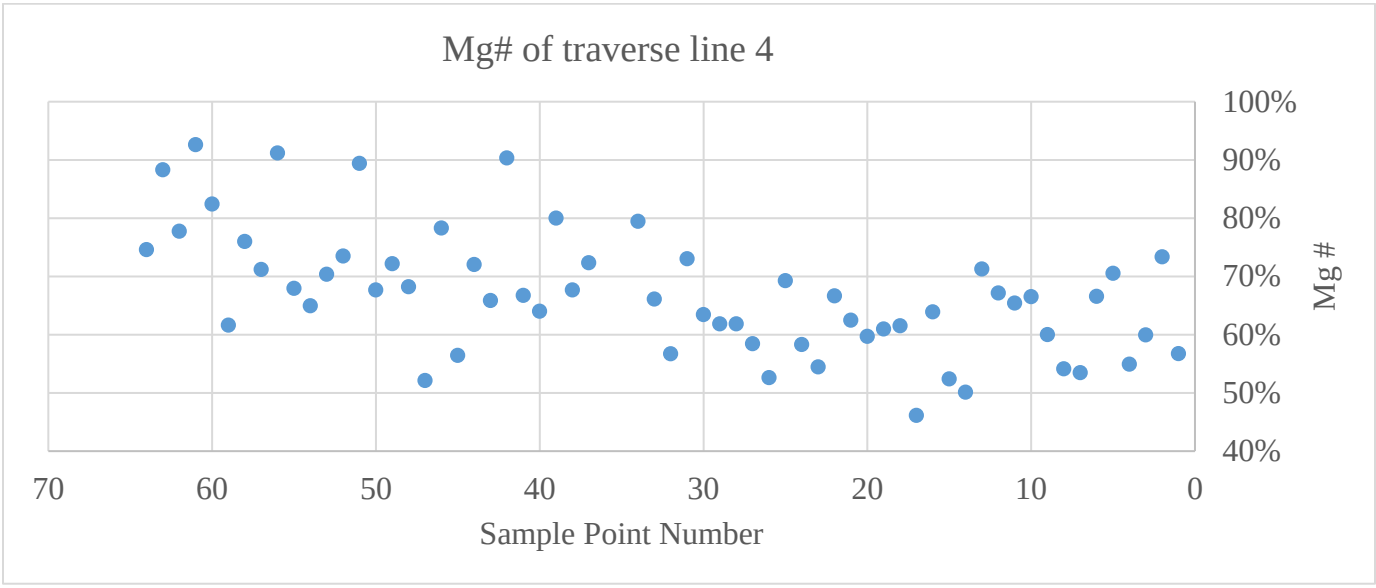

Figure 29- see page 62 for caption.

a.)BSE image of glomeroporphyritic pyroxene. The darker phases are orthopyroxene, while the lighter phases are clinopyroxene. The black phases represent glass and were analyzed for use in equilibrium temperature and pressure calculations. The red line is the path of traverse line 4, with the right side representing the line start and the left side representing the line end. The Mg# is used to determine compositional zonation b.) Compositional heat map of Mg concentration. c.) Compositional heat map of Ca concentration. Some of the small bright phases likely are small apatite crystals. d.) Compositional heat map of Na concentration. e.) Compositional heat map of Fe concentration. The small bright phases are likely ilmenite crystals.

	1	2	3	4	5	6	7	8	9	10	11	12	13	14	15
SiO_2	50.97	53.59	53.52	53.85	53.66	53.13	52.74	51.2	52.68	53.67	53.24	53.54	53.73	54.26	48.24
TiO_2	0.033	0.051	0.056	0.040	0.064	0.038	0.025	0.076	0.020	0.024	0.047	0.107	0.068	0.017	0.040
Al_2O_3	1.93	2.61	2.30	2.20	2.23	2.57	3.00	3.34	3.15	2.80	2.88	2.32	2.12	1.90	1.67
FeO	13.91	14.00	13.97	14.22	14.71	14.71	14.47	13.94	14.49	14.63	14.75	14.11	14.40	14.44	13.73
MgO	23.81	28.98	28.85	29.05	28.32	28.18	28.24	24.01	28.04	28.05	28.02	28.49	28.51	28.76	27.40
MnO	0.28	0.27	0.28	0.31	0.33	0.33	0.34	0.30	0.25	0.26	0.32	0.23	0.31	0.31	0.29
CaO	1.82	1.81	1.62	1.65	1.66	1.66	1.85	1.94	2.12	2.00	1.96	1.76	1.75	1.72	1.66
NaO	0.009	0.018	0.072	0.041	0.109	0.077	0.145	0.018	0.167	0.068	0.041	0.000	0.050	0.000	0.059
K_2O	0.009	0.002	0.014	0.000	0.005	0.000	0.000	0.055	0.145	0.011	0.000	0.009	0.011	0.003	0.069
Total	92.78	101.33	100.68	101.35	101.09	100.69	100.80	94.89	101.06	101.51	101.25	100.57	100.95	101.41	93.15
Numbers of ion on the basis of 6O															
Si	1.98	1.90	1.91	1.91	1.92	1.91	1.89	1.94	1.89	1.91	1.90	1.92	1.92	1.93	1.88
Ti	0.0010	0.0013	0.0015	0.0011	0.0017	0.0010	0.0007	0.0022	0.0005	0.0006	0.0013	0.0029	0.0018	0.0005	0.0012
iv AL	0.09	0.11	0.10	0.09	0.09	0.11	0.13	0.15	0.13	0.12	0.12	0.10	0.09	0.08	0.08
vi AL	0.45	0.42	0.42	0.42	0.44	0.44	0.43	0.44	0.43	0.43	0.44	0.42	0.43	0.43	0.45
Fe	1.38	1.53	1.54	1.54	1.51	1.51	1.51	1.36	1.50	1.49	1.49	1.52	1.52	1.52	1.59
Mg	0.08	0.07	0.06	0.06	0.06	0.06	0.07	0.08	0.08	0.08	0.08	0.07	0.07	0.07	0.07
Mn	0.009	0.008	0.008	0.009	0.010	0.010	0.010	0.010	0.008	0.008	0.010	0.007	0.009	0.009	0.010
Ca	0.00	0.00	0.00	0.00	0.01	0.01	0.01	0.00	0.01	0.00	0.00	0.00	0.00	0.00	0.00
Na	0.00	0.00	0.00	0.00	0.00	0.00	0.00	0.00	0.01	0.00	0.00	0.00	0.00	0.00	0.00
K	0.00	0.00	0.00	0.00	0.00	0.00	0.00	0.00	0.00	0.00	0.00	0.00	0.00	0.00	0.00
Atomic Percentages															
Mg	5.20%	4.30%	3.87%	3.91%	4.02%	4.05%	4.47%	5.49%	5.11%	4.85%	4.79%	4.26%	4.22%	4.12%	4.16%
Fe	94.75%	95.62%	95.82%	95.91%	95.51%	95.61%	94.90%	94.41%	94.16%	94.85%	95.03%	95.74%	95.56%	95.88%	95.57%
Ca	0.05%	0.08%	0.31%	0.17%	0.48%	0.34%	0.63%	0.09%	0.73%	0.30%	0.18%	0.00%	0.22%	0.00%	0.27%

Table 6- Oxide weight percent from pyroxene line traverse 3 analysis of sample 513-7, as shown in figure 29.

	16	17	18	19	20	21	22	23	24	25	26	27	28	29	30
SiO_2	54.87	54.46	54.5	54.29	54.67	54.1	53.57	53.23	53.22	52.42	52.55	50.8	53.21	49.56	52.46
TiO_2	0.000	0.000	0.025	0.000	0.002	0.015	0.054	0.000	0.071	0.016	0.041	0.000	0.049	0.116	0.000
Al_2O_3	1.54	1.48	1.61	1.41	1.46	1.31	1.26	2.22	2.91	2.91	2.82	1.68	2.71	4.55	0.00
FeO	14.19	14.25	14.33	14.18	14.24	14.16	14.18	14.64	14.46	15.15	15.19	14.61	14.27	9.10	0.00
MnO	29.10	29.01	29.13	28.97	28.84	29.14	28.66	28.54	27.89	26.95	27.64	26.28	28.24	15.55	0.14
MgO	0.32	0.34	0.28	0.30	0.35	0.27	0.30	0.31	0.31	0.30	0.36	0.26	0.33	0.22	0.01
CaO	1.73	1.78	1.72	1.74	1.78	1.72	1.89	1.89	1.79	2.03	1.75	1.85	1.81	17.94	47.36
NaO	0.000	0.194	0.032	0.095	0.018	0.005	0.099	0.077	0.072	0.050	0.082	0.027	0.059	0.583	0.000
K_2O	0.009	0.000	0.004	0.017	0.007	0.000	0.004	0.000	0.017	0.000	0.007	0.036	0.001	0.038	0.000
Total	101.77	101.52	101.63	101.00	101.37	100.72	100.02	100.90	100.73	99.83	100.44	95.55	100.68	97.66	99.97
Numbers of ion on the basis of 6O															
Si	1.94	1.93	1.93	1.93	1.94	1.93	1.93	1.91	1.91	1.90	1.90	1.93	1.91	1.88	2.02
Ti	0.0000	0.0000	0.0007	0.0000	0.0001	0.0004	0.0015	0.0000	0.0019	0.0004	0.0011	0.0000	0.0013	0.0033	0.0000
iv AL	0.06	0.06	0.07	0.06	0.06	0.06	0.05	0.09	0.12	0.12	0.12	0.08	0.11	0.20	0.00
vi AL	0.42	0.42	0.42	0.42	0.42	0.42	0.43	0.44	0.43	0.46	0.46	0.46	0.43	0.29	0.00
Fe	1.53	1.53	1.54	1.54	1.53	1.55	1.54	1.52	1.49	1.46	1.49	1.49	1.51	0.88	0.01
Mg	0.07	0.07	0.07	0.07	0.07	0.07	0.07	0.07	0.07	0.08	0.07	0.08	0.07	0.73	1.95
Mn	0.010	0.010	0.008	0.009	0.011	0.008	0.009	0.009	0.009	0.009	0.011	0.008	0.010	0.007	0.000
Ca	0.00	0.01	0.00	0.01	0.00	0.00	0.01	0.01	0.01	0.00	0.01	0.00	0.00	0.04	0.00
Na	0.00	0.00	0.00	0.00	0.00	0.00	0.00	0.00	0.00	0.00	0.00	0.00	0.00	0.00	0.00
K	0.00	0.00	0.00	0.00	0.00	0.00	0.00	0.00	0.00	0.00	0.00	0.00	0.00	0.00	0.00
Atomic Percentages															
Mg	4.10%	4.20%	4.07%	4.12%	4.24%	4.08%	4.50%	4.52%	4.39%	5.13%	4.34%	4.82%	4.39%	44.16%	99.58%
Fe	95.90%	94.98%	95.79%	95.48%	95.68%	95.90%	95.07%	95.15%	95.29%	94.64%	95.29%	95.06%	95.35%	53.25%	0.42%
Ca	0.00%	0.82%	0.14%	0.41%	0.08%	0.02%	0.43%	0.33%	0.32%	0.23%	0.37%	0.13%	0.26%	2.60%	0.00%

Table 6- (Continued) Oxide weight percent from pyroxene line traverse 3 analysis of sample 513-7, as shown in figure 29.

	31	32	33	34	35	36	37	38	39	40	41	42	43	44	45
SiO_2	55.13	51.64	51.35	51.23	51.28	51	50.3	47.49	47.45	50.79	53.75	52.83	52.33	50.2	47.09
TiO_2	0.000	0.095	0.073	0.070	0.067	0.056	0.068	0.060	0.053	0.031	0.065	0.042	0.026	0.066	0.067
Al_2O_3	0.61	3.19	3.04	2.95	3.13	3.23	3.09	2.85	2.75	2.69	3.37	2.76	2.85	2.72	2.46
FeO	0.78	8.82	9.06	8.72	8.79	8.77	8.44	7.53	8.61	8.31	8.44	8.81	8.83	8.85	8.69
MnO	18.81	18.22	18.09	18.25	17.49	17.37	17.19	15.01	13.69	19.15	17.48	18.75	18.33	17.67	17.90
MgO	0.05	0.23	0.22	0.26	0.20	0.21	0.28	0.18	0.17	0.19	0.24	0.17	0.22	0.23	0.21
CaO	24.23	17.32	17.06	17.01	17.51	18.00	17.34	15.83	17.84	17.47	18.30	17.39	16.93	16.59	15.72
NaO	0.423	0.632	0.528	0.563	0.596	0.533	0.464	0.508	0.302	0.533	0.485	0.471	0.416	0.344	0.377
K_2O	0.000	0.002	0.000	0.000	0.000	0.013	0.012	0.002	0.007	0.000	0.000	0.003	0.000	0.005	0.014
Total	100.03	100.15	99.42	99.05	99.06	99.18	97.18	89.45	90.88	99.17	102.13	101.23	99.93	96.67	92.53
Numbers of ion on the basis of 6O															
Si	1.99	1.90	1.91	1.91	1.91	1.90	1.91	1.95	1.94	1.89	1.93	1.92	1.92	1.91	1.88
Ti	0.0000	0.0026	0.0020	0.0020	0.0019	0.0016	0.0019	0.0019	0.0016	0.0009	0.0018	0.0011	0.0007	0.0019	0.0020
iv AL	0.03	0.14	0.13	0.13	0.14	0.14	0.14	0.14	0.13	0.12	0.14	0.12	0.12	0.12	0.12
vi AL	0.02	0.27	0.28	0.27	0.27	0.27	0.27	0.26	0.29	0.26	0.25	0.27	0.27	0.28	0.29
Fe	1.01	1.00	1.00	1.01	0.97	0.96	0.97	0.92	0.83	1.06	0.94	1.02	1.00	1.00	1.07
Mg	0.94	0.68	0.68	0.68	0.70	0.72	0.71	0.70	0.78	0.70	0.70	0.68	0.67	0.68	0.67
Mn	0.002	0.007	0.007	0.008	0.006	0.006	0.009	0.006	0.006	0.006	0.007	0.005	0.007	0.007	0.007
Ca	0.03	0.05	0.04	0.04	0.04	0.04	0.03	0.04	0.02	0.04	0.03	0.03	0.03	0.03	0.03
Na	0.00	0.00	0.00	0.00	0.00	0.00	0.00	0.00	0.00	0.00	0.00	0.00	0.00	0.00	0.00
K	0.00	0.00	0.00	0.00	0.00	0.00	0.00	0.00	0.00	0.00	0.00	0.00	0.00	0.00	0.00
Atomic Percentages															
Mg	47.36%	39.53%	39.51%	39.18%	40.80%	41.73%	41.19%	42.06%	47.66%	38.76%	42.07%	39.23%	39.20%	39.69%	38.06%
Fe	51.15%	57.86%	58.28%	58.48%	56.69%	56.03%	56.81%	55.49%	50.88%	59.10%	55.91%	58.85%	59.05%	58.82%	60.29%
Ca	1.50%	2.61%	2.21%	2.35%	2.51%	2.24%	2.00%	2.45%	1.46%	2.14%	2.02%	1.93%	1.75%	1.49%	1.65%

Table 6- (Continued) Oxide weight percent from pyroxene line traverse 3 analysis of sample 513-7, as shown in figure 29.

	46	47	48	49	50	51	52	53	54	55	56	57	58	59	60
SiO_2	50.23	50.82	49.8	49.92	48.07	48.57	50.5	49.71	49.9	49.5	49.69	49.87	50.53	50.25	50.64
TiO_2	0.060	0.098	0.066	0.070	0.066	0.115	0.079	0.083	0.059	0.091	0.090	0.083	0.045	0.115	0.018
Al_2O_3	3.30	3.38	4.53	4.44	4.01	4.93	3.76	4.24	4.39	4.48	4.71	4.47	4.14	3.93	6.01
FeO	8.83	8.97	9.24	9.02	8.25	9.05	8.24	8.82	9.09	8.95	9.36	8.87	8.61	8.60	8.59
MnO	17.17	18.25	17.19	17.01	16.07	16.25	17.59	17.12	17.07	17.21	16.85	17.09	16.80	16.92	14.61
MgO	0.27	0.24	0.21	0.20	0.19	0.26	0.22	0.23	0.19	0.25	0.28	0.24	0.26	0.22	0.24
CaO	16.56	16.90	17.11	17.19	16.71	16.40	18.15	17.06	17.02	16.98	16.57	17.21	17.65	17.90	16.92
NaO	0.464	0.463	0.547	0.583	0.624	0.538	0.426	0.582	0.482	0.546	0.506	0.579	0.518	0.477	0.583
K_2O	0.002	0.010	0.004	0.000	0.000	0.000	0.000	0.000	0.017	0.003	0.000	0.001	0.000	0.020	0.378
Total	96.89	99.13	98.70	98.43	93.99	96.12	98.97	97.85	98.21	98.01	98.05	98.41	98.56	98.44	97.99
Numbers of ion on the basis of 6O															
Si	1.91	1.89	1.87	1.87	1.89	1.87	1.88	1.88	1.88	1.87	1.87	1.87	1.89	1.89	1.90
Ti	0.0017	0.0027	0.0019	0.0020	0.0020	0.0033	0.0022	0.0023	0.0017	0.0026	0.0025	0.0023	0.0013	0.0032	0.0005
iv AL	0.15	0.15	0.20	0.20	0.19	0.22	0.17	0.19	0.19	0.20	0.21	0.20	0.18	0.17	0.27
vi AL	0.28	0.28	0.29	0.28	0.27	0.29	0.26	0.28	0.29	0.28	0.29	0.28	0.27	0.27	0.27
Fe	0.97	1.01	0.96	0.95	0.94	0.93	0.98	0.96	0.96	0.97	0.95	0.96	0.94	0.95	0.82
Mg	0.67	0.67	0.69	0.69	0.70	0.68	0.73	0.69	0.69	0.69	0.67	0.69	0.71	0.72	0.68
Mn	0.009	0.007	0.007	0.006	0.006	0.009	0.007	0.007	0.006	0.008	0.009	0.007	0.008	0.007	0.008
Ca	0.03	0.03	0.04	0.04	0.05	0.04	0.03	0.04	0.04	0.04	0.04	0.04	0.04	0.03	0.04
Na	0.00	0.00	0.00	0.00	0.00	0.00	0.00	0.00	0.00	0.00	0.00	0.00	0.00	0.00	0.02
K	0.00	0.00	0.00	0.00	0.00	0.00	0.00	0.00	0.00	0.00	0.00	0.00	0.00	0.00	0.00
Atomic Percentages															
Mg	40.11%	39.19%	40.72%	41.02%	41.57%	41.02%	41.83%	40.69%	40.87%	40.51%	40.49%	40.94%	42.06%	42.31%	44.18%
Fe	57.86%	58.87%	56.92%	56.47%	55.62%	56.54%	56.40%	56.80%	57.03%	57.13%	57.28%	56.56%	55.70%	55.64%	53.07%
Ca	2.03%	1.94%	2.36%	2.52%	2.81%	2.44%	1.78%	2.51%	2.10%	2.36%	2.24%	2.49%	2.24%	2.04%	2.75%

Table 6- (Continued) Oxide weight percent from pyroxene line traverse 3 analysis of sample 513-7, as shown in figure 29.

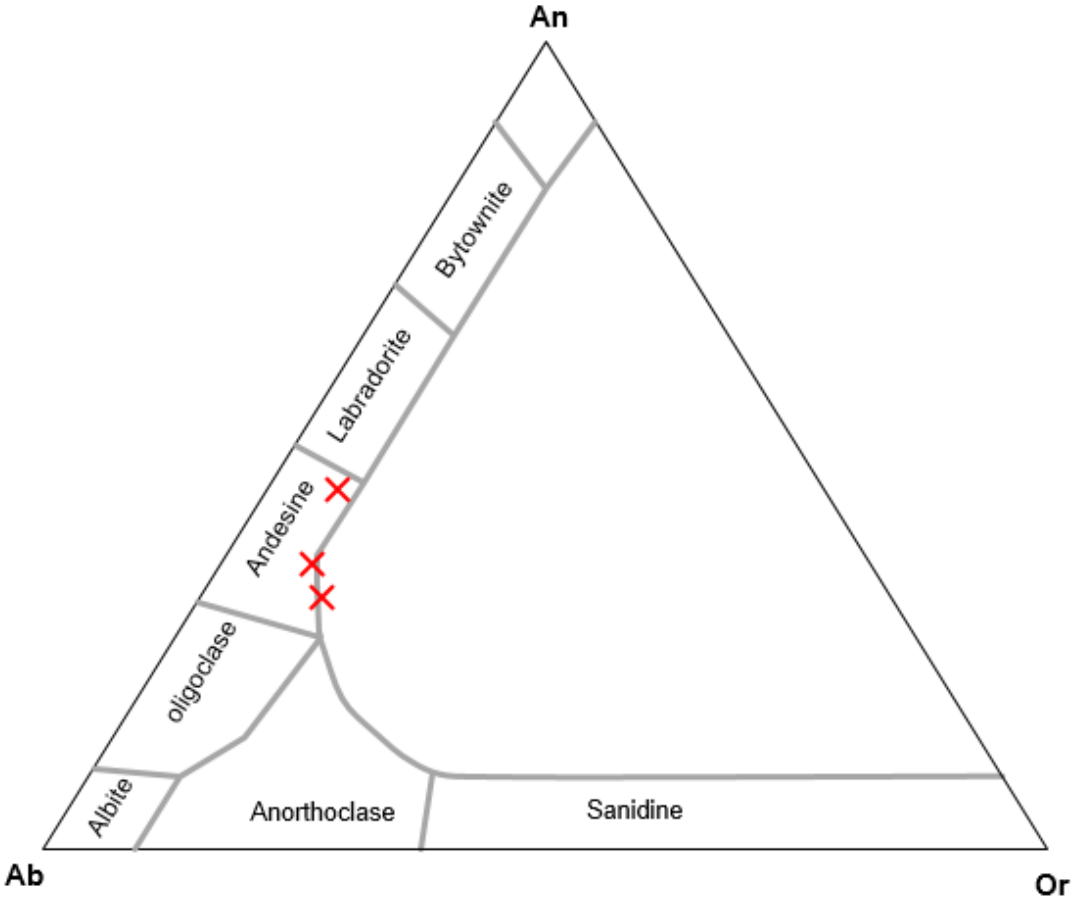

Figure 30- Plagioclase classification. Plagioclase compositions plotted are of analyses done on the core of plagioclase grains shown in figures 27-29.

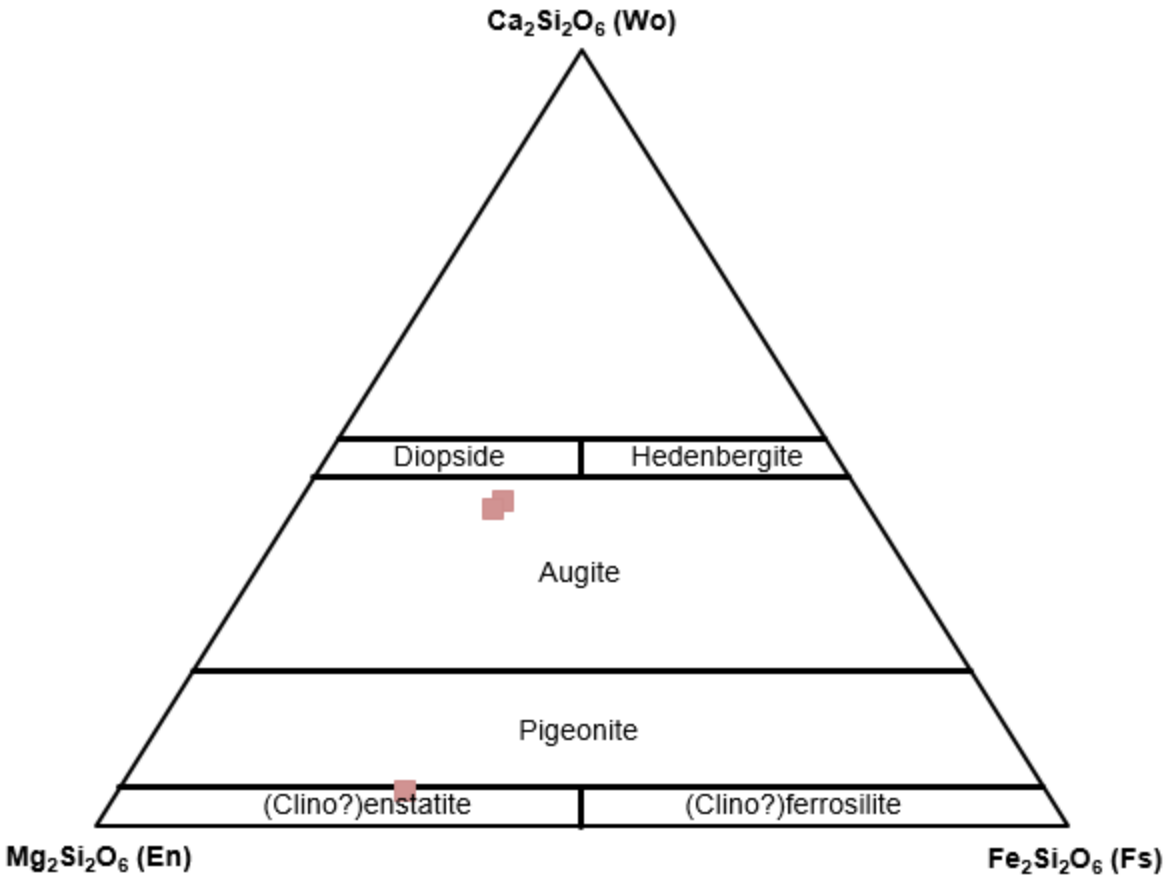

Figure 31- Pyroxene classification. Pyroxene compositions are core values from pyroxenes shown in figure 30. Modified from Marshall, (1996).

Pre-eruption Magma Temperature and Pressure

Using methods defined by Putirka (2008), equilibrium temperature and pressure were calculated using compositional analyses of orthopyroxenes and clinopyroxenes. In order to assess pre-eruption magma temperature and pressure, the equilibrium between pyroxene components must be evaluated. For orthopyroxene, the Fe-Mg exchange coefficient between cpx and opx K_D $(Fe\text{-}Mg)^{cpx\text{-}opx}$ is 1.09±0.14, the cpx and opx can be considered to be in equilibrium. This is calculated by equation 1 (Putirka, 2008):

$$K_D(Fe-Mg)^{cpx-opx} = \left(\frac{\frac{X_{Fe}^{cpx}}{X_{Mg}^{cpx}}}{\frac{X_{Fe}^{opx}}{X_{Mg}^{opx}}}\right)$$

Equation 1- Fe-Mg exchange coefficient equation used to test for equilibrium

Of the 5 orthopyroxene and clinopyroxene pairs analyzed, 3 were found to be in equilibrium and 2 were not. Using compositional data and the following equations by Putrika (2008), pressure and temperature were estimated.

$$\frac{10^4}{T(^\circ\mathrm{C})} = 11.2 - 1.96\ln\left(\frac{X_{EnFs}^{cpx}}{X_{EnFs}^{opx}}\right) - 3.3\left(X_{\mathrm{Ca}}^{cpx}\right) - 25.8\left(X_{\mathrm{CrCaTs}}^{cpx}\right) + 33.2\left(X_{\mathrm{Mn}}^{opx}\right) - 23.6\left(X_{\mathrm{Na}}^{opx}\right) - 2.08\left(X_{En}^{opx}\right) - 8.33\left(X_{Di}^{opx}\right) - 0.05P(\mathrm{kbar})$$

Equation 2- From Putirka, (2008).

$$P(\text{kbar}) = -94.25 + 0.045T(^{\circ}\text{C}) + 187.7\left(X^{opx}_{\text{Al(VI)}}\right) + 246.8\left(X^{opx}_{Fm_2Si_2O_6}\right)$$
$$-212.5\left(X^{opx}_{En}\right) + 127.5\left(a^{opx}_{En}\right) - \frac{1.66}{K_f} - 69.4\left(X^{cpx}_{EnFs}\right) - 133.9\left(a^{cpx}_{Di}\right)$$

Equation 3- From Putirka, (2008).

By solving equations 2 and 3 simultaneously, pressure and temperature estimations are possible. The results are displayed in table 6 below.

Sample Pair	**P (kbar)**	**T ºC**	**Depth (km)**	**Cpx/Opx K_d(Fe-Mg)**
OPX-CPX 1	7.1	1104	23.4	1.033
OPX-CPX 2	6.5	1097	21.5	1.081
OPX-CPX 3	5.6	1081	18.5	1.158
Average	6.4	1094	21.1	
Uncertainty	0.8	12	2.5	

Table 7- Pressure and Temperature estimates using orthopyroxene and clinopyroxene.

DISCUSSION

Sr Isotopes in Open System processes

The $^{87}Sr/^{86}Sr$ data from samples 513-4b and 513-7 show that the $^{87}Sr/^{86}Sr$ ratio of the plagioclase crystals (0.710361-0. 0.715863) are mostly higher compared to whole rock $^{87}Sr/^{86}Sr$ ratios (0.710096-0.710212). These data reveal several interesting pieces of information. The $^{87}Sr/^{86}Sr$ data show that the plagioclase crystals are a more sensitive analytical tool for detecting variations in $^{87}Sr/^{86}Sr$ as opposed to measuring whole-rock $^{87}Sr/^{86}Sr$ values. This method is thus a better source of data when considering open system processes that affect the Sr isotopic compositions of a system. No previous work has used the sensitive single-grain plagioclase Sr analysis on samples from the Ashi Volcano.

Wei et al. (2017) is the only other published work focusing on the Sr content of samples of the Ashi Volcano. The Sr isotope data collected was whole rock and yielded $^{87}Sr/^{86}Sr$ values (0.707490-0.710523) that were enriched compared to bulk silicate Earth (BSE), but did not show enrichment values that would be expected if the Ashi magma chamber experienced significant crustal assimilation. This is a surprising conclusion, since the crustal thickness of the NW Tibetan Plateau is up to 80 km thick. This extremely thick crust would provide ample opportunity for crustal assimilation. The work by Wei et al. (2017) used whole rock Sr analyses to draw these conclusions, which explains the discrepancies between their Sr isotope data and the Sr isotope data presented in this research. Note that our whole-rock Sr isotope data are consistent with the Sr isotope data of Wei et al. (2017) for the same type of rocks.

Drawing conclusions from the measured $^{87}Sr/^{86}Sr$ values of samples 513-4b and 513-7, crustal assimilation is clearly detected in some plagioclases because their $^{87}Sr/^{86}Sr$ values (up to 0.716) are significantly greater than the whole rock value (0.710). These high $^{87}Sr/^{86}Sr$ values can not be attributed to mantle-derived basaltic magma recharge because mantle-derived magmas have $^{87}Sr/^{86}Sr$ ratios (0.702 to 0.706, Zindler and Hart 1986; Zou et al., 2000), lower than the Ashi whole rocks (0.710). Our data show that the plagioclase minerals contained within the Ashi volcanic rocks are both phenocrysts crystallized from the host magmas and xenocrysts from crustal contaminations.

As mentioned previously, this crustal assimilation plays an important role in the evolution of the Ashi magmas. It is logical to consider the great distance that the magma of the Ashi Volcano travelled and surmise that it assimilated enough continental crust to significantly alter its $^{87}Sr/^{86}Sr$ content. Other optical evidence for crustal assimilation was observed and presented in Figure 23, which shows sillimanite in a potassium feldspar. This is likely a xenocryst from surrounding country rock. Sillimanite is not typically found as an igneous mineral phase. Instead, it is commonly produced by metamorphosing pelitic sediments through high temperatures (>800ºC) and over a wide pressure range. It is reasonable to conclude that the sillimanite xenocryst is possibly assimilated country rock that underwent pseudo-metamorphism during its time in the Ashi magma chamber.

Magma Chambers and Recharge Events

Drawing conclusions from the analyses on both plagioclase and pyroxenes, it is not possible to positively conclude that the magma chamber beneath the Ashi Volcano experienced recharge events from a mantle source, as was proposed by Wei et al., (2017). It is possible that the changing conditions of the magma (pressure, temperature, water content) caused the observed zonation in plagioclase. There was no observed evidence that the magma chambers received any new input of magma. Wei et al., (2017) concluded that new magma from the source was the likely cause of the 1951 eruption. The evidence in their research was the homogeneity in the $^{87}Sr/^{86}Sr$ signature of multiple Ashi volcanic rocks. Recharge by new basaltic magma (with low $^{87}Sr/^{86}Sr$) would produce crystals with $^{87}Sr/^{86}Sr$ ratios lower than the bulk rock values, but the opposite is observed. Reverse zoning in plagioclase can be caused by 4 factors: temperature, pressure, and water content, and assimilation. Our Sr isotope studies clearly detects crustal assimilation because Sr isotopes are not dependent on variations in temperature, pressure, and water content.

Temperature and Pressure

The temperature and pressure estimates from the data show that the magma chamber was under pressure between 7.1-5.6 kbars, yielding a depth estimate of 18.5-23.4 km. The corresponding temperature range is 1081ºC-1104ºC. The depth estimate is in good agreement with other reported estimates, but the temperature estimates are a bit lower than other reported values reported e.g., Yu et al., (2014). These pre-eruption pressure and temperature estimates show that the magma chamber is at a depth that agrees with other reported values.

CONCLUSIONS

Volcanism in the Ashikule basin has been an active process for Quaternary period, with the most recent eruption from the Ashi Volcano in 1951. With little work done on the Ashi Volcano, there are many unanswered questions on the evolution of its magma. Specifically, with crustal thickness at approximately 80 km, the role of crustal assimilation is a topic of interest. Previously, crustal assimilation had been evaluated by Sr isotopic work on the bulk rocks. This method, however, was not sensitive enough to detect the contaminated signature present in the samples of the Ashi Volcano. Sr isotopic compositions from individual plagioclase crystals are more sensitive indicators of magma contaminations. Our new data lends itself to the conclusion that the magma has in fact assimilated crustal material.

The Ashi plagioclase yield $^{87}Sr/^{86}Sr$ between 0.710361-0.715863. The $^{87}Sr/^{86}Sr$ of whole rock measurements range between 0.710096-0.710212. This lower Sr values for whole rock is due to issues with averaging of the Sr values from various mineral phases. The individual plagioclase crystals are a much more sensitive indicator of Sr isotopic signatures because of the lack of mixing compared to bulk rock. The $^{87}Sr/^{86}Sr$ ratio from the plagioclase is much closer to a ratio that would be characteristic of crustal material. Therefore, it is apparent that some of the plagioclase crystals are xenocrystic and are the product of assimilation of country rock.

The possibility of magma recharge events causing reverse compositional zonation reported in other previous works is an area recommended for further research. While reverse compositional zonation is observed, it is not uniformly observed and could be caused by

variables other than inputs of new magma. Changing temperatures, pressures, and water content all may cause zonation and are not directly indicative of new magma inputs. It is also likely that the assimilation has altered the composition of the magma, which may also produce zonation.

The Ashi magma chamber today is located 18.5-23.4 km beneath the surface. The corresponding temperature range is 1081ºC-1104ºC. These values are in agreement with the reported literature values.

REFERENCES

Chatterjee, S., Goswami, A., Scotese, C., 2013. The longest voyage: Tectonic, magmatic, and paleoclimate evolution of the Indian plate during its northward flight from Gondwana to Asia. Gondwana Research 23.1, 238-267.

Cooper, K.M., Reid, M.R., Dunbar, N.W., Mcintosh, W.C., 2002. Origin of mafic magmas beneath northwestern Tibet: constraints from 230Th–238U disequilibria. Geochemistry, Geophysics, Geosystems 3 (11), 1–23.

Dewey, J., Shackleton, R., Chengfa, C., Yiyin, S.,1988. The tectonic evolution of the Tibetan plateau. The Royal Society. http://dx.doi.org/10.1098/rsta.1988.0135

Faure, G. and Mensing, T.M., 2005. Isotopes: Principles and Applications. Third Edition. 897pp.

Liu Jiaqi. Volcano in China. Beijing, 1993: Science Press, 44-46.

Marshall, Daniel (1996), Ternplot: An Excel spreadsheet for Ternary diagrams, Computers and Geosciences, vol. 22 #6, p. 697-699.

Mikova, J. and Denkova, P., 2007. Modified chromatographic separation scheme for Sr and Nd isotope analysis in geological silicate samples. Journal of Geosciences 52, 221-226.

Putrika, K., 2008. Thermometers and barometers for volcanic systems. Reviews in Mineralogy and Geochemistry, 69: 61-120.

Tapponnier, P., Zhigin, X., Roger, F., Meyer, B., Arnaud, N., Wittlinger, G., Jinqsui, Y., 2001. Oblique stepwise rise and growth of the Tibet plateau. Science 294(5547), 1671-1677.

Turner, S., Hawkesworth, C., Liu, J., Rogers, N., Kelley, S., van Clasteren, P., 1993. Timing of Tibetan uplift constrained by analysis of volcanic rocks. Nature 364, 50–54.

Turner, S., Arnaud, N., Liu, J., Rogers, N., Hawkesworth, C., Harris, N., Kelley, S., van Calsteren, P., Deng, W., 1996. Post-collision, shoshonitic volcanism on the Tibetan plateau: implications for convective thinning of the lithosphere and the source of ocean island basalts. Journal of Petrology 37, 45–71.

Wei, F., Prytulak, J., Xu, J., Wei, W., Hammond, J., Zhao, B., 2017. The cause and source of melting for the most recent volcanism in Tibet: A combined geochemical and geophysical perspective. Lithos 288-289.

Williams, H.M., Turner, S.P., Pearce, J.A., Kelley, S.P., Harris, N.B.W., 2004. Nature of the source regions for post-collisional, potassic magmatism in southern and northern Tibet from geochemical variations and inverse trace element modelling. Journal of Petrology 45 (3), 555–607.

Xia, L.Q., Li, X.M., Ma, Z.P., Zu, X.Y., Zia, Z.C., 2010. Cenozoic volcanism and tectonic evolution of the Tibetan plateau. Gondwana Research, 19, 850–866.

Xu, J., Zhao, B., Zhang, L., Chen, Z., 2012. Field geological exploration of the Ashikule Volcano group in western Kunlun Mountains. Earthquake Research in China 26, 152-159.

Yu, H., Xu, J., Zhao, B., Shen, H., Lin, C., 2014. Magmatic processes of Ashi Volcano, western Kunlun Mountains, China. Acta Geologica Sinica, English Edition 88.2, 530-43.

Zhang, C. L., Zou, H. B., Li, H. K., Wang, H. Y. (2013) Tectonic framework and evolution of the Tarim Block in NW China. Gondwana Research 23, 1306-1315.

Zhao, M., 1976. Introduction on Ashikule active volcanoes and the Quaternary volcano groups in Kunlun Mountains of Xinjang. Xinjang Geology 1-2, 27-36.

Zou, H.B., 1999. Studies of mantle melting process and compositions using major and trace elements, Nd-Sr-Pb isotopic systematics and U-series disequilibria: Mathematical modeling and experimental analyses. Ph.D. Thesis, Florida State University, 185pp.

Zou, H.B., Zindler, A., Xu, X.S., Qi, Q., 2000. Major and trace element, and Nd-Sr-Pb isotope studies of Cenozoic basalts in SE China: mantle sources, regional variations, and tectonic significance. Chemical Geology 171, 33-47.

Appendix 1

Spectral signatures generated from the EDS spectrometer on the Auburn University Electron Microprobe Analyzer (AU-EMPA). This data was generated to assure analyses were completed on the appropriate mineral phases and to discern mineral phases that were enigmatic when identifying composition.

Princeton Gamma Tech

PGT eXcalibur Report

Thursday, March 29, 2018

ID(1):

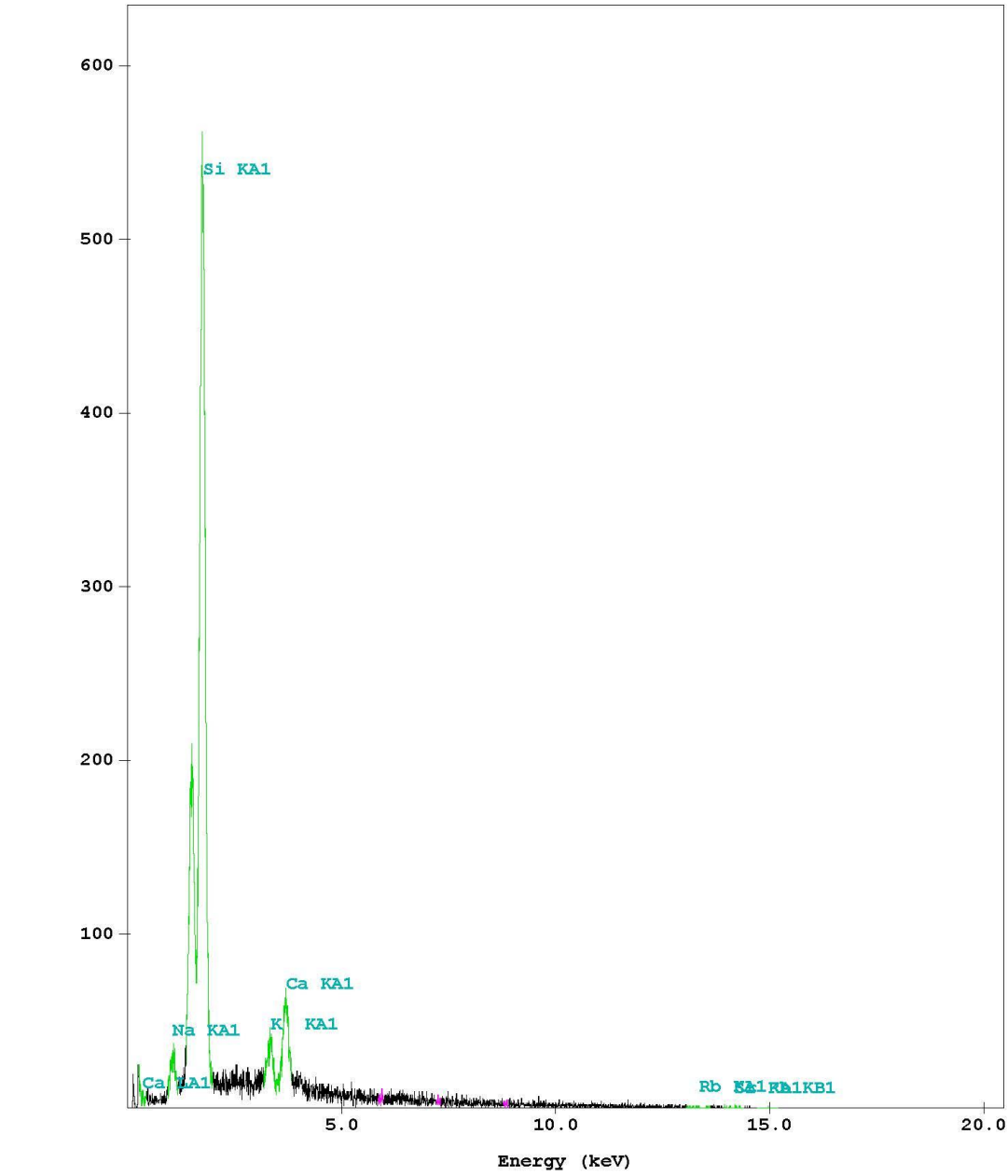

Princeton Gamma Tech
PGT eXcalibur Report
Thursday, March 29, 2018

ID(1):

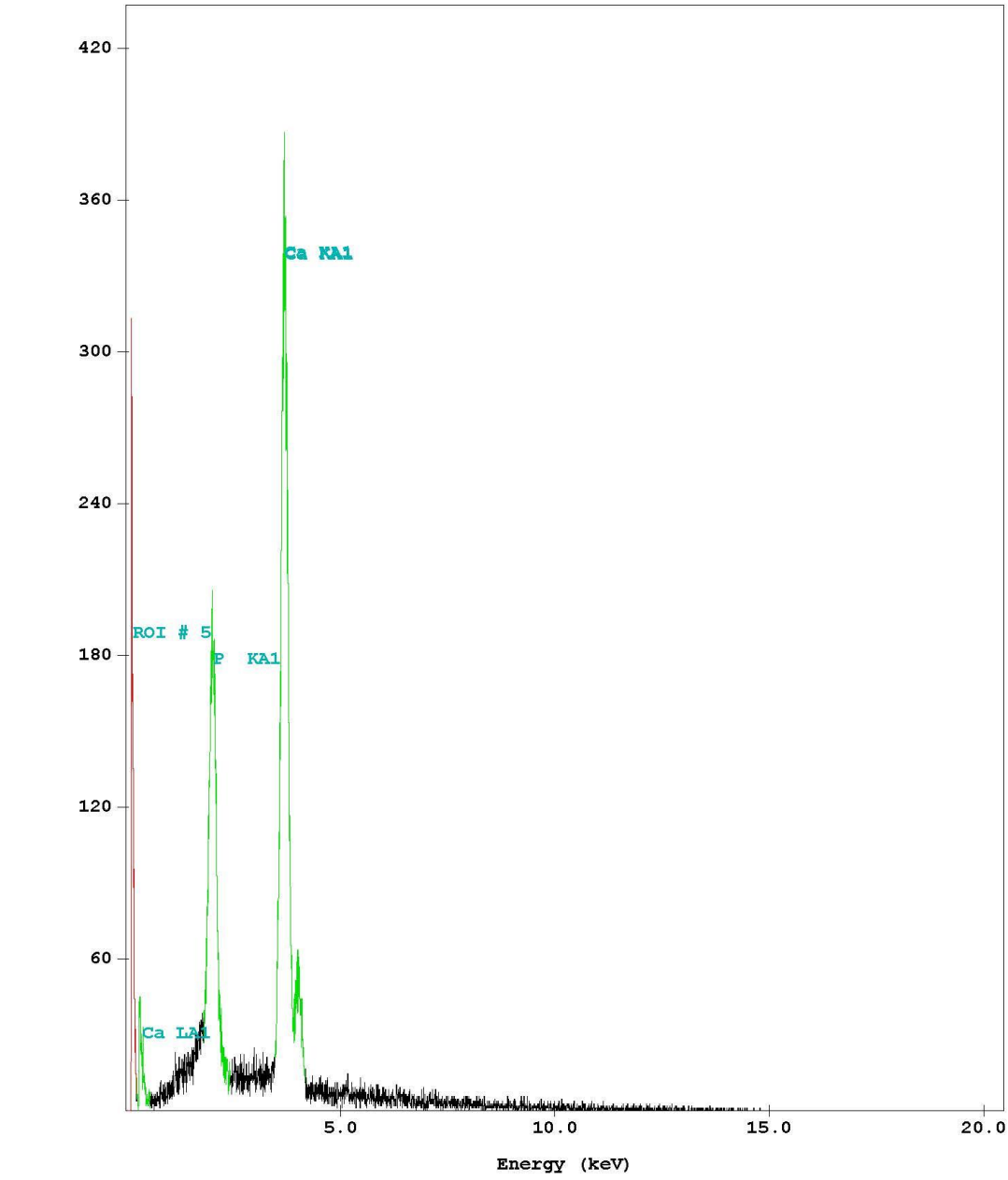

Princeton Gamma Tech

PGT eXcalibur Report

Thursday, March 29, 2018

ID(1):

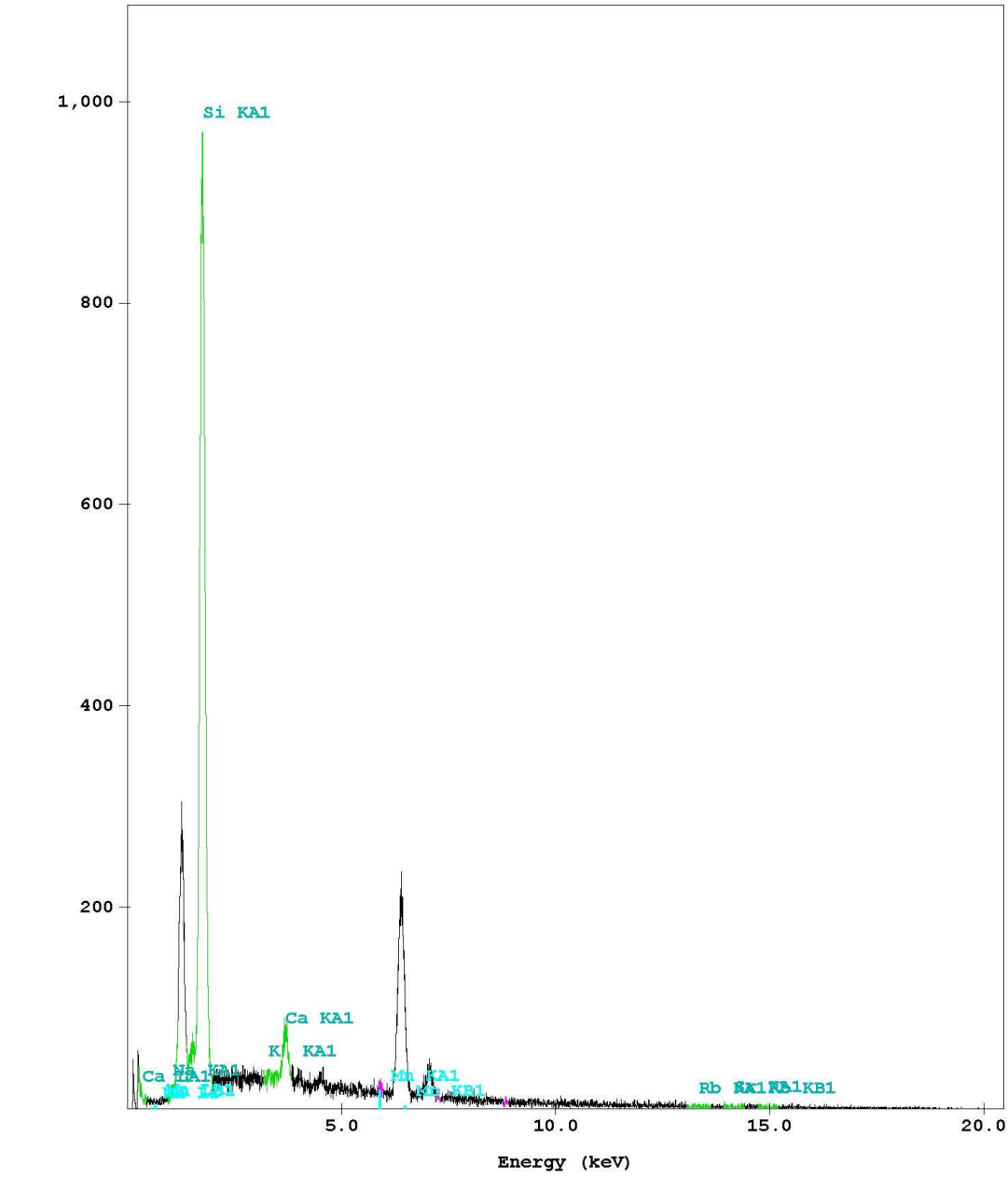

Appendix 2

Oxide weight percent values for Amelia albite, anorthite, and wolastonite standards used for the preceding analyses.

Pt#	SiO_2	Al_2O_3	FeO	MnO	MgO	CaO	Na_2O	K_2O	Total
Amelia 1	45.26	36.06	0.0021	0.0023	0.0523	19.31	0.5823	0.0005	**101.27**
Amelia 2	45.03	36.52	0.0021	0.0023	0.0536	19.26	0.54	0.0123	**101.42**
Amelia 3	45.29	36.24	0.0021	0.0023	0.0057	19.52	0.4994	0.0199	**101.58**

Pt#	SiO2	Al_2O_3	FeO	MnO	MgO	CaO	Na_2O	K_2O	Total
Anorthite 1	44.45	35.98	0.46	0.000	0.064	19.28	0.59	0.017	**100.83**
Anorthite 2	44.54	36	0.52	0.014	0.025	19.07	0.51	0.009	**100.69**
Anorthite 3	44.87	36.53	0.44	0.000	0.045	19.13	0.58	0.016	**101.61**
Anorthite 4	44.51	35.85	0.43	0.009	0.054	19.50	0.45	0.017	**100.82**

Pt#	SiO_2	TiO2	Al_2O_3	FeO	MnO	MgO	CaO	Na_2O	K2O	Cr_2O_3	Total
Wol 1	51.98	0	0.02	0.00	0.00	0.0525	47.83	0.00	0	0	**99.89**
Wol 2	52.46	0	0.00	0.00	0.01	0.1434	47.36	0.00	0	0	**99.97**
Wol 3	55.13	0	0.61	0.78	0.05	18.81	24.23	0.42	0	0	**100.03**